

Electronic and Transport Properties of Graphene Nanostructures

CHRISTOPHER J. POOLE

Submitted for the degree of Doctor of Philosophy

under the supervision of

Prof. Vladimir I. Fal'ko

Dr. Vadim V. Cheianov

February 2012

ProQuest Number: 11003696

All rights reserved

INFORMATION TO ALL USERS

The quality of this reproduction is dependent upon the quality of the copy submitted.

In the unlikely event that the author did not send a complete manuscript and there are missing pages, these will be noted. Also, if material had to be removed, a note will indicate the deletion.



ProQuest 11003696

Published by ProQuest LLC (2018). Copyright of the Dissertation is held by the Author.

All rights reserved.

This work is protected against unauthorized copying under Title 17, United States Code
Microform Edition © ProQuest LLC.

ProQuest LLC.
789 East Eisenhower Parkway
P.O. Box 1346
Ann Arbor, MI 48106 – 1346

The research presented in this thesis is my own work (except where explicitly stated), and has not been submitted towards the award of a higher degree elsewhere.

Chapter 2 published as C. J. Poole. On the applicability of the two-band model to describe transport across n-p junctions in bilayer graphene. *Solid State Communications*, **150**(13–14):632–635, 2010.

“Research is what I’m doing when I don’t know what I’m doing.”

— Wernher von Braun

Acknowledgements

I would like to thank my supervisors Prof. Vladimir Fal'ko and Dr. Vadim Cheianov for their help and guidance throughout, as well as answering my many questions. I would also like to thank Prof. Henning Schomerus and Dr. Ed McCann for invaluable discussions and excellent explanations.

Thanks to everyone in A13 for making the environment a pleasure to conduct research in, including Chris Birchall, Nathan Davies, Oleksiy Kashuba, Kostya Kechedzhi, Marcin Mucha-Kruczyński, Zhenia Suprunenko, and John Wallbank. I thank Diana Gradinar and Stephanie Huntington for their help with proofreading this thesis. I also thank Diana for her thoughts and comments on the calculations in Chapter 3.

Finally, I am indebted to friends, family, and Katie, who have helped enormously during the course of this degree. Thank you.

Overview

Graphene — a crystal of carbon atoms in a two-dimensional (2D) honeycomb lattice — is a gapless semiconductor, and has attracted great interest since it was fabricated in 2004 [1–3]. This monolayer of graphite has been shown to have remarkable properties, such as a linear energy dispersion relation [4] and massless, chiral fermions [5]. This thesis discusses some of these properties, as well as those found in bilayer graphene [6–8]. Bilayer graphene is the formation of two coupled layers of graphene, exhibiting Bernal stacking (to be discussed later), and features massive chiral fermions [9].

Chapter 1 discusses the tight binding model, and derives the Hamiltonians for monolayer and bilayer graphene, used in subsequent Chapters. We also review important phenomena that account for the results seen in later Chapters. In addition to the material discussed in this Chapter, several excellent review articles have been written that cover other features and phenomena in few-layer graphene systems [10–17].

Chapter 2 is original published work. We extend the low energy effective two-band Hamiltonian for electrons in bilayer graphene (McCann and Fal’ko [7]) to include a spatially dependent electrostatic potential. We find that this Hamiltonian contains additional terms, as compared to the one used earlier in the analysis of electronic transport in n-p junctions in bilayers (Katsnelson et al. [9]). However, for potential steps $|u| < \gamma_1$ (where γ_1 is the interlayer coupling), corrections to the transmission probability due to such terms are small. For the angle-dependent transmission $T(\theta)$

we find $T(\theta) \cong \sin^2(2\theta) - (2u/3\gamma_1) \sin(4\theta) \sin(\theta)$ which slightly increases the Fano factor: $F \cong 0.241$ for $u = 40\text{meV}$.

Chapter 3 is original work which was carried out simultaneously with Barbier et al. [18]. Nevertheless, the method of analysis and parameters considered are different, and the results are reached independently. Agreement is found with [19–21]. The work focuses on the introduction of a periodic potential profile in monolayer and bilayer graphene systems, creating extra Dirac points in the energy dispersion for monolayer graphene. Classical catastrophe theory is then employed to describe caustics and cusps in a system with a periodic potential profile, for cusps forming at regular interfaces. The periodicity of the formation of cusps is matched with the periodicity of the superlattice. The energy at which this occurs is then mapped to the energy spectrum found when analysing monolayer graphene with a periodic potential profile.

In Chapter 4 we create a model to characterise the angles and commensurability of a few layers of hexagonal lattice materials, seen in STM images in experiments. The model allows for different lattice constants and rotations for each layer, as well as selectively showing lattice sites that are nearly commensurate with sites in other layers. Two popular cases are turbostratic graphene (bilayer graphene where one layer is rotated relative to the other) and graphene on hBN (hexagonal boron nitride).

Finally, appendices with complete source code to reproduce these results are given, with examples of their usage.

Contents

Acknowledgements	iv
Overview	v
Contents	vii
List of Figures	x
List of Tables	xix
1 Introduction	1
1.1 Tight Binding Method	2
1.2 Nearest-Neighbour Monolayer Hamiltonian Near \mathbf{K} Points	5
1.2.1 Band Structure	8
1.3 Nearest-Neighbour Bilayer Hamiltonian Near \mathbf{K} Points	11
1.3.1 Band Structure	15
1.4 Underlying Phenomena	16
1.4.1 Pseudospin and Chirality	16
1.4.2 Berry Phase	19
1.4.3 Klein Tunnelling	19

2	Analysis of the Applicability of the Two-Band Model to Describe Transport Across n-p Junctions in Bilayer Graphene	21
2.1	Introduction	21
2.2	Derivation of the Effective Hamiltonian	23
2.2.1	Schrieffer-Wolff Transformation	24
2.2.2	Renormalising the Wavefunctions	27
2.2.3	Form of the Effective Hamiltonian	28
2.2.4	Spatially-Dependent Gap in the Energy Spectrum	30
2.2.5	Combined Effective Hamiltonian	32
2.3	Approximation of the Hamiltonian	32
2.4	Analysis of the n-p Junction	33
2.5	Conductance and Fano Factor	36
2.6	Conclusion	37
3	Analysis of a Periodic Modulation of the Potential Profile in Monolayer and Bilayer Graphene	39
3.1	Transfer Matrix Formalism	40
3.1.1	Monolayer Graphene	40
3.1.2	Bilayer Graphene	43
3.2	Periodic Modulation of the Potential Profile in Monolayer Graphene	48
3.2.1	Analysis of the Long Wavelength Approximation	51
3.3	Periodic Modulation of the Potential Profile in Bilayer Graphene	53
3.4	The Formation of Cusps at n-p Junction Interfaces	55

3.4.1	Matching the Periodicity of the Formation of Cusps to the Period of the Superlattice	59
3.5	Conclusion	63
4	Characterisation of Moiré Patterns Formed by Incommensurate Hexagonal Lattices	65
4.1	Theory of Moiré Patterns	66
4.1.1	Analysis Without Rotation	67
4.1.2	Fourier Analysis Method for Rotated Layers	70
4.2	Modelling Moiré Images	75
4.2.1	Commensurate Lattice Sites	76
4.3	A Systematic Study and Comparison of Moiré Model Images to Experimental Images	78
4.3.1	Scanning Tunneling Microscope Images of Graphitic Layers .	79
4.3.2	Monolayer and Bilayer Graphene on hBN	80
4.4	Conclusion	82
5	Summary and Conclusions	83
A	Source Code for Drawing Energy Surfaces Due to a Periodic Mod- ulation of Potential	86
B	Source Code for Rendering Moiré Images	95
C	Full Derivation of Pseudospin in Bilayer Graphene	104
	Bibliography	107

List of Figures

1.1	Geometry of a hexagonal lattice. Red atoms on sublattice A, blue atoms on sublattice B. $a = 2c = \sqrt{3}l$, $b = l \cos 60^\circ = l/2$, $c = l \sin 60^\circ = \sqrt{3}l/2$, $d = l + 2b = 2l$	2
1.2	Geometry of a hexagonal lattice in \mathbf{k} space, with sublattice A (B) sites shown in red (blue). $b_l = b/\sqrt{3}$, $\mathbf{K} = (-4\pi/3a, 0)$ and $\mathbf{K}' = (4\pi/3a, 0)$ relative to zero at the Γ point.	4
1.3	Nearest-neighbour vectors. $\mathbf{R}_1 = (0, a/\sqrt{3})$, $\mathbf{R}_2 = (a/2, -a/2\sqrt{3})$, $\mathbf{R}_3 = (-a/2, -a/2\sqrt{3})$	6
1.4	Monolayer graphene band diagram in \mathbf{k} space, showing energy versus in-plane momentum. The hexagonal Brillouin zone and Dirac cones at each \mathbf{K} point are displayed. Eqn. 1.24 was plotted using values of $a = 0.142$ nm, $\gamma_0 = -3.033$ eV, $s = 0.129$ eV, and momentum range $\pm 2\pi/a$ [13, 27].	9
1.5	Density plot of monolayer graphene band structure in \mathbf{k} space, where the hexagonal lattice is clearly defined. Eqn. 1.24 plotted using the same values as in Fig. 1.4.	10
1.6	Energy dispersion of monolayer graphene showing the linear bands at low energies around the \mathbf{K} points. Eqn. 1.24 plotted using the same values as Fig. 1.4, with $k_y = 0$ and $k_x = \pm 2\pi/a$	11

- 1.7 Schematic of the bilayer graphene lattice with Bernal stacking. The bonds in the top (bottom) layer are indicated by dashed (solid) lines. Sublattice A (B) sites in the bottom layer are coloured red (green). The top layer sublattice A (B) sites are black (blue). 12
- 1.8 Schematic of AB (Bernal) stacked bilayer graphene showing intralayer and interlayer couplings, as well as a unit cell comprising of four carbon atoms: A1, B1, A2, and B2. 13
- 1.9 Band structure of bilayer graphene, showing low (high) energy bands in red (blue). The high energy conduction band has a minimum at $\epsilon = \gamma_1$. Plotted using $\Delta = 0$, $\phi = 90^\circ$ 17
- 2.1 Schematic of AB (Bernal) stacked bilayer graphene showing intra- and inter-layer couplings, as well as a unit cell comprising of four carbon atoms: A1, B1, A2, B2. Inset: energy bands in bilayer graphene near a \mathbf{K} point. The energy of the quasiparticles is near $\epsilon = 0$, qualifying the assumption that γ_1 is large compared to other energies in the system. The transformation reduces the band structure to blue (solid) bands only. 22
- 2.2 Low-energy band structure of a single valley on either side of the potential step. The Fermi energy is the same on both sides, causing an electron from the left side to tunnel through the barrier from the conduction band to the valence band on the right side. 24
- 2.3 Angular dependence of quasiparticle transmission through an n-p junction. 34

- 2.4 Transmission probability through an n-p junction. The solid (dashed) line is with (without) correctional terms. Without correctional terms there is perfect transmission at an angle of 45° to the interface. (a) Transmission at $u = 40$ meV. (b) Transmission at $u = 80$ meV. Plotted with $\epsilon = 0$, $v \approx c/300$, $\gamma_1 = 0.4$ eV, $m = 0.035 m_e$, and $\Delta = 0$. 36
- 2.5 Fano factor as a function of u , from a numerical calculation of the transmission probability for the same parameters as given in Fig. 2.4. 38
- 3.1 Schematic showing a periodic profile of height u , separated by wells of width $(1 - \alpha)l$ (where $\alpha \in (0, 1)$). The Fermi energy ϵ_F is defined to be in the centre of the barrier. Regions one to five are indicated. 40
- 3.2 Schematic of an n-p-n junction in monolayer graphene in one dimension, with interfaces at $x = 0$ and $x = l$ 41
- 3.3 Schematic of an n-p-n junction in bilayer graphene in one dimension, with interfaces at $x = 0$ and $x = l$. In addition to the plane waves as in Fig. 3.2, evanescent waves are also allowed. Regions 1–4 are also shown. 44
- 3.4 Angular dependence of transmission through an n-p-n junction in (a) monolayer and (b) bilayer graphene. (a) Transmission plotted with $\epsilon = 83$ meV, $l = 100$ nm, and $u = 200$ meV (285 meV) for the red (blue) curves. (b) Transmission plotted with $\epsilon = 17$ meV, $l = 100$ nm, and $u = 50$ meV (100 meV) for the red (blue) curves. The values chosen are used to match Katsnelson et al. [9, Fig. 2]. . 49
- 3.5 First conduction and valence energy surfaces for periodically-modulated monolayer graphene. Plotted using the parameters $\alpha = 1/2$ and $u = 10\pi$ 50

- 3.6 First conduction and valence energy surfaces for periodically-modulated monolayer graphene. Plotted using the parameters $\alpha = 6/10$ and $u = 6\pi$ 51
- 3.7 (a)–(c) Energy dispersion surfaces with energy ϵ plotted against the phase ϕ and perpendicular direction of momentum k_y for a Kronig-Penney system in monolayer graphene. (d)–(f) show the corresponding energy cuts through these surfaces (that is, (d) corresponds to (a), etc.). The energy that the cut is made at is determined by the energy of the caustics formed in the system; see Section 3.4. Parameters used to plot Eqn. 3.29 are (a) $\alpha = 1/2$, $u = 10\pi$, (b) $\alpha = 4/10$, $u = 6\pi$, (c) $\alpha = 8/10$, $u = 5\pi$. The values of δ used to produce (d)–(f) are 0.1, 0.7, and 0.2, respectively. The values of ϵ_{cut} used to produce (d)–(f) are 0, 3.7, and -9.4, respectively. 52
- 3.8 Energy dispersion of the long wavelength approximation for a monolayer graphene system with a periodic potential profile (when $1 \gg \tilde{u}$). 53
- 3.9 (a) First two conduction bands of the spectrum of a superlattice with square barriers in bilayer graphene; $\tilde{u} = 37.02$ (corresponding to $u = 100$ meV and $l = 20$ nm), $\alpha = 1/2$. (b) Contour plot of the first conduction band of the spectrum in (a). 55
- 3.10 First two conduction and valence bands for an even periodic potential profile in bilayer graphene (that is, $\alpha = 1/2$). The height of the barrier is $u = 100$ meV. 55
- 3.11 Caustics in an n-p junction (where the p region is coloured gray). Incident waves approach the junction at an angle θ_c (in the conduction band), and refract at an angle θ_v (in the valence band). The envelope of caustics is highlighted in red, showing their meeting as a cusp. Plotted using refractive index $n = -0.82$ 57

- 3.12 The path of one ray to form caustics in an n-p-n junction (where the p region is coloured gray). Incident waves approach the junction (with the first interface at $x = 0$) at an angle θ_c (in the conduction band), and refract at an angle θ_v (in the valence band). Outgoing rays form at an angle θ_c (since we assume a symmetric junction). The caustics overlaid are formed when Eqn. 3.42 matches the position of the second interface. 61
- 3.13 Plots of Eqn. 3.29 for fixed Bloch phase, using parameters $\alpha = 0.4$, $u = 6\pi$, and (a) $\phi = \pi$ (b) $\phi = 0$. Dashed isoenergetic lines are shown to define the energy at which caustics (from rays traversing a length l equal to the period of the potential system), occur with $\delta = 0.7$ and $\epsilon_{\text{cut}} = 3.77$, as defined in Eqn. 3.48. 63
- 4.1 Generated Moiré pattern showing the formation of a superlattice, formed by two hexagonal lattices, with lattice constants a and $a(1 - \sqrt{2}/25)$. (The latter value is chosen to force the model to use an irrational number for the lattice constant.) AA and AB stacking alignments are highlighted. 66
- 4.2 Schematic showing the geometry of a hexagonal lattice. Sites in sublattice A (B) are coloured red (blue). $a = 2c = \sqrt{3}l$, $b = l \cos 60^\circ = \frac{l}{2}$, $c = l \sin 60^\circ = \frac{\sqrt{3}l}{2}$, $d = l + 2b = 2l$ 67
- 4.3 Comb image, representing parallel sides of the lattice hexagons as parallel lines. When overlapped and seen from a distance, they produce a periodic Moiré pattern. 68
- 4.4 (u, v) frequency plane showing two impulses at \mathbf{f} and $-\mathbf{f}$. Inset shows that frequency vector \mathbf{f} is perpendicular to the gratings. . . . 71

- 4.5 The top row shows real images of parallel grids, superimposed in the third image to show the formation of Moiré patterns. The bottom row shows the corresponding frequency vectors for each pattern and the superimposed image, including the effective Moiré frequency vector \mathbf{f}_m 72
- 4.6 Lattice geometry showing \mathbf{c}_i and \mathbf{r}_B vectors used in the calculation of commensurate sites. 75
- 4.7 (a) Atomic model of a 12 nm^2 graphene layer with hBN below, rotated at an angle of 10° . Only graphene sites that are almost directly above boron or nitrogen sites are shown, coloured red (blue) for graphene sublattice A (B). (b) Atomic model of a 12 nm^2 monolayer graphene layer below two layers of hBN, the first rotated by 5° relative to graphene, the second by 10° . Only those sites in the hBN layer that are nearly commensurate with sites from sublattice A (B) in the graphene layer are rendered, coloured red (blue). . . . 77
- 4.8 (a) Commensurability angle formed by turbostratic graphene with a relative angle of -32.2° . (b) Three layer unit supercell; the two lower layers present the usual AB stacking sequence of the bulk hexagonal graphite crystal. The top layer presents a clockwise rotation angle of 21.8° . (b) is analogous to Cisternas et al. [106, Fig. 1]. 78
- 4.9 (a) Moiré image formed by two layers of graphene with a relative angle of 1.8° . An effective area of 22.5 nm^2 is shown. (b) The same image showing commensurate sites causing a periodic modulation of the density of states. 79

- 4.10 (a) Moiré image formed by two Bernal-stacked layers of graphene with a rotated monolayer on top (with a relative angle of 1.8°). (b) The same image showing nearly commensurate sites causing a periodic modulation of the density of states. Sites in the Bernal-stacked layers that are nearly commensurate with sites in the A (B) sublattice of the rotated layer are coloured red (blue). 80
- 4.11 (a) Moiré image produced by overlapping two graphitic monolayers with a relative rotation of 3.5° . Lattice sites from sublattice A (B) are coloured red (blue) (for both layers). (b) The same layer configuration as in (a) but only showing the lattice of the non-rotated layer (no sites); only nearly-commensurate sites are rendered. Sites in the rotated layer that are nearly commensurate with those from sublattice A (B) in the other layer are coloured red (blue). 81
- 4.12 (a) 20 nm^2 STM image of graphene-hBN surface topology with a relative angle of 4° , adapted from Decker et al. [114, Fig. 2(c)]. (b) Atomic model image using equivalent parameters for surface area and relative rotation. (c) Atomic model image showing nearly-commensurate sites. Lattice sites in the hBN layer that are almost commensurate with graphene sublattice A (B) sites are coloured red (blue). 81
- 4.13 Graphene monolayer above hBN with a relative angle of -10.9° . (a) 16 nm^2 STM image of graphene-hBN surface topology, adapted from Xue et al. [115, Fig. 2(c)]. (b) Atomic model image using equivalent parameters for surface area and relative rotation. (c) Atomic model image showing nearly-commensurate sites. Lattice sites in the hBN layer that are almost commensurate with graphene sublattice A (B) sites are coloured red (blue). 81

A.1	Central equation sans plotted with values $u = 10\pi$, $k_y = 16$, $\phi = 1$, and $\alpha = 1/2$ to determine the first root, approximately $\epsilon = \pi/2$	88
A.2	Valence and conduction bands of the spectrum of a superlattice with square barriers in monolayer graphene; $u = 10\pi$, $\alpha = 1/2$. Values used to match Barbier et al. [19, Fig. 2].	90
A.3	Valence and conduction bands of the spectrum of a superlattice with square barriers in monolayer graphene; $u = 6\pi$, $\alpha = 4/10$. Values used to match Barbier et al. [19, Fig. 3].	90
A.4	The first two conduction bands of the spectrum of a superlattice with square barriers in bilayer graphene; $\tilde{u} = 37.02$ (corresponding to 100 meV, $l = 20$ nm), and $\alpha = 1/2$. Values used to match Barbier et al. [20, Fig. 6(1)].	94
B.1	Schematic of the bilayer graphene lattice with Bernal stacking. The bonds in the top (bottom) layer are indicated by dashed (solid) lines. Sublattice A (B) sites in the bottom layer are coloured red (green). The top layer sublattice A (B) sites are black (blue).	100
B.2	Model of a 50x50 graphene layer with hBN below, rotated at an angle of 10° . Only graphene sites that are almost directly above boron or nitrogen sites are shown, coloured red (blue) for graphene sublattice A (B).	101
B.3	Model of monolayer graphene below two layers of hBN, the first rotated by 5° relative to graphene, the second by 10° . Only graphene sites almost directly below a nitrogen site are drawn: sublattice A (B) in red (blue).	102

C.1 Schematics showing graphene bilayer in plane on a substrate (e.g., SiO₂). Top and bottom gates are configured to independently vary the Fermi energy and the size of Δ . The gates can be separated by an in-plane distance of 10–100 nm. 106

List of Tables

2.1	Pseudospin elements and their corresponding momenta values. . . .	35
3.1	Pseudospin elements and momenta for the analysis of transmission through an n-p-n junction in monolayer graphene.	43
3.2	Unitless parameters in bilayer graphene.	48
3.3	Pseudospin elements and momenta for the analysis of transmission through an n-p-n junction in bilayer graphene.	48
3.4	Pseudospin elements and their corresponding momenta values for monolayer graphene with a periodic potential profile.	50
3.5	Pseudospin elements and momenta for the analysis of a periodic po- tential profile in bilayer graphene. Parameters with tildes are unit- less, given in Table 3.2.	54
B.1	Formal parameters (with example values) of <code>graphLayer</code>	103

Chapter 1

Introduction

Carbon has six electrons in the following configuration: $1s^2 2s^2 2p^2$. The electrons in the $1s^2$ orbitals are strongly bound to the core, so do not contribute to the solid state properties of the element, as their energy is far from the Fermi energy compared with the valence electrons. $2s^2 2p^2$ electrons are the valence electrons, which are more weakly bound.

In the crystalline phase the four valence electrons form $2s$, $2p_x$, $2p_y$, and $2p_z$ orbitals. The energy difference between the $2p$ and $2s$ electrons is much less than the binding energy of the chemical bonds, so the electron wavefunctions mix. This mixing enhances the binding energy of the carbon atom with its neighbours, and is known as hybridisation. The mixing of a single $2s$ electron with $n = 1, 2, 3$ electrons in the $2p$ shell is known as sp^n hybridisation. Graphene is an isomer of carbon, and has sp^2 hybridisation. There are three σ bonds per carbon atom in-plane; the other electron is in the π orbital bond, perpendicular to the plane.

The graphene lattice is comprised of two inequivalent triangular sublattices (A and B; the direction of their bonds to nearest neighbours are different), with two inequivalent valleys (\mathbf{K} and \mathbf{K}') sitting at the Dirac points of the hexagonal Brillouin zone. The in-plane nearest-neighbour distance, l in Fig. 1.1, is approximately 1.42 \AA [4, 22, 23], while the interlayer separation is approximately 3.35 \AA [22, 24]

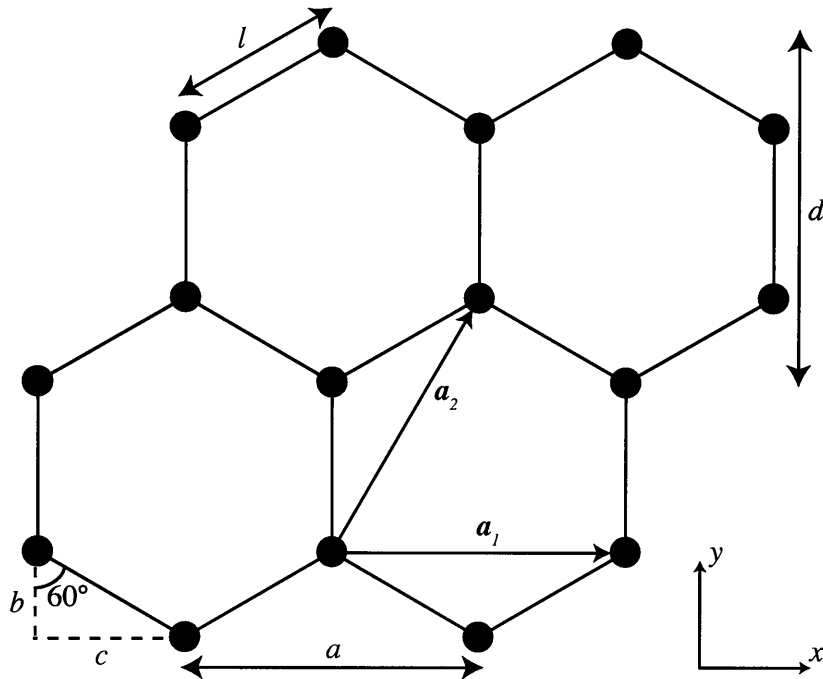


Fig. 1.1: Geometry of a hexagonal lattice. Red atoms on sublattice A, blue atoms on sublattice B. $a = 2c = \sqrt{3}l$, $b = l \cos 60^\circ = l/2$, $c = l \sin 60^\circ = \sqrt{3}l/2$, $d = l + 2b = 2l$.

(this value is taken from bulk graphite measurements, although we use this for bilayer graphene too). Since the intralayer bonds are covalent and interlayer bonds are due to the Van der Waals interaction, intralayer interactions are dominant. The electronic properties of monolayer and bilayer graphene discussed in this thesis are calculated from Hamiltonians derived using a tight binding approach [4, 13, 25], so this derivation is the first item in this thesis. Throughout, we set $\hbar = 1$.

1.1 Tight Binding Method

The general principle behind the tight binding method is that two non-interacting atoms have their own individual wavefunctions, and when brought together, the separated energy levels of the atoms overlap (due to the Coulomb interaction), splitting into bands. We wish to satisfy Bloch conditions, given periodic potential solutions of the Schrödinger equation. The wavefunction of the lattice must

satisfy the translation condition $T_{a_m}\Phi = e^{ik a_m}\Phi$ (with $m = 1, 2, 3$ for each independent spatial direction). To do this, we can construct the wavefunction $\Phi = (1/\sqrt{N})e^{ik\mathbf{R}}\phi(\mathbf{r} - \mathbf{R})$ (where the reference atom is at position \mathbf{R} , with a vector \mathbf{r} to a nearest neighbour), giving

$$\Phi_j(\mathbf{k}, \mathbf{r}) = \frac{1}{\sqrt{N}} \sum_{\mathbf{R}}^N e^{ik\mathbf{R}} \phi_j(\mathbf{r} - \mathbf{R}), \quad (1.1)$$

where N is the number of unit cells in the crystal ($\approx 10^{24}$) and $j = 1, \dots, n$ where n is the number of wavefunctions in each unit cell; thus there are n Bloch functions for a given wavevector \mathbf{k} . This is based on the j th atomic orbital in the unit cell. In Eqn. 1.1 we sum over all unit cells in the crystal, for each orbital j . We can approximate the wavefunction of the crystal itself by assuming that it is a linear combination of the unit cell Bloch functions*:

$$\Psi_j(\mathbf{k}, \mathbf{r}) = \sum_{j'=1}^n C_{jj'}(\mathbf{k}) \Phi_{j'}(\mathbf{k}, \mathbf{r}), \quad (1.2)$$

where $C_{jj'}(\mathbf{k})$ are coefficients. Now we have summed over all the unit cells, and over all orbitals in the crystal. The expectation value of energy is the average value taken in an experiment, which for the j^{th} orbital (thus, j^{th} eigenvalue), is

$$E_j(\mathbf{k}) = \frac{\langle \Psi_j | H | \Psi_j \rangle}{\langle \Psi_j | \Psi_j \rangle} \equiv \frac{\int \Psi_j^* H \Psi_j d\mathbf{r}}{\int \Psi_j^* \Psi_j d\mathbf{r}}, \quad (1.3)$$

where H is the Hamiltonian of the solid. If we insert Eqn. 1.2 into this then

$$E_i(\mathbf{k}) = \frac{\sum_{j,j'=1}^n C_{ij}^*(\mathbf{k}) C_{ij'}(\mathbf{k}) \langle \Phi_j(\mathbf{k}, \mathbf{r}) | H | \Phi_{j'}(\mathbf{k}, \mathbf{r}) \rangle}{\sum_{j,j'=1}^n C_{ij}^* C_{ij'} \langle \Phi_j(\mathbf{k}, \mathbf{r}) | \Phi_{j'}(\mathbf{k}, \mathbf{r}) \rangle}. \quad (1.4)$$

Let

$$S_{jj'}(\mathbf{k}) \equiv \langle \Phi_j(\mathbf{k}, \mathbf{r}) | \Phi_{j'}(\mathbf{k}, \mathbf{r}) \rangle, \quad (1.5)$$

$$H_{jj'}(\mathbf{k}) \equiv \langle \Phi_j(\mathbf{k}, \mathbf{r}) | H | \Phi_{j'}(\mathbf{k}, \mathbf{r}) \rangle, \quad (1.6)$$

*That is, a Linear Combination of Atomic Orbitals (LCAO), discussed and developed in Slater and Koster [26], Painter and Ellis [27].

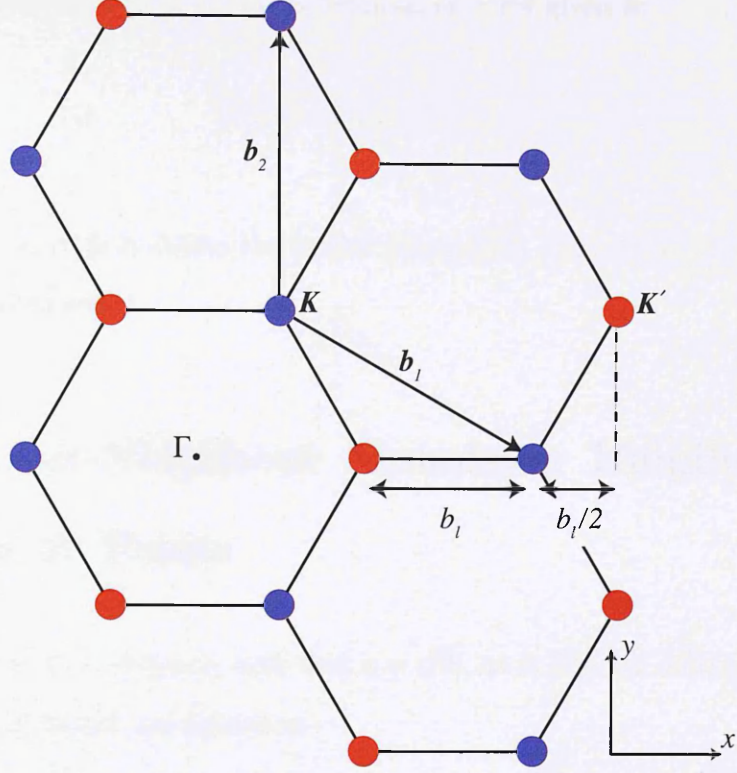


Fig. 1.2: Geometry of a hexagonal lattice in \mathbf{k} space, with sublattice A (B) sites shown in red (blue). $b_l = b/\sqrt{3}$, $\mathbf{K} = (-4\pi/3a, 0)$ and $\mathbf{K}' = (4\pi/3a, 0)$ relative to zero at the Γ point.

where $S_{jj'}(\mathbf{k})$ depends on the region where the wavefunctions overlap, and is known as the overlap integral matrix. $H_{jj'}(\mathbf{k})$ depends on the Bloch wavefunctions as well as the energy of the system, and is known as the transfer integral matrix. Rewriting Eqn. 1.4,

$$E_i(\mathbf{k}) = \frac{\sum_{j,j'=1}^n C_{ij}^*(\mathbf{k}) C_{ij'}(\mathbf{k}) H_{jj'}(\mathbf{k})}{\sum_{j,j'=1}^n C_{ij}^* C_{ij'} S_{jj'}}. \quad (1.7)$$

By fixing $H_{jj'}(\mathbf{k})$ and $S_{jj'}(\mathbf{k})$ for a certain \mathbf{k} , we can optimise C_{ij}^* to minimise $E_i(\mathbf{k})$, through partial derivatives, and arrive at the Schrödinger equation:

$$HC_i = E_i(\mathbf{k})SC_i, \quad (1.8)$$

with $C_i = (C_{i1}, C_{i2}, C_{i3}, \dots, C_{iN})$. Thus, $[H - E_i S]C_i = 0$, and if $[H - E_i S]^{-1}$ exists, $C_i = 0 \forall i$. So to find C_i we must solve the secular equation to get the

energy dispersion relation, to get all E_i eigenvalues for a given \mathbf{k} :

$$\det[H - E_i S] = 0. \quad (1.9)$$

To do this, we must first define the lattice parameters and vectors, required to describe the Hamiltonian.

1.2 Nearest-Neighbour Monolayer Hamiltonian Near K Points

We define l as the C–C distance, such that $a = \sqrt{3}l$, as in Fig. 1.1. Lattice vectors for the hexagonal lattice are defined as

$$\mathbf{a}_1 = (a, 0), \quad \mathbf{a}_2 = \left(\frac{a}{2}, \frac{\sqrt{3}a}{2} \right). \quad (1.10)$$

It is then easy to deduce that

$$\begin{aligned} \mathbf{b}_1 &= 2\pi \frac{\mathbf{a}_2 \times \mathbf{a}_3}{\mathbf{a}_1 \cdot (\mathbf{a}_2 \times \mathbf{a}_3)} = \left(\frac{2\pi}{a}, -\frac{2\pi}{\sqrt{3}a} \right), \\ \mathbf{b}_2 &= 2\pi \frac{\mathbf{a}_3 \times \mathbf{a}_1}{\mathbf{a}_1 \cdot (\mathbf{a}_2 \times \mathbf{a}_3)} = \left(0, \frac{4\pi}{\sqrt{3}a} \right), \end{aligned} \quad (1.11)$$

and the norm of $b_i = 4\pi/\sqrt{3}a$ (see Fig. 1.2).

We define two inequivalent points of high symmetry in \mathbf{k} space as $\mathbf{K} = (-4\pi/3a, 0)$ and $\mathbf{K}' = (4\pi/3a, 0)$ (also shown in Fig. 1.2). It can easily be seen that the nearest-neighbour distance in \mathbf{k} space is $b_l = b_l/2 + b_l/2 = b/\sqrt{3} = 4\pi/3a$. We can define the monolayer Hamiltonian[†] in two valleys \mathbf{K} and \mathbf{K}' as a matrix comprised of transfer integrals between nearest-neighbour atoms (in the basis

$$\Phi = (\phi_{AK}, \phi_{BK}, \phi_{BK'}, \phi_{AK'}):$$

[†]Ignoring intervalley scattering due to the symmetry of the lattice [28].

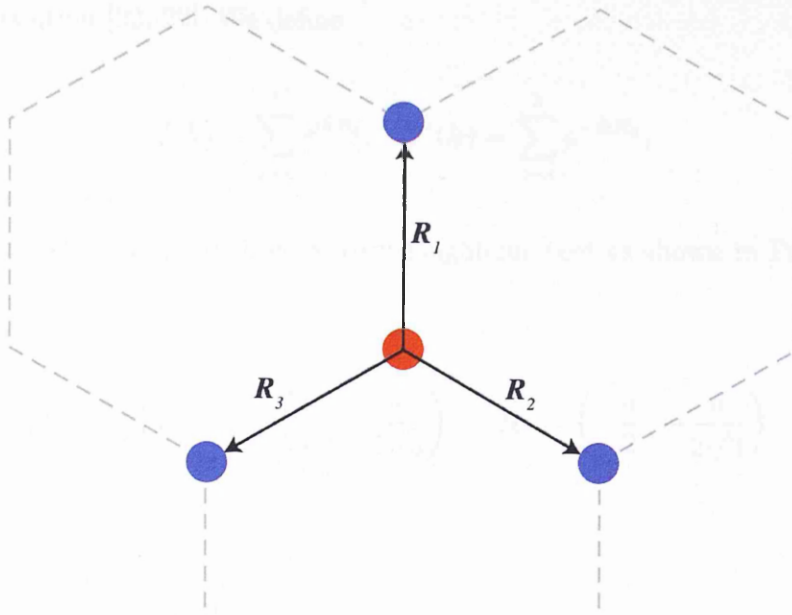


Fig. 1.3: Nearest-neighbour vectors. $\mathbf{R}_1 = (0, a/\sqrt{3})$, $\mathbf{R}_2 = (a/2, -a/2\sqrt{3})$, $\mathbf{R}_3 = (-a/2, -a/2\sqrt{3})$.

$$H_1 = \begin{pmatrix} H_{AKAK} & H_{AKBK} & 0 & 0 \\ H_{BKAK} & H_{BKBK} & 0 & 0 \\ 0 & 0 & H_{BK'BK'} & H_{BK'AK'} \\ 0 & 0 & H_{AK'BK'} & H_{AK'AK'} \end{pmatrix}. \quad (1.12)$$

Common terms can be pulled out of the integrals, to leave

$$H_1 = \begin{pmatrix} \epsilon & \sum_{j=1}^3 e^{-i\mathbf{k}\mathbf{R}_j}\gamma_0 & 0 & 0 \\ \sum_{j=1}^3 e^{i\mathbf{k}\mathbf{R}_j}\gamma_0 & \epsilon & 0 & 0 \\ 0 & 0 & \epsilon & \sum_{j=1}^3 e^{i\mathbf{k}\mathbf{R}_j}\gamma_0 \\ 0 & 0 & \sum_{j=1}^3 e^{-i\mathbf{k}\mathbf{R}_j}\gamma_0 & \epsilon \end{pmatrix}, \quad (1.13)$$

where

$$\gamma_0 = \langle \Phi(\mathbf{r} - \mathbf{R}_A) | H | \Phi(\mathbf{r} - \mathbf{R}_B) \rangle \equiv \langle \Phi(\mathbf{r} - \mathbf{R}_B) | H | \Phi(\mathbf{r} - \mathbf{R}_A) \rangle, \quad (1.14)$$

is the intralayer transfer integral (determined from Eqn. 1.6). Here we use the symbol γ_0 for the hopping energy, in line with the Slonczewski-Weiss-McClure

parameterisation [22, 29]. We define

$$f(\mathbf{k}) = \sum_{j=1}^3 e^{i\mathbf{k}\mathbf{R}_j}, \quad f^*(\mathbf{k}) = \sum_{j=1}^3 e^{-i\mathbf{k}\mathbf{R}_j}, \quad (1.15)$$

where $\mathbf{R}_j = \mathbf{R}_A - \mathbf{R}_B$ are three nearest-neighbour vectors shown in Fig. 1.3 and equal

$$\mathbf{R}_1 = \left(0, \frac{a}{\sqrt{3}}\right), \quad \mathbf{R}_2 = \left(\frac{a}{2}, -\frac{a}{2\sqrt{3}}\right), \quad \mathbf{R}_3 = \left(-\frac{a}{2}, -\frac{a}{2\sqrt{3}}\right), \quad (1.16)$$

such that

$$f(\mathbf{k}) = \sum_{j=1}^3 e^{i\mathbf{k}\mathbf{R}_j} = e^{ik_y a/\sqrt{3}} + 2e^{-ik_y a/2\sqrt{3}} \cos(k_x a/2). \quad (1.17)$$

Eqn. 1.17 can be Taylor expanded[‡] around \mathbf{K} and \mathbf{K}' , after we define $\mathbf{k} = \mathbf{K} + \mathbf{p}$ (the $\mathbf{k} \cdot \mathbf{p}$ method [22, 29, 30]). For example, around \mathbf{K} , $f(\mathbf{k})$ becomes

$$\begin{aligned} f(\mathbf{k}) \Big|_{\mathbf{K}} &\approx \frac{1}{2} i\sqrt{3} a k_y + \frac{\sqrt{3} a}{2} \underbrace{\left(k_x + \frac{4\pi}{3a}\right)}_{p_x} \\ &\approx \frac{i\sqrt{3} a}{2} p_y + \frac{\sqrt{3} a}{2} p_x \\ &\approx \frac{\sqrt{3} a}{2} (p_x + ip_y). \end{aligned} \quad (1.18)$$

$f(\mathbf{k})$ and its complex conjugate, in both valleys, are

$$\begin{aligned} f(\mathbf{k}) \Big|_{\mathbf{K}} &\approx \frac{\sqrt{3} a}{2} (p_x + ip_y), \\ f^*(\mathbf{k}) \Big|_{\mathbf{K}} &\approx \frac{\sqrt{3} a}{2} (p_x - ip_y), \\ f(\mathbf{k}) \Big|_{\mathbf{K}'} &\approx \frac{\sqrt{3} a}{2} (-p_x + ip_y), \\ f^*(\mathbf{k}) \Big|_{\mathbf{K}'} &\approx \frac{\sqrt{3} a}{2} (-p_x - ip_y). \end{aligned} \quad (1.19)$$

[‡]Dropping terms quadratic in momentum.

Thus, if we define the self-hopping energy $\epsilon = 0$, we recover the Dirac-Weyl-like Hamiltonian [5, 31–33], a form previously shown by Slonczewski and Weiss [22],

$$H_1 = \frac{\sqrt{3}a\gamma_0}{2} \begin{pmatrix} 0 & p_x - ip_y & 0 & 0 \\ p_x + ip_y & 0 & 0 & 0 \\ 0 & 0 & 0 & -p_x + ip_y \\ 0 & 0 & -p_x - ip_y & 0 \end{pmatrix} = v\Lambda_z \otimes \boldsymbol{\sigma} \cdot \mathbf{p}, \quad (1.20)$$

where $\Lambda_z = \sigma_z$ (the Pauli spin matrix) in the valley space[§], and $\boldsymbol{\sigma}$ is a vector comprising of the Pauli spin matrices σ_x and σ_y . The prefactor $\sqrt{3}a\gamma_0/2\hbar = v$ is (with \hbar included for correct SI units), the velocity of the carriers. Using values $a \approx 2.46 \cdot 10^{-10}$ m, $\gamma_0 \approx 3.0$ eV, and $\hbar \approx 1.05 \cdot 10^{-34}$ kg m² s⁻¹, we find that $v \approx 9.74 \cdot 10^5$ ms⁻¹ $\approx c/300$ [1, 35], where c is the speed of light in vacuum[¶].

1.2.1 Band Structure

The Hamiltonian in the \mathbf{K} valley can be written as

$$H = \begin{pmatrix} \epsilon & \gamma_0 f^*(\mathbf{k}) \\ \gamma_0 f(\mathbf{k}) & \epsilon \end{pmatrix}, \quad (1.21)$$

where ϵ is the self-hopping energy (since in the nearest-neighbour approximation, the next jump to a sublattice A site is too far).

We can repeat the same procedure as before in order to calculate the overlap matrix, $S_{ij} = \langle \Phi_i | \Phi_j \rangle$. S_{AA} and S_{BB} involve the overlap of the atom's wavefunction with itself (provided we ignore other atoms in the same sublattice as before), so this will produce a value of unity. Thus, $S_{AA} = S_{BB} = 1$, assuming that atomic wavefunctions are normalised. Since S must be Hermitian, $S_{BA} = S_{AB}^*$,

[§] \otimes is the Kronecker product of these matrices [34].

[¶] γ_0 has (given 1 eV = $1.6 \cdot 10^{-19}$ J) units of energy, kg m² s⁻².

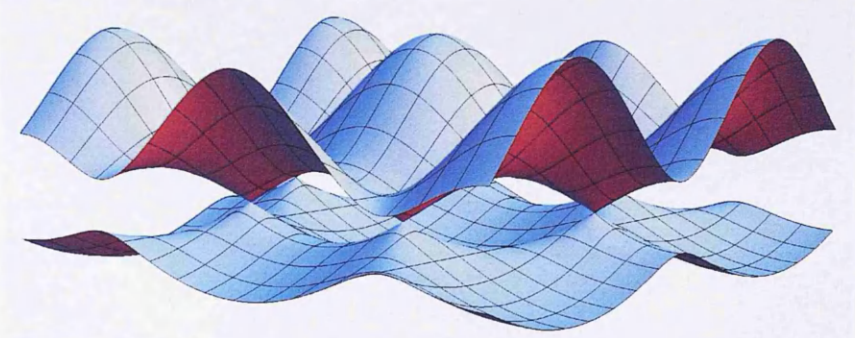


Fig. 1.4: Monolayer graphene band diagram in \mathbf{k} space, showing energy versus in-plane momentum. The hexagonal Brillouin zone and Dirac cones at each \mathbf{K} point are displayed. Eqn. 1.24 was plotted using values of $a = 0.142$ nm, $\gamma_0 = -3.033$ eV, $s = 0.129$ eV, and momentum range $\pm 2\pi/a$ [13, 27].

$$S = \begin{pmatrix} 1 & sf^*(\mathbf{k}) \\ sf(\mathbf{k}) & 1 \end{pmatrix}, \quad (1.22)$$

where s the overlap integral, defined in Eqn. 1.5. We can now solve the secular equation (Eqn. 1.9). Solving for E by substituting H and S ,

$$\begin{vmatrix} \epsilon - E & \gamma_0 f - E s f \\ \gamma_0 f^* - E s f^* & \epsilon - E \end{vmatrix}, \quad (1.23)$$

$$E = \frac{\epsilon \mp \gamma_0 |f|}{1 \mp s |f|}. \quad (1.24)$$

Eqn. 1.24 is used to plot Figs. 1.4 and 1.5; the latter clearly showing the hexagonal lattice structure. Empirical data has been used: $\epsilon = 0$, $\gamma_0 = -3.033$ eV, and $s = 0.129$ eV [13, 27].

We can calculate the energy of carriers near the \mathbf{K} point by calculating the determinant from the Schrödinger equation,

$$\begin{vmatrix} -\epsilon & p_x - ip_y \\ p_x + ip_y & -\epsilon \end{vmatrix} = 0. \quad (1.25)$$

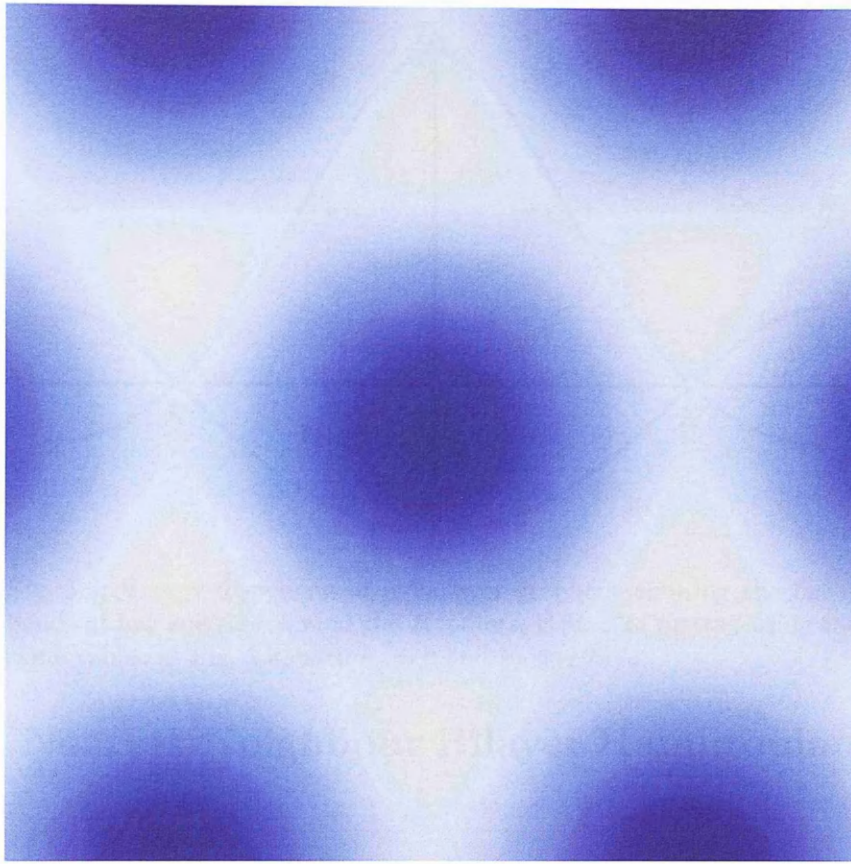


Fig. 1.5: Density plot of monolayer graphene band structure in k space, where the hexagonal lattice is clearly defined. Eqn. 1.24 plotted using the same values as in Fig. 1.4.

Thus,

$$\epsilon = \pm vp, \quad (1.26)$$

where $p = |\mathbf{p}| \equiv \sqrt{p_x^2 + p_y^2}$. Positive energy carriers are those in the conduction band, and those with negative energy reside in the valence band. This shows the linear dispersion relation at low energies near the K points, as shown in Fig. 1.6.

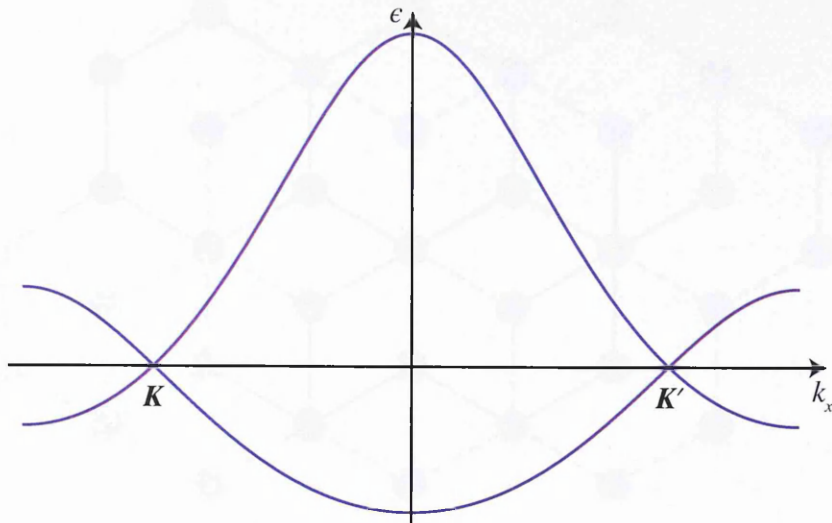


Fig. 1.6: Energy dispersion of monolayer graphene showing the linear bands at low energies around the K points. Eqn. 1.24 plotted using the same values as Fig. 1.4, with $k_y = 0$ and $k_x = \pm 2\pi/a$.

1.3 Nearest-Neighbour Bilayer Hamiltonian Near K Points

We model bilayer graphene as two weakly-coupled monolayers of graphite, separated by a distance of $c \approx 3.35 \text{ \AA}$ [22], and arranged in a Bernal stacking formation. That is, the A atoms in the top layer lie directly above the B atoms in the bottom layer [36]. Thus the unit cell consists of four inequivalent carbon atoms, using the notation A1, B1, A2, B2 to allow for two sublattices in both layers. To construct the tight binding Hamiltonian, we write it as the sum of a few distinct parts:

$$H_2 = H_{\text{mono}} + H_d + H_{\text{tw}}, \quad (1.27)$$

where H_{mono} is the monolayer Hamiltonian, Eqn. 1.13, written in the basis $\Phi_{\mathbf{K}} = (\phi_{A1}, \phi_{B2}, \phi_{A2}, \phi_{B1})$ around the \mathbf{K} point and $\Phi_{\mathbf{K}'} = (\phi_{B2}, \phi_{A1}, \phi_{B1}, \phi_{A2})$ around the \mathbf{K}' point. One minor complication is that we assume the on-site energies can be different on each layer. Thus we replace ϵ in Eqn. 1.13 with $-\Delta/2$ ($\Delta/2$) for layer one (two). In the basis $\Phi_{\mathbf{K}}$,

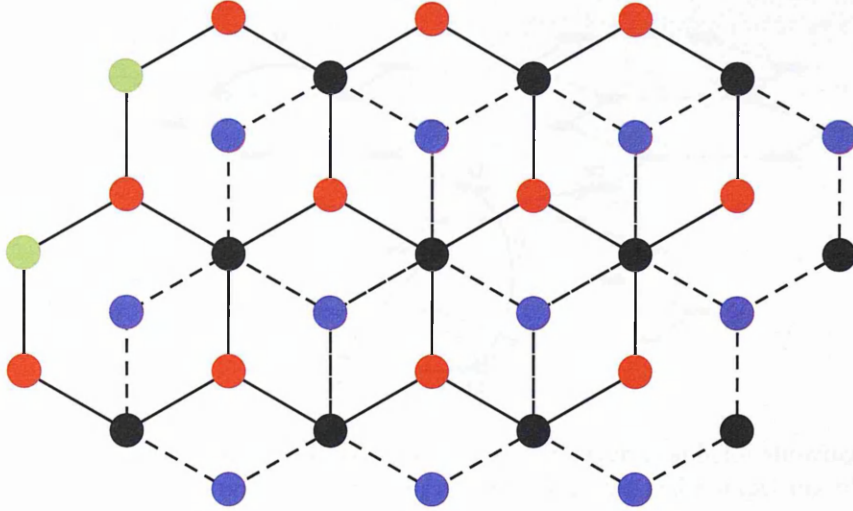


Fig. 1.7: Schematic of the bilayer graphene lattice with Bernal stacking. The bonds in the top (bottom) layer are indicated by dashed (solid) lines. Sublattice A (B) sites in the bottom layer are coloured red (green). The top layer sublattice A (B) sites are black (blue).

$$H_{\text{mono}} = \begin{pmatrix} -\Delta/2 & 0 & 0 & \sum_{j=1}^3 e^{-ikR_j} \gamma_0 \\ 0 & \Delta/2 & \sum_{j=1}^3 e^{ikR_j} \gamma_0 & 0 \\ 0 & \sum_{j=1}^3 e^{-ikR_j} \gamma_0 & \Delta/2 & 0 \\ \sum_{j=1}^3 e^{ikR_j} \gamma_0 & 0 & 0 & -\Delta/2 \end{pmatrix}, \quad (1.28)$$

and in basis $\Phi_{K'}$,

$$H_{\text{mono}} = \begin{pmatrix} \Delta/2 & 0 & 0 & \sum_{j=1}^3 e^{ikR_j} \gamma_0 \\ 0 & -\Delta/2 & \sum_{j=1}^3 e^{-ikR_j} \gamma_0 & 0 \\ 0 & \sum_{j=1}^3 e^{ikR_j} \gamma_0 & -\Delta/2 & 0 \\ \sum_{j=1}^3 e^{-ikR_j} \gamma_0 & 0 & 0 & \Delta/2 \end{pmatrix}. \quad (1.29)$$

Using the definitions in Eqns. 1.15 and 1.19, we can write

$$H_{\text{mono}} = \xi \begin{pmatrix} -\Delta/2 & 0 & 0 & v\pi^\dagger \\ 0 & \Delta/2 & v\pi & 0 \\ 0 & v\pi^\dagger & \Delta/2 & 0 \\ v\pi & 0 & 0 & -\Delta/2 \end{pmatrix}, \quad (1.30)$$

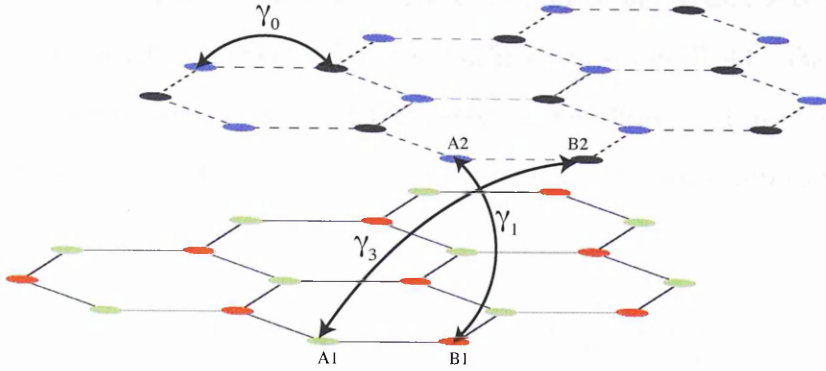


Fig. 1.8: Schematic of AB (Bernal) stacked bilayer graphene showing intralayer and interlayer couplings, as well as a unit cell comprising of four carbon atoms: A1, B1, A2, and B2.

where $\xi = +1(-1)$, serving as an index for the $\mathbf{K}(\mathbf{K}')$ valley, $\pi = p_x + ip_y$ (and π^\dagger is its complex conjugate^{ll}), and $v = \sqrt{3}a\gamma_0/2$, the velocity of quasiparticles for this transport mechanism.

H_d and H_{tw} are introduced to include two coupling mechanisms between the layers. Atoms B1 and A2 form a dimer state allowing for a direct hopping, which is parametrised by the transfer integral between these two atoms, $\gamma_1 = \langle \phi(\mathbf{r} - \mathbf{R}_{B1}) | H | \phi(\mathbf{r} - \mathbf{R}_{A2}) \rangle$. This has been measured experimentally to be around 0.4 eV (for bulk graphite) [12, 37–39]. Again, this parameterisation (and all parameters shown in Fig. 1.8) is that defined in Slonczewski and Weiss [22] and McClure [29]. In both valleys (and in both bases), H_d takes the form

$$H_d = \begin{pmatrix} 0 & 0 & 0 & 0 \\ 0 & 0 & 0 & 0 \\ 0 & 0 & 0 & \gamma_1 \\ 0 & 0 & \gamma_1 & 0 \end{pmatrix}. \quad (1.31)$$

There also exists another interlayer coupling, parametrised by the transfer integral γ_3 , which represents a direct hopping between sites A1 and B2. This term at low energies is responsible for deforming the Fermi circle into a triangular shape [38,

^{ll}The symbol π was originally defined in Slonczewski and Weiss [22] as $\frac{1}{\sqrt{2}}(p_x + ip_y)$.

40–42]. At energies around 1 meV the trigonal warping terms break the isoenergetic line into four pockets, an effect called the Lifshitz transition [7, 43]. The trigonal warping terms will not be further investigated in this thesis, but are included in this derivation for completeness. Thus, the trigonal warping component of the Hamiltonian is (in the basis $\Phi_{\mathbf{K}}$):

$$H_{\text{tw}} = \begin{pmatrix} 0 & \sum_{k=1}^3 e^{i\mathbf{k}\mathbf{R}_k} \gamma_3 & 0 & 0 \\ \sum_{k=1}^3 e^{-i\mathbf{k}\mathbf{R}_k} \gamma_3 & 0 & 0 & 0 \\ 0 & 0 & 0 & 0 \\ 0 & 0 & 0 & 0 \end{pmatrix}, \quad (1.32)$$

and in the basis $\Phi_{\mathbf{K}'}$,

$$H_{\text{tw}} = \begin{pmatrix} 0 & \sum_{k=1}^3 e^{-i\mathbf{k}\mathbf{R}_k} \gamma_3 & 0 & 0 \\ \sum_{k=1}^3 e^{i\mathbf{k}\mathbf{R}_k} \gamma_3 & 0 & 0 & 0 \\ 0 & 0 & 0 & 0 \\ 0 & 0 & 0 & 0 \end{pmatrix}. \quad (1.33)$$

We define

$$g(\mathbf{k}) = \sum_{k=1}^3 e^{i\mathbf{k}\mathbf{R}_k}, \quad g^*(\mathbf{k}) = \sum_{k=1}^3 e^{-i\mathbf{k}\mathbf{R}_k}, \quad (1.34)$$

and calculate $\sum_{k=1}^3 e^{i\mathbf{k}\mathbf{R}_k}$, where \mathbf{R}_k comprises of the three nearest-neighbour vectors $\mathbf{R}_{B2} - \mathbf{R}_{A1}$: $\mathbf{R}_1 = (0, -l, c)$, $\mathbf{R}_2 = (\sqrt{3}l/2, l/2, c)$, $\mathbf{R}_3 = (-\sqrt{3}l/2, l/2, c)$, where c is the interlayer distance.

Taylor expanding $g(\mathbf{k})$ around \mathbf{K} and \mathbf{K}' as for Eqn. 1.18, we find that $g(\mathbf{k})$ and its complex conjugate, in both valleys, are

$$\begin{aligned}
g(\mathbf{k})\Big|_{\mathbf{K}} &\approx \frac{\sqrt{3}a}{2} (p_x + ip_y), \\
g^*(\mathbf{k})\Big|_{\mathbf{K}} &\approx \frac{\sqrt{3}a}{2} (p_x - ip_y), \\
g(\mathbf{k})\Big|_{\mathbf{K}'} &\approx \frac{\sqrt{3}a}{2} (-p_x + ip_y), \\
g^*(\mathbf{k})\Big|_{\mathbf{K}'} &\approx \frac{\sqrt{3}a}{2} (-p_x - ip_y).
\end{aligned} \tag{1.35}$$

It is now easy to see that H_{tw} is

$$H_{\text{tw}} = \frac{\sqrt{3}a\gamma_3}{2}\xi \begin{pmatrix} 0 & \pi & 0 & 0 \\ \pi^\dagger & 0 & 0 & 0 \\ 0 & 0 & 0 & 0 \\ 0 & 0 & 0 & 0 \end{pmatrix}, \tag{1.36}$$

where again, $\xi = +1(-1)$ for valley \mathbf{K} (\mathbf{K}'). The final nearest-neighbour Hamiltonian for bilayer graphene is (from Eqn. 1.27)

$$H_2 = \xi \begin{pmatrix} -\Delta/2 & v_3\pi & 0 & v\pi^\dagger \\ v_3\pi^\dagger & \Delta/2 & v\pi & 0 \\ 0 & v\pi^\dagger & \Delta/2 & \xi\gamma_1 \\ v\pi & 0 & \xi\gamma_1 & -\Delta/2 \end{pmatrix}, \tag{1.37}$$

where $v_3 = \sqrt{3}a\gamma_3/2 \approx v/10$, the velocity of quasiparticles hopping directly between A1 and B2. ξ has been added as a coefficient to the γ_1 terms to ensure that their signs do not change when changing basis from \mathbf{K} to \mathbf{K}' .

1.3.1 Band Structure

In a similar fashion to the calculation in Section 1.2.1, we can calculate the energy of the carriers in order to plot the band structure of bilayer graphene. Calculating the determinant of the Schrödinger equation $|H_2 - \epsilon\mathbb{I}_4| = 0$ (where \mathbb{I}_4 is the 4x4 unit matrix), we solve for ϵ :

$$\begin{aligned}
\epsilon &= \pm \frac{1}{2} \sqrt{2\pi\pi^\dagger (2v^2 + v_3^2) + \Delta^2 + 2\gamma_1^2 \pm 2\sqrt{\Gamma}}, \text{ where} \\
\Gamma &= \pi\pi^\dagger (\pi\pi^\dagger v_3^2 (4v^2 + v_3^2) + 4v^2\Delta^2) + 4 (\pi^3 + (\pi^\dagger)^3) v^2 v_3 \gamma_1 \xi \\
&\quad + 2\pi\pi^\dagger (2v^2 - v_3^2) \gamma_1^2 + \gamma_1^4.
\end{aligned} \tag{1.38}$$

This can be simplified by squaring ϵ and using the notation $\epsilon_\pm^{(\alpha)}(p)$ to account for the first (second) “ \pm ” in Eqn. 1.38 in the subscript (superscript), noting that $p^2 = p_x^2 + p_y^2$ and $\mathbf{p} = p(\cos(\phi), \sin(\phi))$:

$$\begin{aligned}
\epsilon_\pm^{(\alpha)2}(p) &= p^2 \left(v^2 + \frac{v_3^2}{2} \right) + \frac{\Delta^2}{4} + \frac{\gamma_1^2}{2} + (-1)^\alpha \sqrt{\Omega}, \text{ where} \\
\Omega &= p^4 v_3^2 v^2 + \frac{p^4 v_3^4}{4} + p^2 v^2 \Delta^2 + 2p^3 v^2 v_3 \gamma_1 \xi \cos(3\phi) + p^2 \left(v^2 - \frac{v_3^2}{2} \right) \gamma_1^2 + \frac{\gamma_1^4}{4},
\end{aligned} \tag{1.39}$$

to be in agreement with McCann et al. [6]. The energy dispersion, shown in Fig. 1.9, consists of valley-degenerate bands: $\epsilon_-^{(\alpha)}$ ($\epsilon_+^{(\alpha)}$) terms are responsible for valence (conduction) bands, while $\alpha = 1$ (2) produces the low (high) energy bands. For the case of zero momentum it is noticed that $\epsilon_\pm^{(2)}(0) = \pm\sqrt{\gamma_1^2 + \Delta^2/4}$, and thus the high energy bands (formed by the B1 to A2 dimer bond) with no on-site energy asymmetry have a minimum at $\epsilon = \pm\gamma_1$. The low energy bands ($\epsilon_\pm^{(1)}(0) = \pm\sqrt{\Delta^2/4} = \pm\Delta/2$) touch at the \mathbf{K} point (when $\Delta = 0$), and can be split if an asymmetry in the on-site energies between layers is included [7, 44, 45]. This modulation and control of the electronic structure has been realised with gating [8, 37, 46–50].

1.4 Underlying Phenomena

1.4.1 Pseudospin and Chirality

In the monolayer graphene Hamiltonian (Eqn. 1.20), σ operates in the AB sublattice space (pseudospin). The projection of pseudospin onto momentum is known as

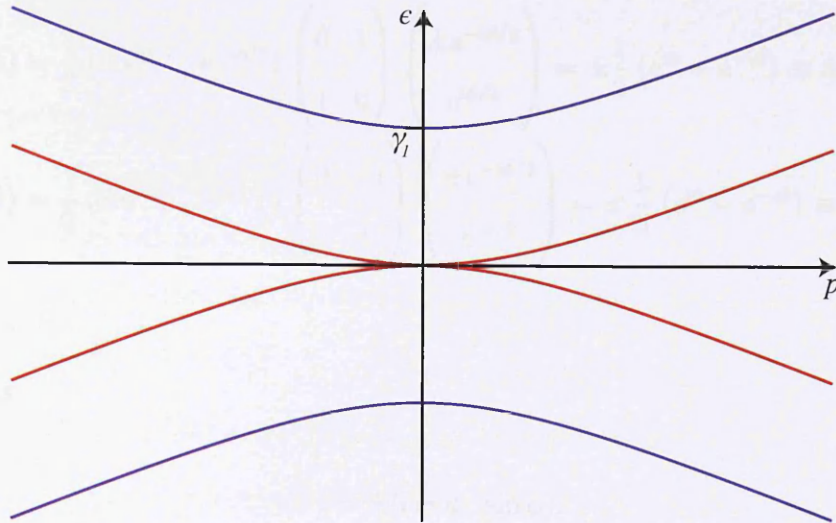


Fig. 1.9: Band structure of bilayer graphene, showing low (high) energy bands in red (blue). The high energy conduction band has a minimum at $\epsilon = \gamma_1$. Plotted using $\Delta = 0$, $\phi = 90^\circ$.

chirality, and hence quasiparticles in graphene are chiral [51–53]. The valley degree of freedom (also similar to spin) is highlighted if we write $H_1 = v\Lambda_z \otimes \boldsymbol{\sigma} \cdot \mathbf{p}$ (as in Eqn. 1.20)**. (Chirality is mirror-reflected for the \mathbf{K}' valley.) Pseudospin, given by $\langle \boldsymbol{\sigma} \rangle$, is physically interpreted as the weighting of the wavefunctions on either of the two sublattices, A and B. To explicitly calculate the form of the pseudospin we write the Schrödinger equation (in the \mathbf{K} valley) as

$$\begin{pmatrix} -\epsilon & \pi^\dagger \\ \pi & -\epsilon \end{pmatrix} \Phi = 0, \quad (1.40)$$

where $\epsilon = \pm vp$ (previously calculated in Section 1.2.1) and $\pi = p(\cos \phi + i \sin \phi) \equiv pe^{i\phi}$. Solving the eigenvector problem, we find that $\Phi = (1/\sqrt{2})(\pm e^{-i\phi}, 1)^T \equiv (1/\sqrt{2})(\pm e^{-i\phi/2}, e^{i\phi/2})^T$, where ϕ is a phase in momentum space.

The pseudospin components are calculated as $\langle \sigma_i \rangle = \langle \Phi | \sigma_i | \Phi \rangle$, where σ_i are the Pauli spin matrices. We find carriers in the conduction band in monolayer graphene exhibit pseudospin of the form

** Λ_z corresponds to the chirality of neutrinos in the Dirac-Weyl Hamiltonian [16].

$$\begin{aligned}
\langle \Phi | \sigma_x | \Phi \rangle &= \frac{1}{2} (\pm e^{i\phi/2}, e^{-i\phi/2}) \begin{pmatrix} 0 & 1 \\ 1 & 0 \end{pmatrix} \begin{pmatrix} \pm e^{-i\phi/2} \\ e^{i\phi/2} \end{pmatrix} = \pm \frac{1}{2} (e^{i\phi} + e^{-i\phi}) \equiv \pm \cos \phi, \\
\langle \Phi | \sigma_y | \Phi \rangle &= \frac{1}{2} (\pm e^{i\phi/2}, e^{-i\phi/2}) \begin{pmatrix} 0 & -i \\ i & 0 \end{pmatrix} \begin{pmatrix} \pm e^{-i\phi/2} \\ e^{i\phi/2} \end{pmatrix} = \pm \frac{1}{2i} (e^{i\phi} - e^{-i\phi}) \equiv \pm \sin \phi,
\end{aligned} \tag{1.41}$$

and thus

$$\langle \boldsymbol{\sigma} \rangle = \pm (\cos \phi, \sin \phi), \tag{1.42}$$

with no out of plane component. Given that the momentum is $\mathbf{p} = p(\cos \phi, \sin \phi)$, this means that the pseudospin is aligned (that is, parallel or anti-parallel) with the momentum. Since group velocity $\mathbf{v}_g = \partial_{\mathbf{p}} E$, \mathbf{v}_g and \mathbf{p} are parallel in the conduction band and anti-parallel in the valence band. Group velocity is parallel to the current operator, and hence $\boldsymbol{\sigma} \cdot \mathbf{p}/p = +1$ (-1) for the conduction (valence) band, changing at the Dirac point^{††}.

For bilayer graphene (using a low energy effective Hamiltonian, the first term in Eqn. 2.24), we find the effective dispersion relation $\epsilon = \pm p^2/2m$, where $m = \gamma_1/2v^2$. The solution of the equivalent eigenvector problem,

$$\begin{pmatrix} -p^2 & p^2 e^{-2i\phi} \\ p^2 e^{2i\phi} & -p^2 \end{pmatrix} \Phi = 0, \tag{1.43}$$

is $\Phi = (\pm e^{-i\phi}, e^{i\phi})^T$. The pseudospin, calculated in the same manner, is $\langle \boldsymbol{\sigma} \rangle = (\cos 2\phi, \sin 2\phi)$. Thus the pseudospin is always aligned at twice the angle of the momentum, parallel or anti-parallel. The consequence of introducing an asymmetry in the on-site energies between the two layers is discussed in Appendix C.

^{††}That is, $p(\sigma) = -p(-\sigma)$ in the conduction band, given that the linear dispersion is centered around the origin in momentum space.

1.4.2 Berry Phase

The phase associated with the rotation of pseudospin is interpreted as a Berry phase, an additional geometric phase acquired by quasiparticles traversing adiabatically around a closed loop [52, 54, 55]. Thus monolayer graphene exhibits Berry phase π [1, 52, 56], where carriers are massless and chiral (near the \mathbf{K} points where the $\mathbf{k} \cdot \mathbf{p}$ approximation applies).

Bilayer graphene exhibits (at low energies) a parabolic energy dispersion with Berry phase 2π [7, 8], giving massive chiral carriers. At the Lifshitz transition the four pockets in the energy spectrum have Berry phases π , $2\pi/3$, $2\pi/3$, and $-\pi/3$, thus consistent with the 2π phase at higher energies [7].

1.4.3 Klein Tunnelling

The relationship between pseudospin and momentum leads to a number of interesting phenomena, such as Klein tunnelling [9, 16, 57–59]. A sufficiently strong potential, though repulsive for electrons, can be attractive for hole states inside the barrier, and align in energy with the electron states outside. Applying a gate voltage over a strip of graphene, that region becomes doped, to form an n-p junction. At the interface between these two regions, carriers in the n region have positive energy (in the conduction band), while those in the p region have negative energy (in the valence band). Thus, a carrier moving from the n region to the p region will have the sign of its energy changed. Group velocity in monolayer graphene is (given Eqn. 1.26) $\mathbf{v}_g = \partial_{\mathbf{p}} E = \pm v \partial_{\mathbf{p}} p = \pm v$, and thus is independent of energy. A carrier travelling in a direction defined as positive will have a positive group velocity. To keep the sign of the carrier's group velocity fixed when passing through the interface, the sign of \mathbf{p} must change (since, during interband tunnelling, the sign of E does too). Thus, in the n region, \mathbf{v} and \mathbf{p} are parallel, while in the p region, they are anti-parallel. This leads to electron states in the n region becoming hole states in the p region, with unit transmission at zero angle of incidence. This is known

as Klein tunnelling, and is due to the suppression of backscattering [52, 60, 61]. In the n region, pseudospin is always aligned with momentum, so there is no state for backscattering to occur (with positive velocity but negative momentum). However, states just across the interface, with positive pseudospin and negative momentum, are allowed and available. This is assuming that the potential profile induced by the gate voltage does not alter pseudospin, which is true if the interface is smooth on the scale of the lattice constant. Thus, the potential does not differentiate between A and B sites, which is why it is added to the Hamiltonian as the product of a unit matrix. This phenomenon will be exploited for the case of bilayer graphene in Chapter 2, and for both monolayer and bilayer graphene in Chapter 3.

Chapter 2

Analysis of the Applicability of the Two-Band Model to Describe Transport Across n-p Junctions in Bilayer Graphene

2.1 Introduction

Gating of graphene enables one to vary the carrier density and therefore move the Fermi level from the conduction band to the valence band. Gating graphene flakes with multiple gates enables one to generate electrostatically defined n-p junctions [9, 57, 62–73]. Bilayer graphene in particular is often described by a four-band Hamiltonian from a tight-binding calculation (given that there are four atoms in the unit cell; see Fig. 2.1). For low energies near the Fermi surface (below 100 meV), we can describe the transport of electrons with a two-band Hamiltonian (see McCann and Fal’ko [7]). Transport across an n-p junction in bilayer graphene in the low energy ballistic regime has been previously studied by Katsnelson et al. [9], but without considering the possibility of a correction due to the spatial depen-

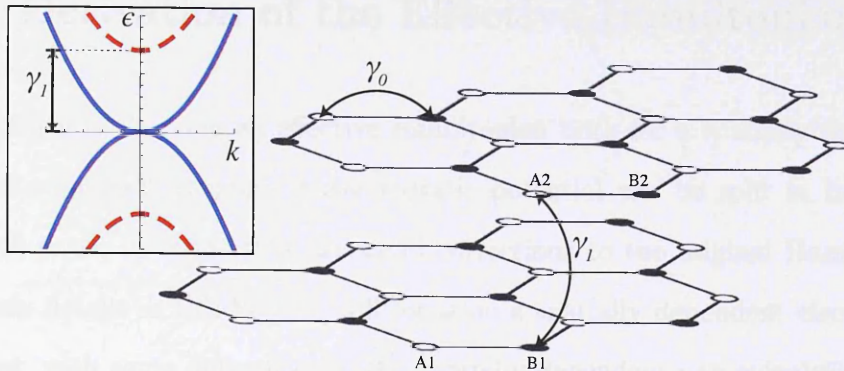


Fig. 2.1: Schematic of AB (Bernal) stacked bilayer graphene showing intra- and inter-layer couplings, as well as a unit cell comprising of four carbon atoms: A1, B1, A2, B2. Inset: energy bands in bilayer graphene near a \mathbf{K} point. The energy of the quasiparticles is near $\epsilon = 0$, qualifying the assumption that γ_1 is large compared to other energies in the system. The transformation reduces the band structure to blue (solid) bands only.

dence of the electrostatic potential. In this Chapter, we wish to test the suitability of this simpler model by extending the derivation of an effective two-band Hamiltonian for bilayer graphene (in the low energy regime) to include the effects of a spatially dependent electrostatic potential u , and a gap in the energy spectrum Δ . If these corrections are small, the two-band model is applicable to the calculation of transport across an n-p junction.

The re-derived two-band model Hamiltonian contains several additional terms which originate from the spatial derivatives of $u(x)$. We use this in the analysis of the problem of an n-p junction, where we find a change in transmission probability, as compared to the analysis in Katsnelson et al. [9], which showed perfect transmission through the n-p junction at an angle of 45° (see Fig. 2.3). This analysis shows that the additional terms in the effective two-band Hamiltonian induced by the gradient expansion involving the lateral potential are small, however the correctional term to the angular transmission probability increases the angle at which perfect transmission occurs by a few degrees. This also results in a small correction to the Fano factor.

2.2 Derivation of the Effective Hamiltonian

The problem of deriving an effective Hamiltonian both for a spatially dependent gap and a spatially dependent electrostatic potential can be split in two, since both will result in terms that are small corrections to the original Hamiltonian. The main details in this Section will focus on a spatially dependent electrostatic potential, with some differences in the spatially dependent gap calculation highlighted in Section 2.2.4. We are then free to combine the results to form the effective Hamiltonian.

The nearest-neighbour tight binding Hamiltonian around a \mathbf{K} point (for basis $\Phi_{\mathbf{K}} = (\phi_{A1}, \phi_{B2}, \phi_{A2}, \phi_{B1})$), derived in Section 1.3, is repeated here for convenience:

$$\mathcal{H}_{4 \times 4} = \begin{pmatrix} -\xi \frac{\Delta}{2} \sigma_z + \hat{u} & \xi v \boldsymbol{\sigma} \cdot \mathbf{p} \\ \xi v \boldsymbol{\sigma} \cdot \mathbf{p} & \xi \frac{\Delta}{2} \sigma_z + \gamma_1 \sigma_x + \hat{u} \end{pmatrix}, \quad (2.1)$$

where $\boldsymbol{\sigma} = (\sigma_x, \sigma_y)$, $\mathbf{p} = (p_x, p_y)$ and ξ is the Dirac point index ($\xi = +1$ for the valley around the \mathbf{K} point, and -1 for the valley around the \mathbf{K}' point). $v = \frac{\sqrt{3}}{2} a \gamma_0 / \hbar$, and σ_i are the Pauli spin matrices. Furthermore, $\Delta = \epsilon_2 - \epsilon_1$ is the difference between the on-site energies in the two layers, $\epsilon_2 = \frac{1}{2} \Delta$, $\epsilon_1 = -\frac{1}{2} \Delta$, which produces a gap in the energy spectrum [44]. A potential term $\hat{u} = \mathbb{I}u$ is added along the diagonal to represent the electrostatic potential (we neglect intervalley scattering between \mathbf{K} and \mathbf{K}' ; \mathbb{I} is the unit matrix). We assume that the interlayer coupling γ_1 is large compared to other energies in the system (which is reasonable for the low energy regime near the Dirac points). Given that $\epsilon \ll \gamma_1$ (where ϵ is the energy of charge carriers), and with $\epsilon = p^2/2m$, where $m = \gamma_1/2v^2$ [7], we see that $(pv/\gamma_1)^2 \ll 1$. From this justification, we drop terms beyond quadratic in momentum in the following calculations. We effectively assume a continuum system, with

$$a \ll l_1 \ll (\lambda_F, l), \quad (2.2)$$

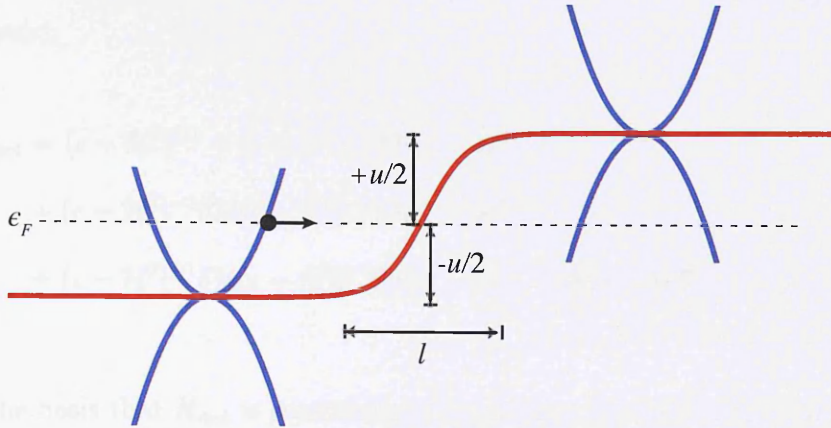


Fig. 2.2: Low-energy band structure of a single valley on either side of the potential step. The Fermi energy is the same on both sides, causing an electron from the left side to tunnel through the barrier from the conduction band to the valence band on the right side.

where a is the lattice constant, l is the width of the step (see Fig. 2.2), $l_{\perp} = v/\gamma_1^*$, and λ_F is the Fermi wavelength.

2.2.1 Schrieffer-Wolff Transformation

We use a Schrieffer-Wolff transformation [74] to map Eqn. 2.1 in a 4D Hilbert space into a 2D subspace, creating an effective Hamiltonian. The general scheme is to take $\mathcal{H}_{4 \times 4}$ and, using Green's functions, map it into a low energy subspace \mathcal{H}_{11} . This leads to the wavevectors no longer being orthonormal, which also has to be fixed.

If we let $\mathcal{H}_{4 \times 4} = \mathcal{H}^0 + \delta\mathcal{H}$, with

$$\mathcal{H}^0 = \begin{pmatrix} H_{11} & 0 \\ 0 & H_{22} \end{pmatrix}, \quad \delta\mathcal{H} = \begin{pmatrix} 0 & H_{12} \\ H_{21} & 0 \end{pmatrix}, \quad (2.3)$$

we can then write the associated Green's function as

$$\mathcal{G}_{4 \times 4} = (\epsilon - \mathcal{H}_{4 \times 4})^{-1} = (\epsilon - \mathcal{H}^0 - \delta\mathcal{H})^{-1}, \quad (2.4)$$

*The interlayer coupling length. This is the perpendicular distance at which interlayer interactions become important [64].

and expand:

$$\begin{aligned}
\mathcal{G}_{4\times 4} &= (\epsilon - \mathcal{H}^0)^{-1} + (\epsilon - \mathcal{H}^0)^{-1} \delta\mathcal{H} (\epsilon - \mathcal{H}^0)^{-1} \\
&+ (\epsilon - \mathcal{H}^0)^{-1} \delta\mathcal{H} (\epsilon - \mathcal{H}^0)^{-1} \delta\mathcal{H} (\epsilon - \mathcal{H}^0)^{-1} \\
&+ (\epsilon - \mathcal{H}^0)^{-1} \delta\mathcal{H} (\epsilon - \mathcal{H}^0)^{-1} \delta\mathcal{H} (\epsilon - \mathcal{H}^0)^{-1} \delta\mathcal{H} (\epsilon - \mathcal{H}^0)^{-1} + \dots . \quad (2.5)
\end{aligned}$$

Given the basis that $\mathcal{H}_{4\times 4}$ is constructed in, and that the low energy quasiparticle transport is directly from atom A1 to B2 in the bilayer unit cell [7] (see Fig. 2.1), we wish to map $\mathcal{H}_{4\times 4}$ onto the H_{11} block matrix, using a Schrieffer-Wolff transformation. To do this, we take each term of Eqn. 2.5 and map it to H_{11} . For example, starting with the first term, $(\epsilon - \mathcal{H}^0)^{-1}$, we realise that when mapping this we are really mapping to \mathcal{H}_{11}^0 . So we first write a subscript of 1 to specify that we are wanting the H_{11} subspace. There is only one item matching this for \mathcal{H}^0 , so we must write $(\epsilon - \mathcal{H}^0)_{11}^{-1}$. With the second term of Eqn. 2.5, $(\epsilon - \mathcal{H}^0)^{-1} \delta\mathcal{H} (\epsilon - \mathcal{H}^0)^{-1}$, we perform the same actions. Starting from the first instance of $(\epsilon - \mathcal{H}^0)^{-1}$, we again start by giving this a subscript of 1. Only \mathcal{H}_{11}^0 can match (again, since $\mathcal{H}_{12}^0 = 0$), so we write $(\epsilon - \mathcal{H}^0)_{11}^{-1}$. We now must perform the same action for $\delta\mathcal{H}$. The first number in the subscript must be a 1 given matrix multiplication rules. Hence, to avoid a trivial result (given $\delta\mathcal{H}_{11} = 0$), we let the subscript of $\delta\mathcal{H}$ become $\delta\mathcal{H}_{12}$. These actions are repeated for all terms in Eqn. 2.5, after which we throw away the compound terms that do not map to H_{11} . The remaining terms result in

$$\begin{aligned}
\mathcal{G}_{2\times 2} &= (\epsilon - \mathcal{H}^0)_{11}^{-1} + (\epsilon - \mathcal{H}^0)_{11}^{-1} \delta\mathcal{H}_{12} (\epsilon - \mathcal{H}^0)_{22}^{-1} \delta\mathcal{H}_{21} (\epsilon - \mathcal{H}^0)_{11}^{-1} \\
&+ (\epsilon - \mathcal{H}^0)_{11}^{-1} \delta\mathcal{H}_{12} (\epsilon - \mathcal{H}^0)_{22}^{-1} \delta\mathcal{H}_{21} (\epsilon - \mathcal{H}^0)_{11}^{-1} \delta\mathcal{H}_{12} (\epsilon - \mathcal{H}^0)_{22}^{-1} \delta\mathcal{H}_{21} (\epsilon - \mathcal{H}^0)_{11}^{-1} \\
&+ \dots . \quad (2.6)
\end{aligned}$$

There is a repeated pattern here, so let $\Sigma_{11} = \delta\mathcal{H}_{12} (\epsilon - \mathcal{H}^0)_{22}^{-1} \delta\mathcal{H}_{21}$, the self energy.

Hence,

$$\begin{aligned} \mathcal{G}_{2 \times 2} &= (\epsilon - \mathcal{H}^0)_{11}^{-1} + (\epsilon - \mathcal{H}^0)_{11}^{-1} \Sigma_{11} (\epsilon - \mathcal{H}^0)_{11}^{-1} \\ &\quad + (\epsilon - \mathcal{H}^0)_{11}^{-1} \Sigma_{11} (\epsilon - \mathcal{H}^0)_{11}^{-1} \Sigma_{11} (\epsilon - \mathcal{H}^0)_{11}^{-1} + \dots \end{aligned} \quad (2.7)$$

Again utilising the expansion $(1 - x)^{-1} = \sum_{n=0}^{\infty} x^n$, we can write $\mathcal{G}_{2 \times 2}$ as

$$\begin{aligned} \mathcal{G}_{2 \times 2} &= (1 + (\epsilon - \mathcal{H}^0)_{11}^{-1} \Sigma_{11} + [(\epsilon - \mathcal{H}^0)_{11}^{-1} \Sigma_{11}]^2 + \dots) (\epsilon - \mathcal{H}^0)_{11}^{-1} \\ &= (1 - (\epsilon - \mathcal{H}^0)_{11}^{-1} \Sigma_{11})^{-1} (\epsilon - \mathcal{H}^0)_{11}^{-1} \\ &= \frac{1}{(\epsilon - \mathcal{H}^0)_{11} (1 - (\epsilon - \mathcal{H}^0)_{11}^{-1} \Sigma_{11})} \\ &= \frac{1}{\epsilon - \mathcal{H}_{11}^0 - \Sigma_{11}} = G_{11}. \end{aligned} \quad (2.8)$$

Using the expression for the self energy,

$$G_{11}^{-1} = \epsilon - H_{11} - H_{12} (\epsilon - H_{22})^{-1} H_{21}, \quad (2.9)$$

which can be calculated with the block matrix values from Eqn. 2.3,

$$\begin{aligned} H_{11} &= -\xi \frac{\Delta}{2} \sigma_z + \mathbb{I}u, \\ H_{12} &= H_{21} = \xi v \boldsymbol{\sigma} \cdot \mathbf{p}, \\ H_{22} &= \xi \frac{\Delta}{2} \sigma_z + \sigma_x \gamma_1 + \mathbb{I}u. \end{aligned} \quad (2.10)$$

Given that we assume γ_1 is large compared to ϵ , u , and Δ , we can simplify $(\epsilon - H_{22})^{-1}$ in Eqn. 2.9:

$$\begin{aligned}
(\epsilon - H_{22})^{-1} &= \left(\epsilon - \left(\xi \frac{\Delta}{2} \sigma_z + \sigma_x \gamma_1 + \mathbb{I}u \right) \right)^{-1} \\
&= -\frac{1}{\gamma_1^2 - (\epsilon - \xi \frac{\Delta}{2} - u)(\epsilon + \xi \frac{\Delta}{2} - u)} \begin{pmatrix} \epsilon + \xi \frac{\Delta}{2} - u & \gamma_1 \\ \gamma_1 & \epsilon - \xi \frac{\Delta}{2} - u \end{pmatrix} \\
&= -\frac{1}{\gamma_1^2 \left[1 - \frac{(\epsilon - \xi \frac{\Delta}{2} - u)(\epsilon + \xi \frac{\Delta}{2} - u)}{\gamma_1^2} \right]} \begin{pmatrix} \epsilon + \xi \frac{\Delta}{2} - u & \gamma_1 \\ \gamma_1 & \epsilon - \xi \frac{\Delta}{2} - u \end{pmatrix} \\
&\approx \frac{1}{\gamma_1^2} \left(\mathbb{I}\epsilon + \sigma_z \xi \frac{\Delta}{2} - \mathbb{I}u + \sigma_x \gamma_1 \right). \tag{2.11}
\end{aligned}$$

Hence,

$$G_{11}^{-1} = \epsilon - H_{11} + \frac{1}{\gamma_1^2} H_{12} \epsilon H_{21} + \frac{\xi \Delta}{\gamma_1^2} H_{12} \sigma_z H_{21} - \frac{1}{\gamma_1^2} H_{12} \hat{u} H_{21} + \frac{1}{\gamma_1} H_{12} \sigma_x H_{21}. \tag{2.12}$$

This shows where the terms in the original effective Hamiltonian are coming from, with the addition of a term depending on the potential. Before substituting Eqn. 2.10 into this, we must ensure the wavefunctions are normalised.

2.2.2 Renormalising the Wavefunctions

The whole Hilbert space has now been projected onto the G_{11}^{-1} subspace. During this projection, the orthonormality of the wavevectors has to be preserved. To do this, we notice that G_{11}^{-1} in Eqn. 2.12 is an inverse Green's function of the form

$$G_{11}^{-1} = \epsilon - H_{11} + \Omega + \epsilon\beta, \tag{2.13}$$

where

$$\begin{aligned}
\beta &= \frac{1}{\gamma_1^2} H_{12} H_{21}, \\
\Omega &= \frac{\xi \Delta}{\gamma_1^2} H_{12} \sigma_z H_{21} - \frac{1}{\gamma_1^2} H_{12} \hat{u} H_{21} + \frac{1}{\gamma_1} H_{12} \sigma_x H_{21}.
\end{aligned}$$

Given that ϵ appears as a linear term, we can make a small shortcut[†]. Using Schrödinger's equation, $[\epsilon(1 + \beta) - H_{11} + \Omega]\psi = 0$, we see that an effective Schrödinger equation is

$$\epsilon(1 + \beta)|\psi\rangle = (H_{11} - \Omega)|\psi\rangle. \quad (2.14)$$

We wish to enforce normalisation and orthogonality of the wavefunctions, hence $\langle\psi|1 + \beta|\psi\rangle = |\psi|^2$ and $\langle\varphi|\psi\rangle = 0$. However, we have $\langle\varphi|1 + \beta|\psi\rangle = 0$, so the $1 + \beta$ part must be split between the two wavefunctions. It is easiest to split this evenly,

$$\langle\varphi|(1 + \beta)^{\frac{1}{2}}(1 + \beta)^{\frac{1}{2}}|\psi\rangle, \quad (2.15)$$

with β a Hermitian operator. We can write the new wavefunction as $\tilde{\psi}$ given

$$\underbrace{\langle\varphi|(1 + \beta)^{\frac{1}{2}}}_{\langle\tilde{\varphi}|} \underbrace{(1 + \beta)^{\frac{1}{2}}|\psi\rangle}_{|\tilde{\psi}\rangle}, \quad (2.16)$$

hence $|\psi\rangle = (1 + \beta)^{-\frac{1}{2}}|\tilde{\psi}\rangle$. Inserting this result into Eqn. 2.14 and multiplying on the left of both sides of the equation with $(1 + \beta)^{-\frac{1}{2}}$ (to orthonormalise), we find that

$$\epsilon|\tilde{\psi}\rangle = \underbrace{(1 + \beta)^{-\frac{1}{2}}(H_{11} - \Omega)(1 + \beta)^{-\frac{1}{2}}}_{H_{\text{eff}}}|\tilde{\psi}\rangle. \quad (2.17)$$

H_{eff} is the effective Hamiltonian for bilayer graphene given the assumption $\gamma_1 \gg \{\epsilon, \Delta, u\}$.

2.2.3 Form of the Effective Hamiltonian

Using Eqn. 2.17, we can calculate the effective Hamiltonian. This involves a Taylor expansion of $(1 + \beta)^{-\frac{1}{2}}$ up to the third power in β , given that we are only interested

[†]This would not be possible if we had, for instance, $\epsilon^2\beta$.

in going up to the second power in momentum (and adding the next term to make sure we do not miss anything). Rearranging and simplifying, we find that

$$H_{\text{eff}} = H_{11} - \Omega - \left\{ (H_{11} - \Omega), \frac{1}{2\gamma_1^2} H_{12} H_{21} \right\}, \quad (2.18)$$

where the curly braces denote the anticommutator. This equation can now be calculated. The right hand side of Eqn. 2.18 outside of the anticommutator becomes

$$H_{11} - \Omega = H_{11} - \frac{\xi \frac{\Delta}{2}}{\gamma_1^2} H_{12} \sigma_z \delta \mathcal{H}_{21} + \frac{1}{\gamma_1^2} H_{12} \hat{u} H_{21} - \frac{1}{\gamma_1} H_{12} \sigma_x H_{21}, \quad (2.19)$$

while the anticommutator becomes

$$\frac{v^2}{2\gamma_1^2} \left[\left(\begin{array}{cc} (u - \xi \frac{\Delta}{2}) \pi^\dagger \pi & 0 \\ 0 & (u + \xi \frac{\Delta}{2}) \pi \pi^\dagger \end{array} \right) + \left(\begin{array}{cc} \pi^\dagger \pi (u - \xi \frac{\Delta}{2}) & 0 \\ 0 & \pi \pi^\dagger (u + \xi \frac{\Delta}{2}) \end{array} \right) \right], \quad (2.20)$$

provided we ignore terms beyond quadratic in momentum.

Combining these results back into Eqn. 2.18, we construct H_{eff} and observe terms containing the potential,

$$\frac{1}{\gamma_1^2} H_{12} \hat{u} H_{21} - \frac{v^2}{2\gamma_1^2} \hat{u} \begin{pmatrix} \pi^\dagger \pi & 0 \\ 0 & \pi \pi^\dagger \end{pmatrix} - \frac{v^2}{2\gamma_1^2} \begin{pmatrix} \pi^\dagger \pi & 0 \\ 0 & \pi \pi^\dagger \end{pmatrix} \hat{u}. \quad (2.21)$$

The commutation relation between the momentum operator and the electrostatic potential is

$$[\boldsymbol{\sigma} \cdot \mathbf{p}, \hat{u}] \phi = \boldsymbol{\sigma} \cdot (-i \nabla) (\hat{u} \phi) - \hat{u} \boldsymbol{\sigma} \cdot (-i \nabla) \phi = [\boldsymbol{\sigma} \cdot \mathbf{p}, \hat{u}] = -i \boldsymbol{\sigma} (\nabla \hat{u}). \quad (2.22)$$

Using this, we recover the original low energy effective Hamiltonian for bilayer graphene in McCann and Fal'ko [7], with the addition of some terms arising from the influence of the potential.

$$\begin{aligned}
H_{\text{eff}} = & \overbrace{-\frac{v^2}{\gamma_1} \begin{pmatrix} 0 & (\pi^\dagger)^2 \\ \pi^2 & 0 \end{pmatrix} + \xi v_3 \begin{pmatrix} 0 & \pi \\ \pi^\dagger & 0 \end{pmatrix} - \xi \frac{\Delta v^2}{\gamma_1^2} \begin{pmatrix} -\pi^\dagger \pi & 0 \\ 0 & \pi \pi^\dagger \end{pmatrix} - \xi \frac{\Delta}{2} \begin{pmatrix} 1 & 0 \\ 0 & -1 \end{pmatrix}}^{\text{Original } H_{\text{eff}}} \\
& + \hat{u} - \frac{v^2}{2\gamma_1^2} \left[\mathbf{i}\boldsymbol{\sigma}(\nabla \hat{u}), \begin{pmatrix} 0 & \pi^\dagger \\ \pi & 0 \end{pmatrix} \right]. \tag{2.23}
\end{aligned}$$

The coefficient of the quadratic term in this effective Hamiltonian can be replaced by $-1/2m$, where m is given $m = \gamma_1/2v^2$. This Hamiltonian can be further refined by expanding the commutator it contains. Paying particular attention to which items the differential operators act on, and noting that $\partial_y \partial_x u - \partial_x \partial_y u$ should be zero if u is continuous, we can replace the commutator acting on wavefunction ψ with $-(\nabla^2 u)\psi + 2i\sigma_z[(\partial_x u)(\partial_y \psi) - (\partial_y u)(\partial_x \psi)]$. By further noting that p_z (momentum in the z direction) and $\partial_z u$ are zero for our system, we can rewrite the effective Hamiltonian as

$$\begin{aligned}
H_{\text{eff}} = & -\frac{1}{2m} \begin{pmatrix} 0 & (\pi^\dagger)^2 \\ \pi^2 & 0 \end{pmatrix} + \xi v_3 \begin{pmatrix} 0 & \pi \\ \pi^\dagger & 0 \end{pmatrix} - \xi \frac{\Delta v^2}{\gamma_1^2} \begin{pmatrix} -\pi^\dagger \pi & 0 \\ 0 & \pi \pi^\dagger \end{pmatrix} - \xi \frac{\Delta}{2} \begin{pmatrix} 1 & 0 \\ 0 & -1 \end{pmatrix} \\
& + \hat{u} + \frac{v^2}{2\gamma_1^2} [(\nabla^2 u) + 2\boldsymbol{\sigma}(\nabla u \times \mathbf{p})], \tag{2.24}
\end{aligned}$$

where the v_3 term is included for completeness[†].

2.2.4 Spatially-Dependent Gap in the Energy Spectrum

We can now repeat the same analysis with zero electrostatic potential, but with a spatially-dependent gap in the energy spectrum. For convenience the gap is written $\hat{\Delta} = \Delta \sigma_z$. As in the previous Section, we make a continuum approximation where the width of the barrier l is taken to be smooth on the scale of the lattice constant a , but sharp compared to the Fermi wavelength of the carriers. This means that

[†] $v_3 = (\sqrt{3}/2)a\gamma_3/\hbar$ is the velocity of quasiparticle transport across the indirect interlayer coupling γ_3 from atoms A1 to B2, and a is the lattice constant. This was originally defined in Section 1.3.

our calculations will be correct as long as the wavelength of the carriers does not rapidly change across the barrier. This ensures derivatives will be proper. The procedure outlined in Section 2.2 can be followed largely unchanged, with the exception that in Section 2.2.2, $\Omega = \frac{\xi}{2\gamma_1^2} \delta\mathcal{H}_{12} \hat{\Delta} \delta\mathcal{H}_{21} + \frac{1}{\gamma_1} \delta\mathcal{H}_{12} \sigma_x \delta\mathcal{H}_{21}$.

Following on from Eqn. 2.18, at all times dropping terms greater than quadratic in momentum, we obtain

$$H_{\text{eff}} = H_{11} - \frac{\xi v^2}{2\gamma_1^2} (\boldsymbol{\sigma} \cdot \mathbf{p}) \hat{\Delta} (\boldsymbol{\sigma} \cdot \mathbf{p}) - \frac{v^2}{\gamma_1} \begin{pmatrix} 0 & (\pi^\dagger)^2 \\ \pi^2 & 0 \end{pmatrix} + \frac{v^2 \xi}{4\gamma_1^2} \left\{ \hat{\Delta}, \begin{pmatrix} \pi^\dagger \pi & 0 \\ 0 & \pi \pi^\dagger \end{pmatrix} \right\}. \quad (2.25)$$

The last term can be expanded to give

$$\frac{v^2 \xi}{4\gamma_1^2} \left[2(\boldsymbol{\sigma} \cdot \mathbf{p}) \hat{\Delta} (\boldsymbol{\sigma} \cdot \mathbf{p}) + [\boldsymbol{\sigma} \cdot \mathbf{p}, [\boldsymbol{\sigma} \times (\nabla \Delta)]_{\hat{k}}] + [\boldsymbol{\sigma} \cdot \mathbf{p}, 2\Delta (\boldsymbol{\sigma} \times \nabla)_{\hat{k}}] \right], \quad (2.26)$$

where the vector products operate in a space with three unit vectors $\hat{i}, \hat{j}, \hat{k}$. Cancelling terms, we have the equation

$$H_{\text{eff}} = H_{11} - \frac{v^2}{\gamma_1} \begin{pmatrix} 0 & (\pi^\dagger)^2 \\ \pi^2 & 0 \end{pmatrix} + \frac{v^2 \xi}{4\gamma_1^2} \left([\boldsymbol{\sigma} \cdot \mathbf{p}, [\boldsymbol{\sigma} \times (\nabla \Delta)]_{\hat{k}}] + [\boldsymbol{\sigma} \cdot \mathbf{p}, 2\Delta (\boldsymbol{\sigma} \times \nabla)_{\hat{k}}] \right). \quad (2.27)$$

We calculate the commutators to be

$$\begin{aligned} [\boldsymbol{\sigma} \cdot \mathbf{p}, \hat{\Delta}] &= [\boldsymbol{\sigma} \times (\nabla \Delta)]_{\hat{k}} + 2\Delta (\boldsymbol{\sigma} \times \nabla)_{\hat{k}}, \\ [\boldsymbol{\sigma} \cdot \mathbf{p}, [\boldsymbol{\sigma} \times (\nabla \Delta)]_{\hat{k}}] &= -\sigma_z (2(\nabla \Delta) \cdot \nabla + (\nabla^2 \Delta)), \\ [\boldsymbol{\sigma} \cdot \mathbf{p}, 2\Delta (\boldsymbol{\sigma} \times \nabla)_{\hat{k}}] &= 2\mathbb{I}(\nabla \Delta) \times \mathbf{p} - \sigma_z (4\Delta \nabla^2 + 2(\nabla \Delta) \cdot \nabla). \end{aligned} \quad (2.28)$$

Substituting these into Eqn. 2.27 we have the final effective Hamiltonian,

$$\begin{aligned}
H_{\text{eff}} = & -\frac{v^2}{\gamma_1} \begin{pmatrix} 0 & (\pi^\dagger)^2 \\ \pi^2 & 0 \end{pmatrix} + \xi v_3 \begin{pmatrix} 0 & \pi \\ \pi^\dagger & 0 \end{pmatrix} - \xi \frac{\Delta}{2} \sigma_z \\
& + \frac{v^2 \xi}{4\gamma_1^2} (2\mathbb{I}(\nabla\Delta) \times \mathbf{p} - \sigma_z (4((\nabla\Delta) \cdot \nabla + \Delta\nabla^2) + (\nabla^2\Delta))). \quad (2.29)
\end{aligned}$$

2.2.5 Combined Effective Hamiltonian

This can be combined with Eqn. 2.24 to obtain the full effective Hamiltonian with a spatially-dependent electrostatic potential and a spatially-dependent gap in the energy spectrum. Thus the effective Hamiltonian is

$$\begin{aligned}
H_{\text{eff}} = & -\frac{1}{2m} [\sigma_x (-k_y^2 - \partial_x^2) + 2i\sigma_y k_y \partial_x] + \xi \frac{\Delta v^2}{\gamma_1^2} |\mathbf{p}|^2 \sigma_z - \xi \frac{\Delta}{2} \sigma_z + \hat{u} \\
& + \frac{v^2}{2\gamma_1^2} [(\nabla^2 u) + 2\boldsymbol{\sigma}(\nabla u \times \mathbf{p})] \\
& + \frac{v^2 \xi}{4\gamma_1^2} [2\mathbb{I}(\nabla\Delta) \times \mathbf{p} - \sigma_z \{4((\nabla\Delta) \cdot \nabla + \Delta\nabla^2) + (\nabla^2\Delta)\}]. \quad (2.30)
\end{aligned}$$

The first two lines form the Hamiltonian found in McCann and Fal'ko [7] (neglecting trigonal warping by setting $v_3 = 0$, since $\gamma_3 \ll \gamma_1$ [6]). The additional correctional terms arise from the spatial dependence of u and Δ .

2.3 Approximation of the Hamiltonian

The effective Hamiltonian in Eqn. 2.30 can be simplified when $\lambda_F \gg l$. Terms with $|\mathbf{p}|^2 \sim k_F^2$ can be dropped, given the length scales in this regime and the de Broglie relation. Now we wish to compare terms containing the potential u and gap Δ . To do this, we follow a simplified scheme to that defined in McCann [44], modelling the bilayer on a substrate as a parallel plate capacitor.

Each layer of graphene has surface area A , and we take the dielectric constants of the material between the back gate and layer one, and the bilayer, to be unity. Layer one has charge $Q = -n_1 e A$, while layer two has charge $Q' = -n_2 e A$, where n_1 (n_2)

is the density on layer one (two) (and $n = n_1 + n_2$). The back gate and layer one are separated by a distance L_b , while the two layers are separated by a distance c_0 . Applying a Gaussian surface around layer one, the magnitude of the electric field is $E = Q/\epsilon_0 A$, where ϵ_0 is the permittivity of free space. The voltage due to this electric field is thus $QL_b/\epsilon_0 A$. The electric potential energy due to the back gate (thus, the potential u) is $u = eQL_b/\epsilon_0 A = n_1 e^2 L_b/\epsilon_0$. We assume that the electric field from the back gate is screened poorly by layer one, so applying the same analysis to layer two, we find that the magnitude of the electric field is $E' = Q'/\epsilon_0 A$. The voltage produced by that electric field is $V' = E' c_0$, so the electric potential energy between the graphene layers (i.e., the gap) is $\Delta = n_2 e^2 c_0/\epsilon_0$. If we assume that the charge density is evenly distributed between the layers, $n_1 = n_2 = n/2$, then $u/\Delta = L_b/c_0$. With $c_0 \sim 0.3$ nm and $L_b \sim 300$ nm, we find that $u \gg \Delta$. By writing H_{eff} in the form $H_{\text{eff}} = \mathbb{I}A + \sigma_x B + \sigma_y C + \sigma_z D$, we compare each term and keep only the largest one in each group A, B, C, D . This produces an approximate Hamiltonian,

$$H_{\text{app}} = -\frac{1}{2m} [\sigma_x (-k_y^2 - \partial_x^2) + 2i\sigma_y k_y \partial_x] + \mathbb{I} \frac{k_F^2}{2m} \left[u + \frac{v^2}{2\gamma_1^2} \eta (\partial_x^2 u) \right] + \sigma_z \left[-\xi \frac{\Delta}{2} + \eta \frac{v^2 k_F^2}{2m\gamma_1^2} (\partial_x u) k_y \right], \quad (2.31)$$

where $\eta \in \{0, 1\}$ and highlights the correctional terms. In the following Section we analyse the effects of these terms, after assuming zero band gap (the effects of which are discussed in the conclusion).

2.4 Analysis of the n-p Junction

An n-p junction can be formed with two back gates, schematically shown in Fig. 2.3. Each gate can independently create an electrostatic potential over that region of bilayer graphene. Given our chosen length scales in Eqn. 2.2, we model the n-p junction as a Heaviside step function $\Theta(x) - (1/2)$, with its derivative the

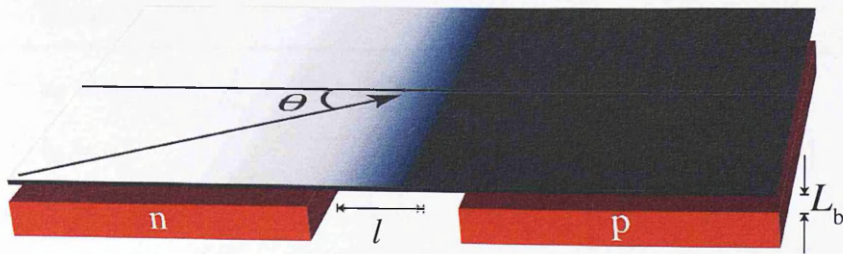


Fig. 2.3: Angular dependence of quasiparticle transmission through an n-p junction.

Dirac delta function. Thus, $u \approx (k_F^2/2m)[\Theta(x) - (1/2)]$, which also determines all additional terms in Eqn. 2.30.

We define the problem in terms of plane waves on the left-hand and right-hand sides of the junction, ψ_1 and ψ_2 respectively:

$$\begin{aligned}\psi_1 &= \begin{pmatrix} 1 \\ a_2 \end{pmatrix} e^{ik_x x} + b \begin{pmatrix} 1 \\ b_2 \end{pmatrix} e^{-ik_x x} + c \begin{pmatrix} 1 \\ c_2 \end{pmatrix} e^{-\kappa x}, \\ \psi_2 &= d \begin{pmatrix} 1 \\ d_2 \end{pmatrix} e^{-ik'_x x} + f \begin{pmatrix} 1 \\ f_2 \end{pmatrix} e^{\kappa' x}.\end{aligned}\quad (2.32)$$

The values for the pseudospin elements and momenta are determined by substituting these expressions for the wavefunction into the Schrödinger equation (in the asymptotic limit), and are given in Table 2.1. The Hamiltonian in Eqn. 2.30 has plane and evanescent wave solutions, and the quasiparticles are chiral, such that when they pass from the conductance band at the left of the interface to the valence band at the right, k_x changes sign [9] (see Fig. 2.2).

With the step defined to be at $x = 0$, we integrate Eqn. 2.31 across it,

$$\int_{0-\delta}^{0+\delta} (\epsilon - H_{\text{app}}) dx, \quad (2.33)$$

and take the limit $\delta \rightarrow 0$. Matching the wavefunctions at either side of the junction ($\psi_1(0) = \psi_2(0)$), we obtain the boundary condition [75]

Element	Momenta
$a_2 = \frac{1}{\epsilon-(u/2)} \left(\frac{k_y^2}{2m} - \frac{k_x^2}{2m} + \frac{ik_x k_y}{m} \right)$	$k_x = \sqrt{-k_y^2 + 2m[(u/2) - \epsilon]}$
$b_2 = a_2^*$	$k'_x = \sqrt{-k_y^2 + 2m[(u/2) + \epsilon]}$
$c_2 = \frac{1}{\epsilon-(u/2)} \left(\frac{k_y^2}{2m} + \frac{\kappa^2}{2m} - \frac{\kappa k_y}{m} \right)$	$\kappa = \sqrt{k_y^2 + 2m[(u/2) - \epsilon]}$
$d_2 = \frac{1}{\epsilon+(u/2)} \left(\frac{k_y^2}{2m} - \frac{k_x'^2}{2m} - \frac{ik'_x k_y}{m} \right)$	$\kappa' = -\sqrt{k_y^2 + 2m[(u/2) + \epsilon]}$
$f_2 = \frac{1}{\epsilon+(u/2)} \left(\frac{k_y^2}{2m} + \frac{\kappa'^2}{2m} + \frac{\kappa' k_y}{m} \right)$	

Table 2.1: Pseudospin elements and their corresponding momenta values.

$$0 = -\frac{\sigma_x}{2m} (\partial_x \psi) \Big|_{\psi_1(0)}^{\psi_2(0)} + \mathbb{I} \eta \frac{k_F^2 v^2}{4m \gamma_1^2} \left(\frac{\psi_1'(0) + \psi_2'(0)}{2} \right) - \sigma_z \eta \frac{v^2 k_F^2 k_y}{2m \gamma_1^2} \psi(0), \quad (2.34)$$

where the Fermi momentum $k_F = \sqrt{k_x^2 + k_y^2}$. We use these equations to calculate the transmission probability for a symmetric junction $T(k_y) = |d|^2$. We assume a wide strip, such that k_y is invariant, and also set $\epsilon = 0$ in the middle of the barrier for simplicity. Using $k_y = k_F \sin(\theta)$ (see Fig. 2.3) we first calculate the transmission with only the leading-order terms in Eqn. 2.34 (by setting $\eta = 0$), finding agreement with Katsnelson et al. [9] in that $T(\theta) = \sin^2(2\theta)$ (and thus obtaining perfect transmission at $\theta = 45^\circ$). Including the correctional terms from Eqn. 2.34 by setting $\eta = 1$, we obtain a correction to the incident angle at which perfect transmission is seen (see Fig. 2.4). Taylor expanding the full analytical result for $T(\theta)$ around η , we find that only the first-order term is important and obtain a potential-dependent result (providing a good fit up to $u \approx 50$ meV):

$$T(\theta) \cong \sin^2(2\theta) - \frac{2u}{3\gamma_1} \sin(4\theta) \sin(\theta). \quad (2.35)$$

This term is small compared to the leading order term (since in this approximation $\gamma_1 \gg u$), and so the correction to the transmission is also small. It is also of interest to determine the influence of corrections to the conductance and Fano factor. This forms the content of the following Section.

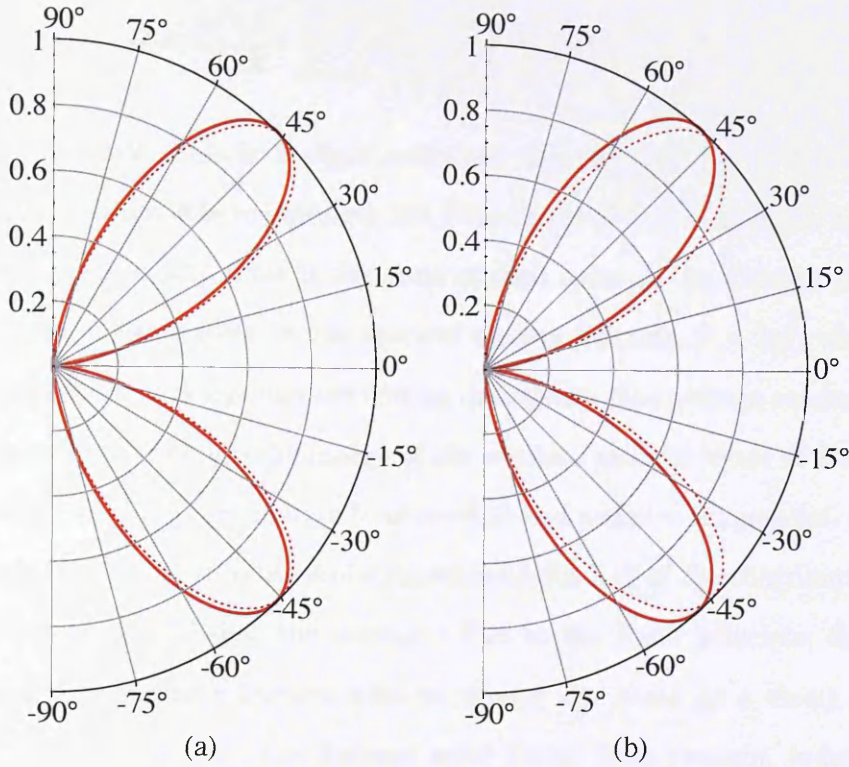


Fig. 2.4: Transmission probability through an n-p junction. The solid (dashed) line is with (without) correctional terms. Without correctional terms there is perfect transmission at an angle of 45° to the interface. (a) Transmission at $u = 40$ meV. (b) Transmission at $u = 80$ meV. Plotted with $\epsilon = 0$, $v \approx c/300$, $\gamma_1 = 0.4$ eV, $m = 0.035 m_e$, and $\Delta = 0$.

2.5 Conductance and Fano Factor

Assuming a wide graphene sheet (that is, a width w much greater than the length) and coherent quasiparticles, one can calculate the conductance from the transmission probability using the Landauer-Büttiker approach [76] (taking into account two valleys and two spins, with n channels),

$$G = \frac{4e^2}{h} \sum_n |t_n|^2. \quad (2.36)$$

Since the barrier is along the y axis, this component of momentum k_y is conserved so we can impose periodic boundary conditions: $k_y = 2\pi n/w$, where n is an integer and w is the width of the system. We convert the sum into an integral and calculate conductivity using the full numerical transmission probability,

$$G = \frac{4e^2wk_F}{2\pi h} \int_{-\pi/2}^{\pi/2} d\theta \cos(\theta)T(\theta) \cong 2.10 \frac{e^2wk_F}{\pi h}, \quad (2.37)$$

with $u = 40$ meV. This is a slight reduction from $2.12 e^2wk_F/\pi h$ for the case $\eta = 0$. It is also possible to calculate the Fano factor [77] $F = S/S_p$ for the same parameters numerically. This is the ratio of shot noise, S , to Poisson noise, S_p [78–80]. Shot noise is given by the spectral density function $S = 2q\bar{I}$, where \bar{I} is the average count of charge carriers flowing in a system (the average conductance), and proportional to G . q is the charge of the carriers, and the factor of 2 is due to (on average) an equal contribution from positive and negative frequencies. (i.e., for the simple case of the current oscillating sinusoidally, half of the contributions are from above and half below the average.) Due to the Pauli principle, the noise is reduced (since charge carriers wish to occupy one state at a time), and so $S \propto \sum_n T_n(1 - T_n)$ [81]. The Poisson noise (noise from random, independent events) has no such constraint, and thus $S_p \propto \sum_n T_n$. Hence, the Fano factor is simply related to the transmission:

$$F = \frac{\int_{-\pi/2}^{\pi/2} d\theta \cos(\theta)T(\theta)(1 - T(\theta))}{\int_{-\pi/2}^{\pi/2} d\theta \cos(\theta)T(\theta)} \cong 0.241. \quad (2.38)$$

A Fano factor near zero would indicate more deterministic transport, while a Fano factor approaching unity corresponds to a Poisson process. Our results show a small increase compared to $F \cong 0.238$ when $\eta = 0$ (see Fig. 2.5).

2.6 Conclusion

We have extended the earlier derived low energy effective Hamiltonian for bilayer graphene to incorporate a spatially dependent electrostatic potential consistently. We calculate the angle-dependent transmission through an n-p junction and find $T(\theta) \cong \sin^2(2\theta) - (2u/3\gamma_1) \sin(4\theta) \sin(\theta)$. Perfect transmission is still seen, but at a slightly increased angle. The conductance is slightly reduced to

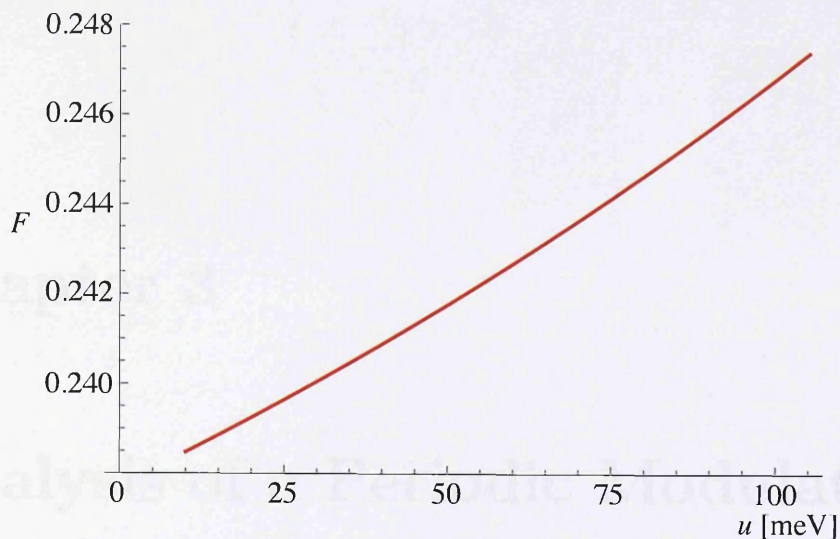


Fig. 2.5: Fano factor as a function of u , from a numerical calculation of the transmission probability for the same parameters as given in Fig. 2.4.

$G \cong 2.10 e^2 w k_F / \pi h$, whereas the Fano factor is slightly increased to $F \cong 0.241$ (both for $u = 40$ meV). Thus, the effective Hamiltonian derived in McCann and Fal'ko [7] is a very good approximation, as the correctional terms derived in this Chapter are small. Additionally, a low energy effective Hamiltonian with a spatially dependent asymmetry in the on-site energy between layers is derived. A gap in the electronic spectrum (induced by an external electrostatic potential) could be modulated to create a transport channel, and is a possible avenue of further research (with the derived correctional terms). The ability to open a gap in the electronic spectrum is exciting, as it enables the creation of an effective switchable field effect transistor, something more readily exploitable in bilayer graphene than monolayer graphene. The term containing Δ in Eqn. 2.31 (responsible for a difference in the on-site energies between sites A1 and B2) was dropped from later analysis given the length scales used. Transmission of charge carriers at energies inside the gap will be suppressed since there are no states to be occupied when tunnelling across the n-p junction. This should not affect the results of the calculation of transmission (and thus also conductance) presented here as charge carriers are considered with an energy in the middle of the interface, thus the shift in energy would be $u/2 \rightarrow (u - \Delta)/2$, which can be assumed to be negligible.

Chapter 3

Analysis of a Periodic Modulation of the Potential Profile in Monolayer and Bilayer Graphene

In this Chapter we analyse a low energy graphene system where a periodically-modulated potential is added to the Hamiltonian (see Fig. 3.1). We can analyse this system by considering it to consist of a series of n-p-n junctions, a construction developed by Kronig and Penney [82]. This model system was originally conceptualised to represent a sequence of atoms. Sometimes the potential walls are considered as delta functions to simplify calculations (e.g., Kittel [83]), but here they are considered to have finite width.

The work focuses on the analysis of the energy dispersion in monolayer and bilayer graphene when a periodic modulation of potential is added to the respective low energy Hamiltonian. We also analyse caustics and cusps in a system with a periodic potential and characterise their influence on the energy dispersion. The analysis involves the use of transfer matrices, so this formalism is explained first.

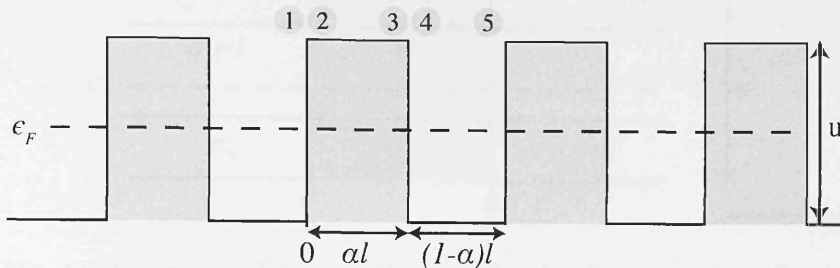


Fig. 3.1: Schematic showing a periodic profile of height u , separated by wells of width $(1 - \alpha)l$ (where $\alpha \in (0, 1)$). The Fermi energy ϵ_F is defined to be in the centre of the barrier. Regions one to five are indicated.

3.1 Transfer Matrix Formalism

Transfer matrices make it easy to calculate the transmission across multiple n-p junctions. They do this by relating the wavefunctions on one side of an interface (or set of interfaces) to the other. For example, a transfer matrix could be constructed to relate the wavefunctions in region one in Fig. 3.1, to those in region four. In this Section we derive the transfer matrices to calculate transmission through an n-p-n junction in monolayer and bilayer graphene, before applying this to the case of an infinite array of junctions.

3.1.1 Monolayer Graphene

The monolayer graphene Hamiltonian is defined in Eqn. 1.20 as

$$H_1 = -\hbar v \boldsymbol{\sigma} \cdot \mathbf{p}. \quad (3.1)$$

We define a one-dimensional n-p-n junction as in Fig. 3.2. If we assume a quasi-particle described as a plane wave with unity amplitude to approach from the left of the system, there are two things that can happen at the first interface. It can reflect back (with amplitude a_2), or transmit through (with amplitude b_1). At the second interface the same situation arises, giving reflection amplitude b_2 and transmission amplitude c_1 . We neglect incidence from the right of the system. The

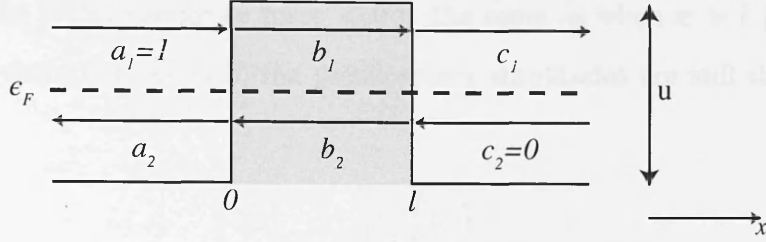


Fig. 3.2: Schematic of an n-p-n junction in monolayer graphene in one dimension, with interfaces at $x = 0$ and $x = l$.

wavefunctions are therefore of the form

$$\begin{aligned}\psi_1 &= a_1 \begin{pmatrix} 1 \\ a_{12} \end{pmatrix} e^{ik_x x} + a_2 \begin{pmatrix} 1 \\ a_{22} \end{pmatrix} e^{-ik_x x}, \\ \psi_2 &= b_1 \begin{pmatrix} 1 \\ b_{12} \end{pmatrix} e^{ik_x x} + b_2 \begin{pmatrix} 1 \\ b_{22} \end{pmatrix} e^{-ik_x x}.\end{aligned}\quad (3.2)$$

At the first interface ($x = 0$) the amplitudes must be equal:

$$a_1 \begin{pmatrix} 1 \\ a_{12} \end{pmatrix} + a_2 \begin{pmatrix} 1 \\ a_{22} \end{pmatrix} = b_1 \begin{pmatrix} 1 \\ b_{12} \end{pmatrix} + b_2 \begin{pmatrix} 1 \\ b_{22} \end{pmatrix}, \quad (3.3)$$

where a_{ij} and b_{ij} are pseudospin elements. This can be rewritten using matrices relating amplitudes inside and outside the barrier as

$$\begin{pmatrix} b_1 \\ b_2 \end{pmatrix} = B^{-1} A \begin{pmatrix} a_1 \\ a_2 \end{pmatrix}, \quad (3.4)$$

where

$$A = \begin{pmatrix} 1 & 1 \\ a_{12} & a_{22} \end{pmatrix}, \quad B = \begin{pmatrix} 1 & 1 \\ b_{12} & b_{22} \end{pmatrix} \quad (3.5)$$

The same logic can be applied to the second interface at position $x = l$:

$$b_1 \begin{pmatrix} 1 \\ b_{12} \end{pmatrix} + b_2 \begin{pmatrix} 1 \\ b_{22} \end{pmatrix} = c_1 \begin{pmatrix} 1 \\ c_{12} \end{pmatrix} + c_2 \begin{pmatrix} 1 \\ c_{22} \end{pmatrix}. \quad (3.6)$$

We assume the Fermi energy ϵ_F for $x < 0$ is the same as when $x > l$ (i.e., the junction is symmetric). As such, the pseudospinor amplitudes are still the same. Thus,

$$\begin{pmatrix} c_1 \\ c_2 \end{pmatrix} = A^{-1}B \begin{pmatrix} b_1 \\ b_2 \end{pmatrix}. \quad (3.7)$$

A matrix to describe the free flow of quasiparticles from the interface at $x = 0$ to the interface at $x = l$ can be written as

$$C = \begin{pmatrix} e^{ik'_x l} & 0 \\ 0 & e^{-ik'_x l} \end{pmatrix}, \quad (3.8)$$

where prime terms are used to denote quantities inside the barrier. Using this, we can fully describe transport across the two barriers which make up the n-p-n junction:

$$\begin{pmatrix} c_1 \\ c_2 \end{pmatrix} = A^{-1}BCB^{-1}A \begin{pmatrix} a_1 \\ a_2 \end{pmatrix}. \quad (3.9)$$

Here, $A^{-1}BCB^{-1}A$ is the transfer matrix. The next step is to determine its elements.

Calculation of Pseudospin Amplitudes

The matrices defined above contain pseudospin amplitudes only. To determine these we solve the Schrödinger equation $(H_1 - \epsilon)\psi = 0$ asymptotically far from the junction using an ansatz $\psi = a_1(1, a_{12})e^{ik_x x}$ for the incoming wavefunction, where

$$H_1 = -\hbar v(\sigma_x p_x + \sigma_y p_y) = \hbar v(i\sigma_x \partial_x - \sigma_y k_y). \quad (3.10)$$

We define $\epsilon = 0$ in the centre of the barrier, thus at $\epsilon + u/2$ while outside and $\epsilon - u/2$ inside, determining $-\hbar v k_x - \hbar v k_y i - (\epsilon + u/2) a_{12} = 0$, hence

Element	Momenta
$a_{12} = \frac{1}{\tilde{\epsilon} + \tilde{u}/2}(-\tilde{k}_x - i\tilde{k}_y)$	$\tilde{k}_x = \sqrt{-\tilde{k}_y^2 + \frac{1}{4}(\tilde{u} + 2\tilde{\epsilon})^2}$
$a_{22} = \frac{1}{\tilde{\epsilon} + \tilde{u}/2}(\tilde{k}_x - i\tilde{k}_y)$	$\tilde{k}'_x = -\sqrt{-\tilde{k}_y^2 + \frac{1}{4}(\tilde{u} - 2\tilde{\epsilon})^2}$
$b_{12} = \frac{1}{\tilde{\epsilon} - \tilde{u}/2}(-\tilde{k}'_x - i\tilde{k}_y)$	
$b_{22} = \frac{1}{\tilde{\epsilon} - \tilde{u}/2}(\tilde{k}'_x - i\tilde{k}_y)$	

Table 3.1: Pseudospin elements and momenta for the analysis of transmission through an n-p-n junction in monolayer graphene.

$$a_{12} = \frac{\hbar v}{\left(\epsilon + \frac{u}{2}\right)}(-k_x - k_y i), \quad (3.11)$$

where $k_x = \sqrt{-4\hbar^2 k_y^2 v^2 + (u + 2\epsilon)^2} / (2\hbar v)$. For convenience we switch to unitless parameters, defining

$$k_x = \frac{\tilde{k}_x}{l}, \quad k_y = \frac{\tilde{k}_y}{l}, \quad \epsilon = \tilde{\epsilon} u_0, \quad u = \tilde{u} u_0, \quad (3.12)$$

where $u_0 = \hbar v / l$. The other pseudospin elements and momenta values are found by the method described here and are presented in Table 3.1, using other parts of the wavefunctions in Eqn. 3.2. We define $k_y = k_F \sin \theta$ (where $k_F = \sqrt{k_x^2 + k_y^2}$ is the Fermi momentum and θ is defined in Fig. 2.3), so that $k_y = (1/2l)(\tilde{u} + 2\tilde{\epsilon}) \sin \theta$. Eqn. 3.9 can then be solved for the transmission $t = |c_1|^2$, which is plotted for angles in the range $\theta \in [-\pi/2, \pi/2]$ in Fig. 3.4(a). The Klein tunnelling effect produces perfect transmission when $\theta = 0$ as expected, but the transmission robustness at this angle, as well as others, is affected strongly by the interface height u .

3.1.2 Bilayer Graphene

The procedure for calculating the transfer matrix across an n-p-n junction in bilayer graphene is quite similar to that of the monolayer. However, given the quadratic differential operator in its low energy Hamiltonian, evanescent waves as well as plane waves are possible solutions of the Schrödinger equation.

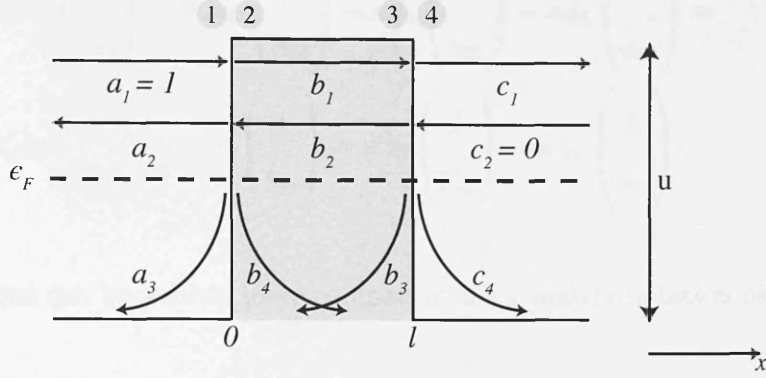


Fig. 3.3: Schematic of an n-p-n junction in bilayer graphene in one dimension, with interfaces at $x = 0$ and $x = l$. In addition to the plane waves as in Fig. 3.2, evanescent waves are also allowed. Regions 1–4 are also shown.

Functions representing plane and evanescent waves, and their derivatives, must match at the first interface ($x = 0$) in Fig. 3.3. If the wavefunctions ψ_i (for each region i in Fig. 3.3) are a linear combination of these, we have

$$\psi_1(x) = a_1 \begin{pmatrix} 1 \\ a_{12} \end{pmatrix} e^{ik_x x} + a_2 \begin{pmatrix} 1 \\ a_{22} \end{pmatrix} e^{-ik_x x} + a_3 \begin{pmatrix} 1 \\ a_{32} \end{pmatrix} e^{\kappa x} + a_4 \begin{pmatrix} 1 \\ a_{42} \end{pmatrix} e^{-\kappa x},$$

$$\psi_2(x) = b_1 \begin{pmatrix} 1 \\ b_{12} \end{pmatrix} e^{ik'_x x} + b_2 \begin{pmatrix} 1 \\ b_{22} \end{pmatrix} e^{-ik'_x x} + b_3 \begin{pmatrix} 1 \\ b_{32} \end{pmatrix} e^{\kappa' x} + b_4 \begin{pmatrix} 1 \\ b_{42} \end{pmatrix} e^{-\kappa' x}, \quad (3.13)$$

and thus their matching at $x = 0$ gives two equations:

$$a_1 \begin{pmatrix} 1 \\ a_{12} \end{pmatrix} + a_2 \begin{pmatrix} 1 \\ a_{22} \end{pmatrix} + a_3 \begin{pmatrix} 1 \\ a_{32} \end{pmatrix} + a_4 \begin{pmatrix} 1 \\ a_{42} \end{pmatrix} =$$

$$b_1 \begin{pmatrix} 1 \\ b_{12} \end{pmatrix} + b_2 \begin{pmatrix} 1 \\ b_{22} \end{pmatrix} + b_3 \begin{pmatrix} 1 \\ b_{32} \end{pmatrix} + b_4 \begin{pmatrix} 1 \\ b_{42} \end{pmatrix}, \quad (3.14)$$

$$\begin{aligned}
& ik_x a_1 \begin{pmatrix} 1 \\ a_{12} \end{pmatrix} - ik_x a_2 \begin{pmatrix} 1 \\ a_{22} \end{pmatrix} + \kappa a_3 \begin{pmatrix} 1 \\ a_{32} \end{pmatrix} - \kappa a_4 \begin{pmatrix} 1 \\ a_{42} \end{pmatrix} = \\
& ik'_x b_1 \begin{pmatrix} 1 \\ b_{12} \end{pmatrix} - ik'_x b_2 \begin{pmatrix} 1 \\ b_{22} \end{pmatrix} + \kappa' b_3 \begin{pmatrix} 1 \\ b_{32} \end{pmatrix} - \kappa' b_4 \begin{pmatrix} 1 \\ b_{42} \end{pmatrix}. \quad (3.15)
\end{aligned}$$

These equations can be written more compactly using matrix notation as

$$\underbrace{\begin{pmatrix} 1 & 1 & 1 & 1 \\ a_{12} & a_{22} & a_{32} & a_{42} \\ ik_x & -ik_x & \kappa & -\kappa \\ ik_x a_{12} & -ik_x a_{22} & \kappa a_{32} & -\kappa a_{42} \end{pmatrix}}_A \begin{pmatrix} a_1 \\ a_2 \\ a_3 \\ a_4 \end{pmatrix} = \underbrace{\begin{pmatrix} 1 & 1 & 1 & 1 \\ b_{12} & b_{22} & b_{32} & b_{42} \\ ik'_x & -ik'_x & \kappa' & -\kappa' \\ ik'_x b_{12} & -ik'_x b_{22} & \kappa' b_{32} & -\kappa' b_{42} \end{pmatrix}}_B \begin{pmatrix} b_1 \\ b_2 \\ b_3 \\ b_4 \end{pmatrix}, \quad (3.16)$$

or

$$\begin{pmatrix} b_1 \\ b_2 \\ b_3 \\ b_4 \end{pmatrix} = B^{-1} A \begin{pmatrix} a_1 \\ a_2 \\ a_3 \\ a_4 \end{pmatrix}. \quad (3.17)$$

The wavefunctions at the next barrier (at $x = l$) can similarly be calculated, assuming a symmetric junction so that pseudospin elements are equal for $x < 0$ and $x > l$. The wavefunctions are

$$\psi_3(x) = \psi_2(x - l), \quad (3.18)$$

$$\psi_4(x) = \psi_1(x - l), \quad (3.19)$$

so that matching them and their derivatives at the interface (at $x = l$) gives

$$\begin{aligned}
& c_1 \begin{pmatrix} 1 \\ a_{12} \end{pmatrix} + c_2 \begin{pmatrix} 1 \\ a_{22} \end{pmatrix} + c_3 \begin{pmatrix} 1 \\ a_{32} \end{pmatrix} + c_4 \begin{pmatrix} 1 \\ a_{42} \end{pmatrix} = \\
& b_1 \begin{pmatrix} 1 \\ b_{12} \end{pmatrix} + b_2 \begin{pmatrix} 1 \\ b_{22} \end{pmatrix} + b_3 \begin{pmatrix} 1 \\ b_{32} \end{pmatrix} + b_4 \begin{pmatrix} 1 \\ b_{42} \end{pmatrix}, \tag{3.20}
\end{aligned}$$

$$\begin{aligned}
& ik_x c_1 \begin{pmatrix} 1 \\ a_{12} \end{pmatrix} - ik_x c_2 \begin{pmatrix} 1 \\ a_{22} \end{pmatrix} + \kappa c_3 \begin{pmatrix} 1 \\ a_{32} \end{pmatrix} - \kappa c_4 \begin{pmatrix} 1 \\ a_{42} \end{pmatrix} = \\
& ik'_x b_1 \begin{pmatrix} 1 \\ b_{12} \end{pmatrix} - ik'_x b_2 \begin{pmatrix} 1 \\ b_{22} \end{pmatrix} + \kappa' b_3 \begin{pmatrix} 1 \\ b_{32} \end{pmatrix} - \kappa' b_4 \begin{pmatrix} 1 \\ b_{42} \end{pmatrix}. \tag{3.21}
\end{aligned}$$

Using matrices A and B ,

$$\begin{pmatrix} b_1 \\ b_2 \\ b_3 \\ b_4 \end{pmatrix} = B^{-1} A \begin{pmatrix} c_1 \\ c_2 \\ c_3 \\ c_4 \end{pmatrix}. \tag{3.22}$$

A matrix describing the propagation of carriers from the first interface to the second is given by

$$C = \begin{pmatrix} e^{ik'_x l} & 0 & 0 & 0 \\ 0 & e^{-ik'_x l} & 0 & 0 \\ 0 & 0 & e^{\kappa' l} & 0 \\ 0 & 0 & 0 & e^{-\kappa' l} \end{pmatrix}. \tag{3.23}$$

Thus,

$$\begin{pmatrix} c_1 \\ c_2 \\ c_3 \\ c_4 \end{pmatrix} = A^{-1} B C B^{-1} A \begin{pmatrix} a_1 \\ a_2 \\ a_3 \\ a_4 \end{pmatrix}. \tag{3.24}$$

Analysing transport directed in the positive x direction through the junction, Eqn. 3.24 can now be solved for the transmission $t = |c_1|^2$ (the outgoing plane wave amplitude), after defining $a_1 = 1$, $a_4 = c_2 = c_3 = 0^*$.

Calculation of Pseudospin Amplitudes

In order to calculate t , we must calculate the elements of the matrices A , B , and C . As in the monolayer case, this is done by solving the relevant Schrödinger equation for the constituent parts of the specified wavefunctions ψ_i , asymptotically far from the junction. The low energy effective Hamiltonian for bilayer graphene is given by the first term in Eqn. 2.24,

$$H_2 = -\frac{1}{2m} \begin{pmatrix} 0 & (\pi^\dagger)^2 \\ \pi^2 & 0 \end{pmatrix}, \quad (3.25)$$

where $\pi = p_x + ip_y$, $p_x = i\hbar\partial_x$, and $p_y = \hbar k_y$, such that

$$H_2 = -\frac{\hbar^2}{2m} [\sigma_x(-k_y^2 - \partial_x^2) + 2i\sigma_y k_y \partial_x]. \quad (3.26)$$

Solving Schrödinger's equation $H_2\psi = \epsilon\psi$ by substituting $\psi = (1, a_{12})e^{ik_x x}$ (and then the other parts of Eqns. 3.1.2 and 3.1.3), we find the elements of the pseudospinors, presented in Table 3.3, where for simplicity we switch to unitless parameters defined in Table 3.2.

Transmission is plotted using $k_y = \sqrt{\tilde{u}/2 + \tilde{\epsilon}} \sin\theta$ in Fig. 3.4(b). Klein tunnelling again gives rise to perfect transmission at certain angles, though the effect is not as robust as in the monolayer case. The transmission is still sensitive to barrier height u .

*That is, there is no exponentially increasing wave from the left or right of the junction, and we neglect incident plane waves from the right.

Unitless Parameters	
$\epsilon = \tilde{\epsilon}u_0$	$u_0 = \frac{\hbar^2}{2ml^2}$
$u = \tilde{u}u_0$	
$k_y = \tilde{k}_y/l$	
$k_x = \tilde{k}_x/l$	
$k'_x = \tilde{k}'_x/l$	

Table 3.2: Unitless parameters in bilayer graphene.

Element	Momenta
$a_{12} = \frac{1}{\tilde{\epsilon} + \tilde{u}/2} \left(\tilde{k}_y^2 - \tilde{k}_x^2 - 2i\tilde{k}_x\tilde{k}_y \right)$	$\tilde{k}_x = \sqrt{-\tilde{k}_y^2 + (\tilde{u}/2 + \tilde{\epsilon})}$
$a_{22} = \frac{1}{\tilde{\epsilon} + \tilde{u}/2} \left(\tilde{k}_y^2 - \tilde{k}_x^2 + 2i\tilde{k}_x\tilde{k}_y \right)$	$\tilde{k}'_x = -\sqrt{-\tilde{k}_y^2 + (\tilde{u}/2 - \tilde{\epsilon})}$
$a_{32} = \frac{1}{\tilde{\epsilon} + \tilde{u}/2} \left(\tilde{k}_y^2 + \tilde{\kappa}^2 - 2\tilde{\kappa}\tilde{k}_y \right)$	$\tilde{\kappa} = \sqrt{\tilde{k}_y^2 + (\tilde{u}/2 + \tilde{\epsilon})}$
$a_{42} = \frac{1}{\tilde{\epsilon} + \tilde{u}/2} \left(\tilde{k}_y^2 + \tilde{\kappa}^2 + 2\tilde{\kappa}\tilde{k}_y \right)$	$\tilde{\kappa}' = -\sqrt{\tilde{k}_y^2 + (\tilde{u}/2 - \tilde{\epsilon})}$
$b_{12} = \frac{1}{\tilde{\epsilon} - \tilde{u}/2} \left(\tilde{k}_y^2 - \tilde{k}'_x{}^2 - 2i\tilde{k}'_x\tilde{k}_y \right)$	
$b_{22} = \frac{1}{\tilde{\epsilon} - \tilde{u}/2} \left(\tilde{k}_y^2 - \tilde{k}'_x{}^2 + 2i\tilde{k}'_x\tilde{k}_y \right)$	
$b_{32} = \frac{1}{\tilde{\epsilon} - \tilde{u}/2} \left(\tilde{k}_y^2 + \tilde{\kappa}'^2 - 2\tilde{\kappa}'\tilde{k}_y \right)$	
$b_{42} = \frac{1}{\tilde{\epsilon} - \tilde{u}/2} \left(\tilde{k}_y^2 + \tilde{\kappa}'^2 + 2\tilde{\kappa}'\tilde{k}_y \right)$	

Table 3.3: Pseudospin elements and momenta for the analysis of transmission through an n-p-n junction in bilayer graphene.

3.2 Periodic Modulation of the Potential Profile in Monolayer Graphene

We now extend the analysis of an n-p-n junction in monolayer graphene to that of an infinite array of junctions, as shown in Fig. 3.1. Each step has a width αl , while each well has a width $(1 - \alpha)l$. A transfer matrix can be derived to equate a quasiparticle travelling from region one to region five (that is, across total length l ; see Fig. 3.1), $\psi_5 = T\psi_1$. As a general solution to the Schrödinger equation, the wavefunction must also be able to acquire a Bloch phase ϕ when propagating this

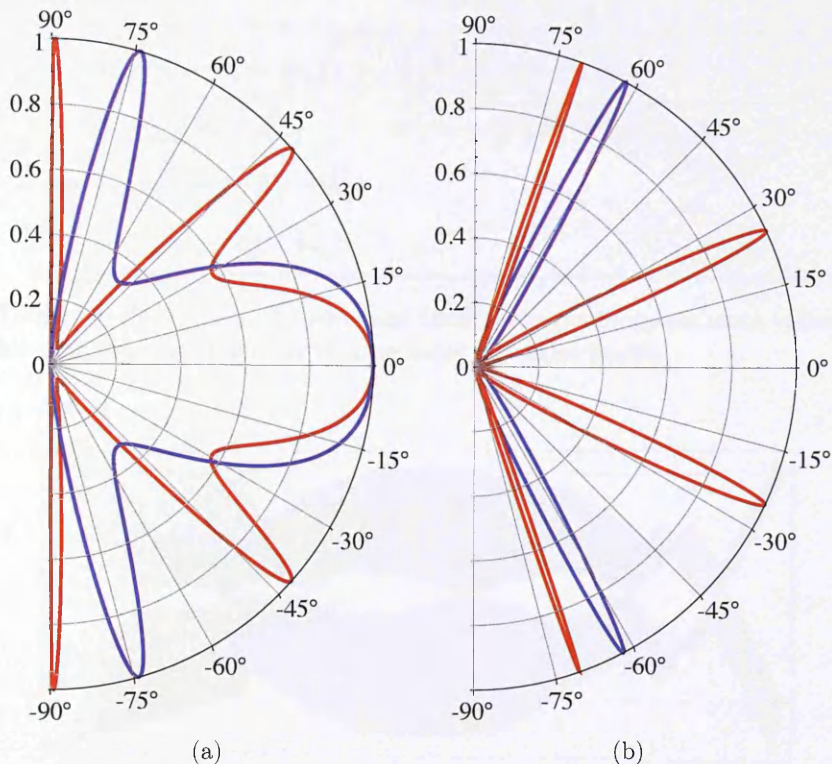


Fig. 3.4: Angular dependence of transmission through an n-p-n junction in (a) monolayer and (b) bilayer graphene. (a) Transmission plotted with $\epsilon = 83$ meV, $l = 100$ nm, and $u = 200$ meV (285 meV) for the red (blue) curves. (b) Transmission plotted with $\epsilon = 17$ meV, $l = 100$ nm, and $u = 50$ meV (100 meV) for the red (blue) curves. The values chosen are used to match Katsnelson et al. [9, Fig. 2].

distance, such that $\psi_5 = e^{i\phi}\psi_1$. These two quantities can be equated so that we may solve the equation

$$|T - \mathbb{I}_2 e^{i\phi}| = 0, \quad (3.27)$$

where \mathbb{I}_2 is the 2x2 unit matrix and $T = DA^{-1}BCB^{-1}A$. Matrices A, B, C , and D are derived in the same manner as in Section 3.1.1 and are defined as

$$A = \begin{pmatrix} 1 & 1 \\ a_{12} & a_{22} \end{pmatrix}, \quad B = \begin{pmatrix} 1 & 1 \\ b_{12} & b_{22} \end{pmatrix},$$

Element	Momenta
$a_{12} = \frac{1}{\tilde{\epsilon} + \tilde{u}\alpha} (-\tilde{k}_x - i\tilde{k}_y)$	$\tilde{k}_x = \sqrt{-\tilde{k}_y^2 + (\tilde{u}\alpha + \tilde{\epsilon})^2}$
$a_{22} = \frac{1}{\tilde{\epsilon} + \tilde{u}\alpha} (\tilde{k}_x - i\tilde{k}_y)$	$\tilde{k}'_x = -\sqrt{-\tilde{k}_y^2 + (\tilde{u}(1-\alpha) - \tilde{\epsilon})^2}$
$b_{12} = \frac{1}{\tilde{\epsilon} - \tilde{u}(1-\alpha)} (-\tilde{k}'_x - i\tilde{k}_y)$	
$b_{22} = \frac{1}{\tilde{\epsilon} - \tilde{u}(1-\alpha)} (\tilde{k}'_x - i\tilde{k}_y)$	

Table 3.4: Pseudospin elements and their corresponding momenta values for monolayer graphene with a periodic potential profile.

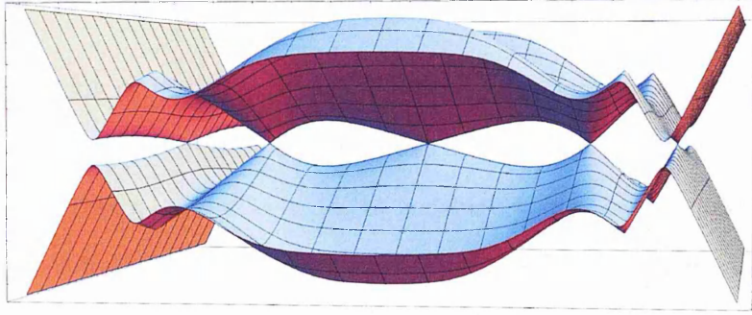


Fig. 3.5: First conduction and valence energy surfaces for periodically-modulated monolayer graphene. Plotted using the parameters $\alpha = 1/2$ and $u = 10\pi$.

$$C = \begin{pmatrix} e^{ik'_x \alpha l} & 0 \\ 0 & e^{-ik'_x \alpha l} \end{pmatrix}, \quad D = \begin{pmatrix} e^{ik_x(1-\alpha)l} & 0 \\ 0 & e^{-ik_x(1-\alpha)l} \end{pmatrix}. \quad (3.28)$$

The matrix D is introduced to describe the propagation from region four to five, which was not considered in the simpler n-p-n case. The unitless parameters that constitute these matrices are defined in Table 3.4.

Eqn. 3.27 is analytically calculated to be

$$\begin{aligned} & \cos(\phi) - \cos(\alpha\tilde{k}'_x) \cos((\alpha-1)\tilde{k}_x) \\ & + \frac{(\tilde{k}_y^2 - (\tilde{u}(\alpha-1) + \tilde{\epsilon})(\tilde{u}\alpha + \tilde{\epsilon}))}{\tilde{k}_x \tilde{k}'_x} \sin((\alpha-1)\tilde{k}_x) \sin(\alpha\tilde{k}'_x) = 0. \end{aligned} \quad (3.29)$$

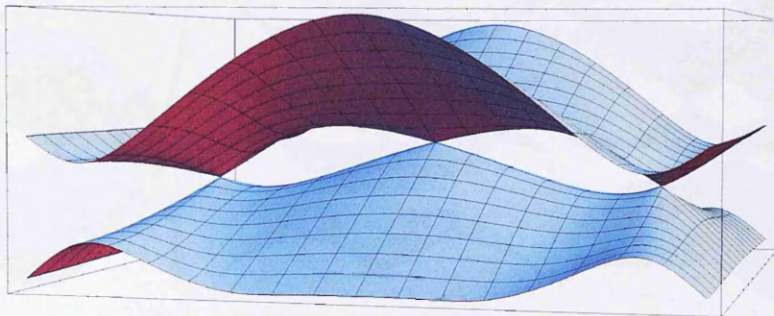


Fig. 3.6: First conduction and valence energy surfaces for periodically-modulated monolayer graphene. Plotted using the parameters $\alpha = 6/10$ and $u = 6\pi$.

This is plotted for $\alpha = 1/2$ in Fig. 3.5 using the source code presented in Appendix A. Given specific arguments for α and \tilde{u} , the algorithm solves Eqn. 3.29 for ϵ by iterating across k_y and ϕ in order to generate energy surface plots. A root of Eqn. 3.29 for the lower bounds chosen for k_y and ϕ is obtained phenomenologically, and then the Brent or Newton-Raphson methods of root finding are used to find the next root after k_y or α is incremented by a small quantity. As shown in Fig. 3.5, along $\phi = 0 \pm 2\pi n$, where $n \in \mathbb{N}_0$, extra Dirac points develop. To understand the effects that the parameters \tilde{u} and α have on the energy surfaces (and where the induced Dirac points form), other values of these parameters were used. Fig. 3.6 shows how the Dirac points at $k_y \neq 0$ form at a negative energy when the width of a barrier is longer than a well (referring to Fig. 3.1). Additional energy surfaces are shown in Figs. 3.7(a)–(c), where Dirac points can be seen at higher energies.

3.2.1 Analysis of the Long Wavelength Approximation

Eqn. 3.29 can be simplified dramatically if it can be assumed that $v/l \gg u$, i.e., that $1 \gg \tilde{u}$. (Thus, $\epsilon > u$, such that scattering effects can be neglected.) If we Taylor expand this equation around $u = 0$, we derive

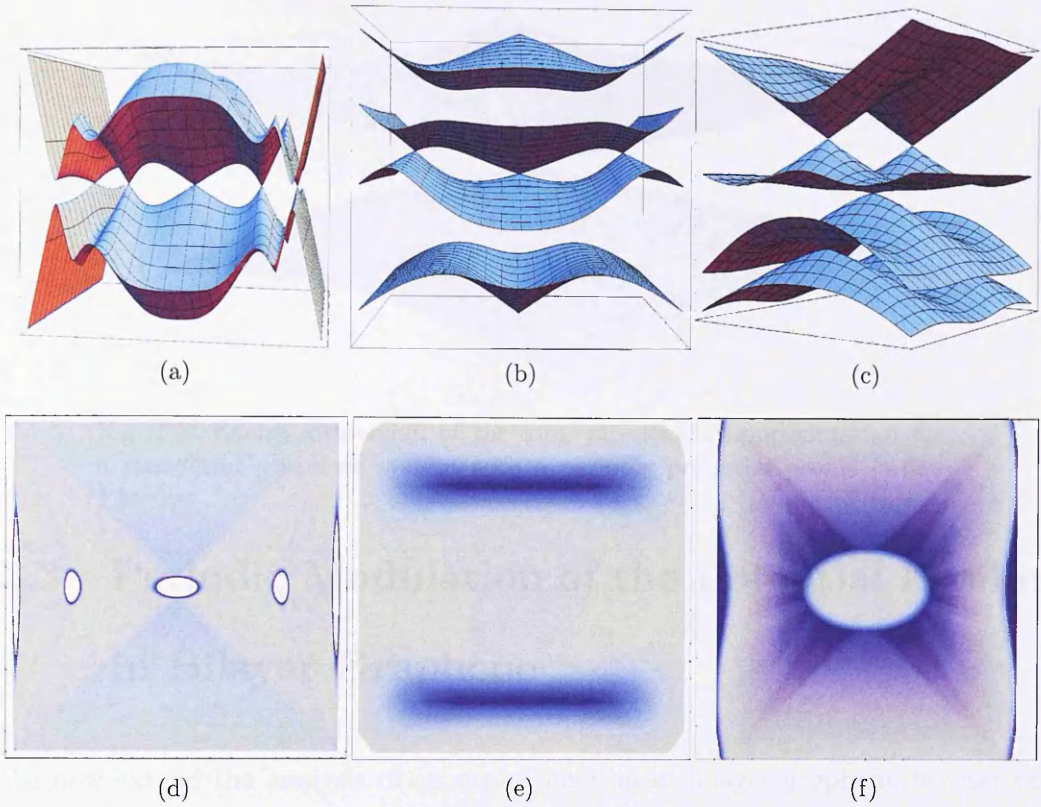


Fig. 3.7: (a)–(c) Energy dispersion surfaces with energy ϵ plotted against the phase ϕ and perpendicular direction of momentum k_y for a Kronig-Penney system in monolayer graphene. (d)–(f) show the corresponding energy cuts through these surfaces (that is, (d) corresponds to (a), etc.). The energy that the cut is made at is determined by the energy of the caustics formed in the system; see Section 3.4. Parameters used to plot Eqn. 3.29 are (a) $\alpha = 1/2$, $u = 10\pi$, (b) $\alpha = 4/10$, $u = 6\pi$, (c) $\alpha = 8/10$, $u = 5\pi$. The values of δ used to produce (d)–(f) are 0.1, 0.7, and 0.2, respectively. The values of ϵ_{cut} used to produce (d)–(f) are 0, 3.7, and -9.4, respectively.

$$\cos(\phi) = \frac{\Gamma \cos(\eta) - k_y^2 u^2 (\cos(\eta - 2\eta\alpha) + 2\eta(\alpha - 1)\alpha \sin(\eta))}{4(k_y^2 - \epsilon^2)^2},$$

$$\Gamma = (4k_y^4 + 4\epsilon^4 + k_y^2(u^2 - 8\epsilon^2)),$$

$$\eta = \sqrt{\epsilon^2 - k_y^2}. \quad (3.30)$$

Simplifying, we find that the energy dispersion relation is $\epsilon = \pm\sqrt{k_y^2 + \phi^2}$, thus restoring the single Dirac cone, shown in Fig. 3.8.

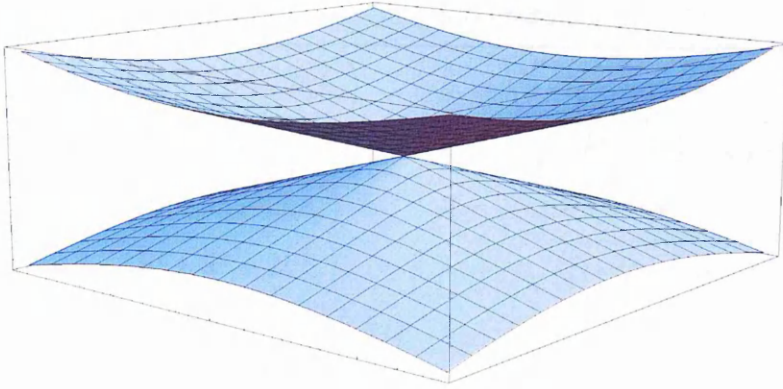


Fig. 3.8: Energy dispersion of the long wavelength approximation for a monolayer graphene system with a periodic potential profile (when $1 \gg \bar{u}$).

3.3 Periodic Modulation of the Potential Profile in Bilayer Graphene

We now extend the analysis of an n-p-n junction in bilayer graphene to that of an infinite array of junctions, as shown in Fig. 3.1. Each step has a width αl , while each well has a width $(1 - \alpha)l$. A transfer matrix can be derived to equate a quasiparticle travelling from region one to region five (that is, across a total length l ; see Fig. 3.1), $\psi_5 = T\psi_1$. As a general solution to the Schrödinger equation, the wavefunction must also be able to acquire a Bloch phase ϕ when propagating this distance, such that $\psi_5 = e^{i\phi}\psi_1$. These two quantities can be equated so that we may solve the equation

$$|T - \mathbb{I}_4 e^{i\phi}| = 0, \tag{3.31}$$

where \mathbb{I}_4 is the 4x4 unit matrix and $T = DA^{-1}BCB^{-1}A$. Matrices A, B, C , and D are derived in the same manner as in Section 3.1.2 and are defined as

$$A = \begin{pmatrix} 1 & 1 & 1 & 1 \\ a_{12} & 1_{22} & a_{32} & a_{42} \\ ik_x & -ik_x & \kappa & -\kappa \\ ik_x a_{12} & -ik_x a_{22} & \kappa a_{32} & -\kappa a_{42} \end{pmatrix}, \quad B = \begin{pmatrix} 1 & 1 & 1 & 1 \\ b_{12} & 1_{22} & b_{32} & b_{42} \\ ik'_x & -ik'_x & \kappa' & -\kappa' \\ ik'_x b_{12} & -ik'_x b_{22} & \kappa' b_{32} & -\kappa' b_{42} \end{pmatrix},$$

3.3 Periodic Modulation of the Potential Profile in Bilayer Graphene 54

Element	Momenta
$a_{12} = \frac{1}{\tilde{\epsilon} + \tilde{u}\alpha} \left(\tilde{k}_y^2 - \tilde{k}_x^2 - 2i\tilde{k}_x\tilde{k}_y \right)$	$\tilde{k}_x = \sqrt{-\tilde{k}_y^2 + \tilde{u}\alpha + \tilde{\epsilon}}$
$a_{22} = \frac{1}{\tilde{\epsilon} + \tilde{u}\alpha} \left(\tilde{k}_y^2 - \tilde{k}_x^2 + 2i\tilde{k}_x\tilde{k}_y \right)$	$\tilde{k}_x' = -\sqrt{-\tilde{k}_y^2 + \tilde{u}(1-\alpha) - \tilde{\epsilon}}$
$a_{32} = \frac{1}{\tilde{\epsilon} + \tilde{u}\alpha} \left(\tilde{k}_y^2 + \tilde{\kappa}^2 - 2\tilde{\kappa}\tilde{k}_y \right)$	$\tilde{\kappa} = \sqrt{\tilde{k}_y^2 + \tilde{u}\alpha + \tilde{\epsilon}}$
$a_{42} = \frac{1}{\tilde{\epsilon} + \tilde{u}\alpha} \left(\tilde{k}_y^2 + \tilde{\kappa}^2 + 2\tilde{\kappa}\tilde{k}_y \right)$	$\tilde{\kappa}' = -\sqrt{\tilde{k}_y^2 + \tilde{u}(1-\alpha) - \tilde{\epsilon}}$
$b_{12} = \frac{1}{\tilde{\epsilon} - \tilde{u}(1-\alpha)} \left(\tilde{k}_y^2 - \tilde{k}_x'^2 - 2i\tilde{k}_x'\tilde{k}_y \right)$	
$b_{22} = \frac{1}{\tilde{\epsilon} - \tilde{u}(1-\alpha)} \left(\tilde{k}_y^2 - \tilde{k}_x'^2 + 2i\tilde{k}_x'\tilde{k}_y \right)$	
$b_{32} = \frac{1}{\tilde{\epsilon} - \tilde{u}(1-\alpha)} \left(\tilde{k}_y^2 + \tilde{\kappa}'^2 - 2\tilde{\kappa}'\tilde{k}_y \right)$	
$b_{42} = \frac{1}{\tilde{\epsilon} - \tilde{u}(1-\alpha)} \left(\tilde{k}_y^2 + \tilde{\kappa}'^2 + 2\tilde{\kappa}'\tilde{k}_y \right)$	

Table 3.5: Pseudospin elements and momenta for the analysis of a periodic potential profile in bilayer graphene. Parameters with tildes are unitless, given in Table 3.2.

$$C = \begin{pmatrix} e^{ik'_x\alpha l} & 0 & 0 & 0 \\ 0 & e^{-ik'_x\alpha l} & 0 & 0 \\ 0 & 0 & e^{\kappa'\alpha l} & 0 \\ 0 & 0 & 0 & e^{-\kappa'\alpha l} \end{pmatrix}, \quad D = \begin{pmatrix} e^{ik_x(1-\alpha)l} & 0 & 0 & 0 \\ 0 & e^{-ik_x(1-\alpha)l} & 0 & 0 \\ 0 & 0 & e^{\kappa(1-\alpha)l} & 0 \\ 0 & 0 & 0 & e^{-\kappa(1-\alpha)l} \end{pmatrix}. \quad (3.32)$$

Wavefunctions of the form in Eqn. 3.13 are admitted as solutions to the Hamiltonian (Eqn. 3.25), in the same manner as in Section 3.1.2. Substituting plane and evanescent waves enables us to determine values for the pseudospin components and the momenta, presented in Table 3.5

As with the analysis of a periodic modulation of the potential in monolayer graphene, given specific arguments for α and \tilde{u} , we numerically solve Eqn. 3.31 for ϵ^\dagger . We iterate across k_y and ϕ in order to generate energy surface plots; a root of the equation for the lower bounds chosen for k_y and ϕ is obtained phenomenologically, and then the Brent or Newton-Raphson methods of root finding are used to find the next root after k_y or α is incremented by a small quantity. The energy

[†]Using the algorithm defined in Appendix A.

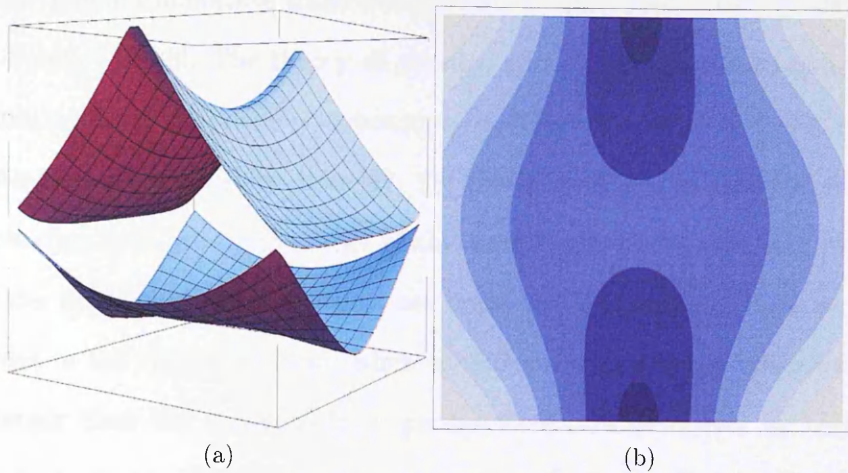


Fig. 3.9: (a) First two conduction bands of the spectrum of a superlattice with square barriers in bilayer graphene; $\tilde{u} = 37.02$ (corresponding to $u = 100$ meV and $l = 20$ nm), $\alpha = 1/2$. (b) Contour plot of the first conduction band of the spectrum in (a).

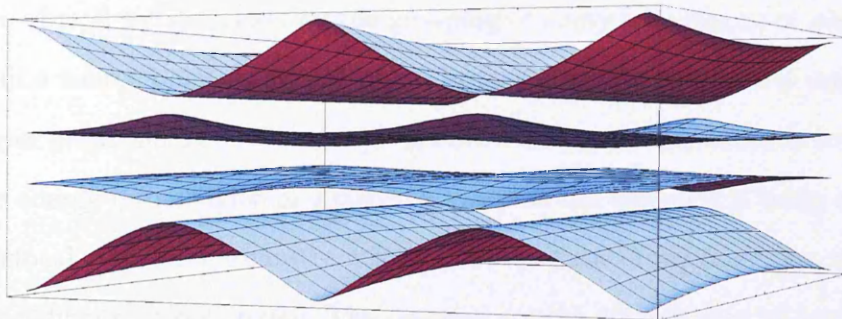


Fig. 3.10: First two conduction and valence bands for an even periodic potential profile in bilayer graphene (that is, $\alpha = 1/2$). The height of the barrier is $u = 100$ meV.

surfaces for the first conduction and valence bands are shown in Fig. 3.9(a). We find that the surfaces approach each other at four points but never actually touch. This is shown in Fig. 3.10, including the valence bands.

3.4 The Formation of Cusps at n-p Junction Interfaces

In this Section we overview the formation of caustics and cusps in monolayer graphene, and analyse them in a system with a periodically-modulated external

potential. The mathematical framework behind singularities in ray optics is catastrophe theory [84–86]. The theory of caustics and its application to quasiparticle paths in monolayer graphene was developed by Cheianov et al. [63], describing an n-p-n junction as a Veselago lens [87, 88] (see Fig. 3.11). In theories where the distances discussed are on the order of the wavelength of the rays, the phase and amplitude, describing wavefunctions, are important parameters. Here we characterise rays in the shortwave limit, where singularities that are perceived on scales much larger than the wavelength of quasiparticles are described by trajectories along which energy flows, rather than wavefunctions. On finer scales the caustics become decorated with diffraction catastrophes, which are not discussed here. Hence, there is an analogy to geometric optics.

Families of rays are described by the grouping of many trajectories of quasiparticles from a source point to a focal point, propagating through an n-p junction in monolayer graphene. A family of rays has the ability to focus, which is to concentrate its energy into a region of dimension less than the system it is being analysed in. This focal region is the caustic, which is the envelope of ray functions, the locus where neighbouring rays touch. The caustics are the singularities of catastrophe theory, and dominate spaces of many trajectories since they are the places that appear brightest. In relation to Veselago lenses in monolayer graphene, caustics occur around the focal point when the lens' refractive index is not $n = -1$. Perfect focusing would be seen if $n = -1$, for zero temperature (such that carriers are not excited to energies above the Fermi energy). If this condition is not met, a blurring of the focus will be seen [63], even for a lens with $k_c = k_v$ (where k_v (k_c) is the Fermi momentum in the valence (conduction) band[†]; a symmetric junction). Any small difference in the Fermi momenta in the n and p regions produces caustics, and when trajectories with angle θ and $-\theta$ are considered, the point at which the

[†]Such that $k_c = \sqrt{k_x^2 + k_y^2}$ and $k_v = \sqrt{k_x'^2 + k_y'^2}$, given our notation of primes denoting momentum inside a p region. The ratio of Fermi momenta plays the role of the refractive index in geometrical optics.

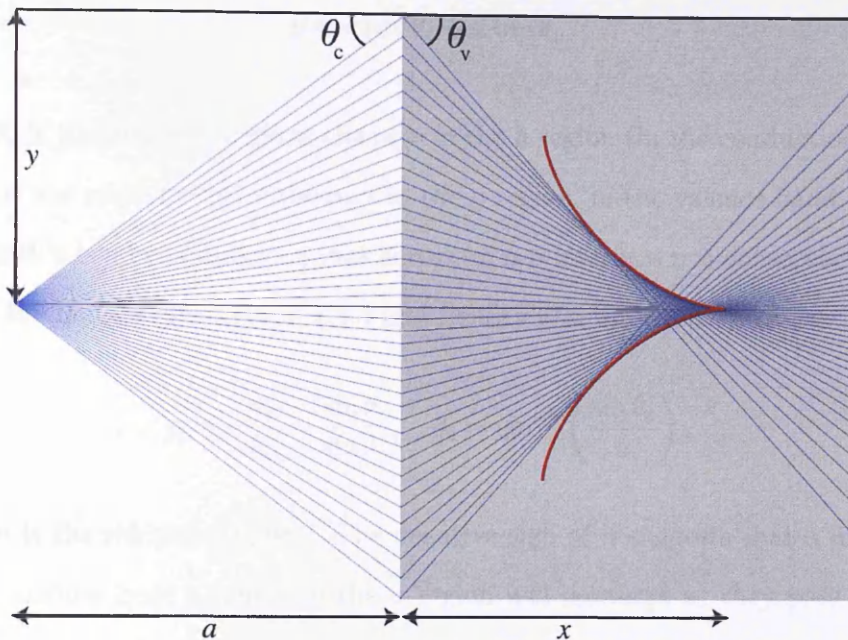


Fig. 3.11: Caustics in an n-p junction (where the p region is coloured gray). Incident waves approach the junction at an angle θ_c (in the conduction band), and refract at an angle θ_v (in the valence band). The envelope of caustics is highlighted in red, showing their meeting as a cusp. Plotted using refractive index $n = -0.82$.

caustics meet is called a cusp[§]. It is of interest therefore to find the position at which the cusp is formed, and the energies at which they occur. If we analyse these ray trajectories in a system with a periodic potential profile, we are interested in the regime where the cusp forms at a particular position after propagating through several interfaces.

To characterise the caustics we must first define the ray trajectories, determined by Fermat's principle (i.e., rays in a homogeneous medium are straight, such that the optical distance it traverses is stable under local variations) [90]. The possible trajectories, given by y in Eqn. 3.35, are therefore parametrised by θ_c only; see Fig. 2.3. As such, the equation for the trajectory of rays at the interface of an n-p junction (Fig. 3.11) is given by

[§]A cusp is defined as an elementary catastrophe such that $\partial_{\theta_c} y$ in Eqn. 3.36 can be defined using two control parameters (constants), i.e., that it has a codimension of 2. Higher order polynomials exist in catastrophe theory too, such as the swallowtail, with a codimension of 3. See Berry [89, pp. 489].

$$y = a \tan \theta_c + x \tan \theta_v, \quad (3.33)$$

where θ_c is the incident angle of the rays in the n region (in the conduction band), and θ_v is the angle made by the rays in the p region, in the valence band. We can write Snell's law by considering that across an n-p interface \mathbf{v} is conserved but the sign of k_x changes (see Section 1.4.3 and Pendry and Smith [91]), so that

$$n = -\frac{k_v}{k_c} = \frac{\sin \theta_c}{\sin \theta_v}, \quad \theta_v = \sin^{-1} \left(\frac{\sin \theta_c}{n} \right), \quad (3.34)$$

where n is the refractive index[¶]. The negative sign of n suggests that a divergent flow of carriers from a source in the n region will converge as they pass the n-p interface. In the following derivation, we wish to determine x_{cusp} — the position where the cusp forms relative to the interface. To do this, firstly we can rewrite y in terms of θ_c alone:

$$\begin{aligned} y &= a \tan \theta_c + x \tan \theta_v \\ &= a \tan \theta_c + x \tan \left(\sin^{-1} \left(\frac{\sin \theta_c}{n} \right) \right) \\ &= a \tan \theta_c \pm \frac{x \sin \theta_c}{n \sqrt{1 - \frac{\sin^2 \theta_c}{n^2}}}. \end{aligned} \quad (3.35)$$

For the condition of stationarity enforced by Fermat's principle, we require

$\partial y / \partial \theta_c = 0$, producing

$$\frac{\partial y}{\partial \theta_c} = a \sec^2 \theta_c \mp \frac{n^3 x \cos \theta_c \sqrt{1 - \frac{\sin^2 \theta_c}{n^2}}}{(n^2 - \sin^2 \theta_c)^2} = 0, \quad (3.36)$$

which can be rearranged for x to give

$$x = \frac{a \sec^3 \theta_c (n^2 - \sin^2 \theta_c)^2}{n^3 \sqrt{1 - \frac{\sin^2 \theta_c}{n^2}}}. \quad (3.37)$$

[¶]The origin of the negative refractive index is due to the sign of k_v , since $\epsilon_F = v k_F$. In the valence band (with negative energy) the Fermi momentum is negative (for the reasons outlined in Section 1.4.3).

The form of x_{cusp} is the result of Taylor expanding Eqn. 3.37 around $\theta_c = 0$, since this is the angle at which the major contribution to the trajectories occurs. The expansion shows that $x_{\text{cusp}} = ak_v/k_c = a|n|$.

Additionally y_{caust} — the equation describing the shape of the caustics — can be derived. To do this, Eqn. 3.37 is substituted into Eqn. 3.35 to give

$$y = -\frac{a}{n^2}(n^2 - 1) \tan^3 \theta_c. \quad (3.38)$$

By rearranging Eqn. 3.37 for θ_c and substituting into Eqn. 3.38, the final result is

$$\begin{aligned} y_{\text{caust}} &= \pm \frac{a(n^2 - 1)}{n^2} \left[\frac{\left(a^4 n^4 (n^2 - 1)^6 x^2 \right)^{1/3}}{a^2 (n^2 - 1)^3} - \frac{n^2}{n^2 - 1} \right]^{3/2} \\ &= \pm \frac{a(n^2 - 1)}{n^2} \left[\frac{\left(x_{\text{cusp}}^4 x^2 \right)^{1/3}}{a^2 (n^2 - 1)} - \frac{n^2}{n^2 - 1} \right]^{3/2} \\ &= \pm \frac{a(n^2 - 1)}{n^2} \cdot \frac{1}{(n^2 - 1)^{3/2}} \cdot \left[\frac{\left(x_{\text{cusp}}^4 x^2 \right)^{1/3}}{a^2} - n^2 \right]^{3/2} \\ &= \frac{a}{n^2} \frac{1}{(n^2 - 1)^{1/2}} \left[\frac{x_{\text{cusp}}^{4/3} x^{2/3}}{a^2} - n^2 \right]^{3/2} \\ &= \pm \sqrt{\frac{\left(x^{2/3} - x_{\text{cusp}}^{2/3} \right)^3}{n^2 - 1}}. \end{aligned} \quad (3.39)$$

This is plotted as the red envelope in Fig. 3.11. We can now extend this derivation to multiple junctions.

3.4.1 Matching the Periodicity of the Formation of Cusps to the Period of the Superlattice

In this Section we analyse the effects of various trajectories of rays, forming cusps at regular interfaces, on the energy spectrum analysed in the problem of a periodic modulation of the potential profile in Section 3.2. The aim of the exercise is to de-

termine whether features seen in the spectrum (Figs. 3.7(a)–(c)) can be attributed to effects caused by these classical trajectories described by catastrophe theory. We start this analysis by extending the trajectory path that rays follow, to match Fig. 3.12 (i.e., an n-p-n junction). We then extend the analysis to prescribe cusps forming at interfaces with a periodicity matching that of the superlattice shown in Fig. 3.1, order to make the appropriate analogy. In the above analysis of an n-p junction, $x_{\text{cusp}} = a|n| = (1 - \alpha)l|n|$ if the trajectories start from the interface at $x = -(1 - \alpha)l$ for the system shown in Fig. 3.1. Given the footnote on page 56, it is determined that

$$n = 1 - \frac{u}{u\alpha + \epsilon}, \quad (3.40)$$

using values for k_x and k'_x from Table 3.4. In this Section we advance to describe trajectories in an n-p-n junction as in Fig. 3.12, so that

$$y = (1 - \alpha)l \tan \theta_c + \alpha l \tan \theta_v + (x - \alpha l) \tan \theta_c, \quad (3.41)$$

assuming the source point is at $x = -(1 - \alpha)l$. Following the same procedure as above, we calculate the position of the cusp to be

$$x_{\text{cusp}} = l \left(\left(2 - \frac{1}{n} \right) \alpha - 1 \right). \quad (3.42)$$

If we define $x_{\text{cusp}} = \alpha l$ so that the cusp forms at the second interface, then the refractive index is calculated to be $n = \alpha/(\alpha - 1)$. Equating this to Eqn. 3.40, the energy for the formation of the cusp is

$$\epsilon = u(1 - 2\alpha). \quad (3.43)$$

As confirmation, this can be arrived at in the same manner by considering the simpler trajectories of Eqn. 3.35. If we instead require the cusp to form at $x_{\text{cusp}} = l$, we find that

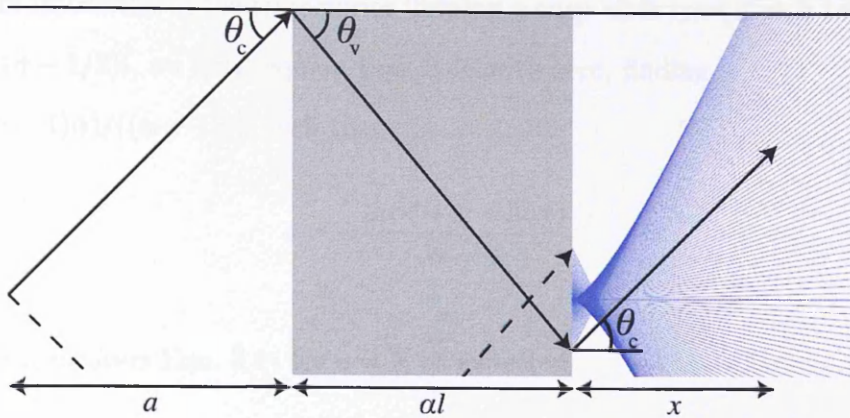


Fig. 3.12: The path of one ray to form caustics in an n-p-n junction (where the p region is coloured gray). Incident waves approach the junction (with the first interface at $x = 0$) at an angle θ_c (in the conduction band), and refract at an angle θ_v (in the valence band). Outgoing rays form at an angle θ_c (since we assume a symmetric junction). The caustics overlaid are formed when Eqn. 3.42 matches the position of the second interface.

$$\epsilon = -\frac{u(2 + (\alpha - 4)\alpha)}{\alpha - 2}. \quad (3.44)$$

Generally for a system of trajectories that cover a total path length ηl (to match the superlattice period in Section 3.2, and where $\eta \in \mathbb{N}_1$), and assuming the first trajectory is in the conduction band, we can describe the trajectories as

$$y = \eta(1 - \alpha)l \tan \theta_c + (\eta - 1)\alpha l \tan \theta_v + x \tan \theta_v. \quad (3.45)$$

A cusp is found to form at

$$x_{\text{cusp}} = l(\alpha - n\eta + (n - 1)\alpha\eta), \quad (3.46)$$

and since in this case of an integer multiple of l , $x_{\text{cusp}} = \alpha l$, we find that $n = \alpha/(\alpha - 1)$, i.e., independent of η . The energy is therefore always Eqn. 3.43 when the length of the trajectories have a period equal to an integer multiple of the superlattice system's period.

If we are interested in the trajectories forming a cusp after travelling a total path length $(\eta - 1/2)l$, we must equate Eqn. 3.46 with zero, finding

$n = ((\eta - 1)\alpha)/((\alpha - 1)\eta)$, such that

$$\epsilon = -\frac{u(\alpha^2 + \eta - 2\alpha\eta)}{\alpha - \eta}. \quad (3.47)$$

This form recovers Eqn. 3.44 for $\eta = 2$, as expected.

Since we are interested in mapping the energy at which cusps form at interfaces to the problem of a periodic potential profile, we use the energies given by Eqn. 3.43 in later analysis. Given this energy (at which caustics form at various interfaces), it is interesting to see if this maps to any distinctive features in the energy surfaces produced by a periodic modulation of the potential. To do this we select energy planes that match the criterion

$$|\epsilon_{\text{cut}} - \epsilon| \leq \delta, \quad (3.48)$$

where ϵ_{cut} is Eqn. 3.43, ϵ is the value of energy in the surface plots, and δ is a small parameter to control the thickness of the energy plane selected. The value of ϵ_{cut} is shown as the horizontal line in Figs. 3.13, which show cross-sections of the 3D energy surfaces for fixed ϕ . We note that while ϵ_{cut} slices through surfaces for certain values of parameters u and α , it does not coincide with the energies at which Dirac cones are formed in the general case. For $\alpha = 1/2$, however, the energy plane cuts at $\epsilon = 0$, coinciding with the point of the Dirac cones (see Fig. 3.7(a)). The energy planes selected by Eqn. 3.48 when applied to certain energy surfaces are shown in Figs. 3.7(d)–(f). In other cases the energy at which cusps form at regular interfaces does not slice through an energy surface at all: it occurs between surfaces. This suggests that most features (e.g., the Dirac cones) of the superlattice energy spectrum are attributable to interference effects from smaller length scales, since there are no visible singular features at the energies where classical catastrophe theory suggests cusps form at regular interfaces. However, there may be small

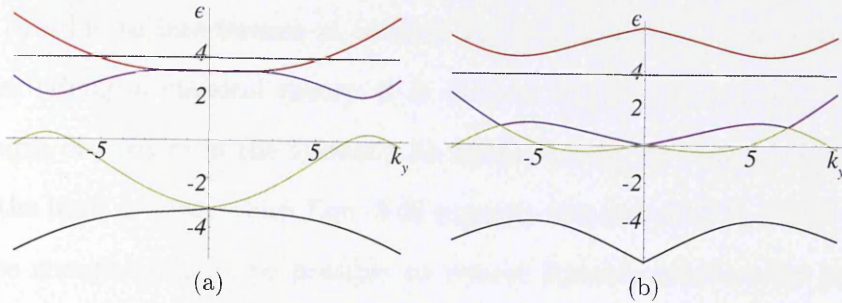


Fig. 3.13: Plots of Eqn. 3.29 for fixed Bloch phase, using parameters $\alpha = 0.4$, $u = 6\pi$, and (a) $\phi = \pi$ (b) $\phi = 0$. Dashed isoenergetic lines are shown to define the energy at which caustics (from rays traversing a length l equal to the period of the potential system), occur with $\delta = 0.7$ and $\epsilon_{\text{cut}} = 3.77$, as defined in Eqn. 3.48.

features that would warrant further investigation. Furthermore, it may be possible to investigate classically-induced features in the limit of the carrier wavelength $\lambda \rightarrow 0$ (that is, $\epsilon \rightarrow \infty$), since classical theories are valid at length scales greater than the quasiparticle wavelength.

3.5 Conclusion

We introduced transfer matrices by calculating the transmission of ballistic carriers through n-p-n junctions in monolayer and bilayer graphene. We then extended this analysis by introducing the modulation of a periodic potential profile, which introduces extra Dirac points in the energy dispersion. Classical catastrophe theory was then employed to describe caustics and cusps in a system with a periodic potential profile, for cusps forming at regular interfaces. The periodicity of the formation of cusps was matched with the periodicity of the superlattice, where we determined that the energy at which these cusps form is independent of the number of periods of the superlattice traversed. We map this energy to the energy spectrum found when analysing monolayer graphene with a periodic potential profile, and find that they do not correspond to features in the electronic dispersion of the system in the general case (the exception being for $\alpha = 1/2$ where the n and p regions are of equal width). This suggests that the main features seen in the

system are due to interference at smaller length scales than catastrophe theory operates. (Being a classical theory, it is valid at length scales greater than the wavelength of carriers in the system.) As further study, we could minimise λ by taking the limit $\epsilon \rightarrow \infty$, which Eqn. 3.43 suggests means taking the limit $u \rightarrow \infty$. At these energies it may be possible to resolve features attributable to such a classical theory. Furthermore, there may be subtle features in the energy spectrum at the energies that cusps form that this analysis has not shown; it may warrant further investigation to attempt to resolve these.

Chapter 4

Characterisation of Moiré Patterns Formed by Incommensurate Hexagonal Lattices

Whenever two regular hexagonal lattices are overlaid at an angle and/or with a small difference in lattice constants, Moiré patterns appear. Periodic modulations forming superlattices have been observed experimentally in scanning tunnelling microscopy (STM) studies of graphite [92–96], and also studied theoretically in graphene [97–100]. In this Chapter we develop the theory of Moiré patterns and create a computer model to allow experimentally observed patterns to be characterised by angle (and perhaps additionally lattice constant). Furthermore, the model has also been written to (optionally) selectively show only those lattice sites that are nearly commensurate with sites in another layer. The atoms at these sites are hypothesised to dominate interlayer interaction effects.

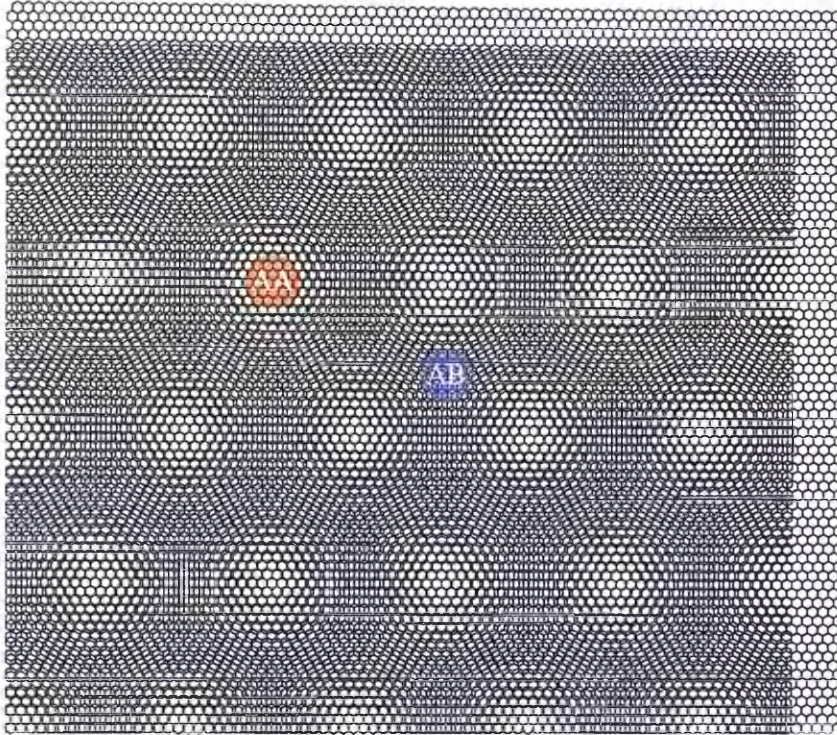


Fig. 4.1: Generated Moiré pattern showing the formation of a superlattice, formed by two hexagonal lattices, with lattice constants a and $a(1 - \sqrt{2}/25)$. (The latter value is chosen to force the model to use an irrational number for the lattice constant.) AA and AB stacking alignments are highlighted.

4.1 Theory of Moiré Patterns

The theory of geometric Moiré patterns (outside of solid state physics) has been well researched [101–105], often focusing on gratings and other simple structures. Usually, the spacing between each set of grids is slightly different, or there is a small amount of rotation. For the case of two layers with hexagonal lattices, the Moiré pattern formed is also a hexagonal lattice, defined as a superlattice (see Fig. 4.1). Each hexagon formed is called a supercell. For the construction of this model, each layer is a hexagonal lattice, with lattice spacing and rotation angle defined independently. We make a general assumption that there can be a difference in rotation angle θ between any two layers, and that the bond lengths of layers one and two are l and $l(1 - \delta)$ respectively; $\delta \in [0, 0.05]$ is small and irrational. l is shown in Fig. 4.2. Throughout this Chapter, the use of the prime symbol designates

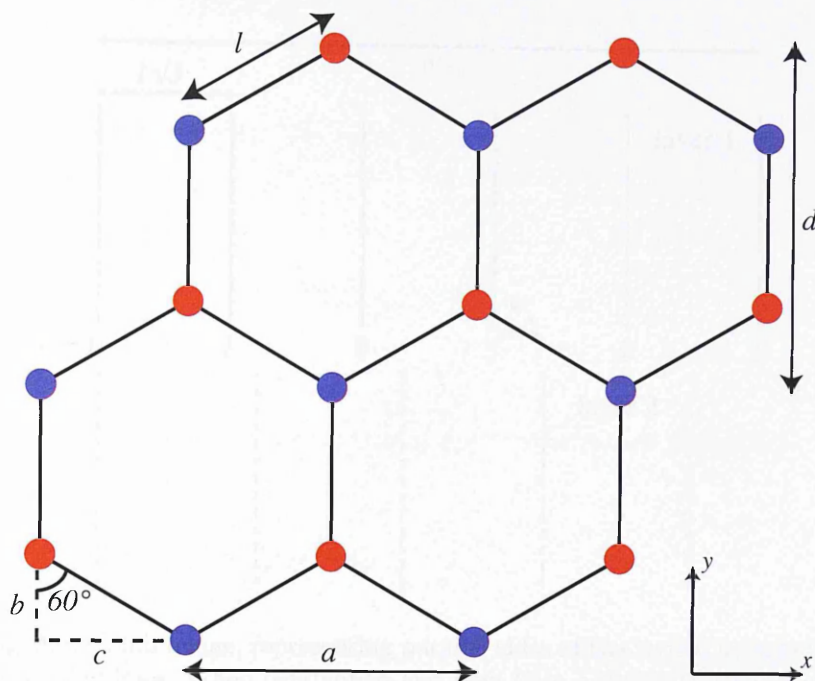


Fig. 4.2: Schematic showing the geometry of a hexagonal lattice. Sites in sublattice A (B) are coloured red (blue). $a = 2c = \sqrt{3}l$, $b = l \cos 60^\circ = \frac{l}{2}$, $c = l \sin 60^\circ = \frac{\sqrt{3}l}{2}$, $d = l + 2b = 2l$.

a property of the superlattice.

4.1.1 Analysis Without Rotation

With no rotation, the calculation of the distance between points in the centre of adjacent hexagons in the superlattice is straightforward. We can model each hexagon formed by six lattice sites in each layer as a set of pairs of parallel lines, each separated by length $a = \sqrt{3}l$. Thus, a hexagonal grid forms combs of parallel lines, and the Moiré pattern formed will be the superposition of the pattern of parallel lines in one direction, plus two other equivalent patterns rotated by 120° . Light areas in a Moiré pattern are formed when lines of one layer are directly above the lines of the other layer: they are superimposed. The dark areas are formed when lines from one layer are in the middle of the lines from the other layer: from a distance, there is less white space (see Fig. 4.3). To find the distance between a dark region and a light region in the Moiré pattern (and thus, half

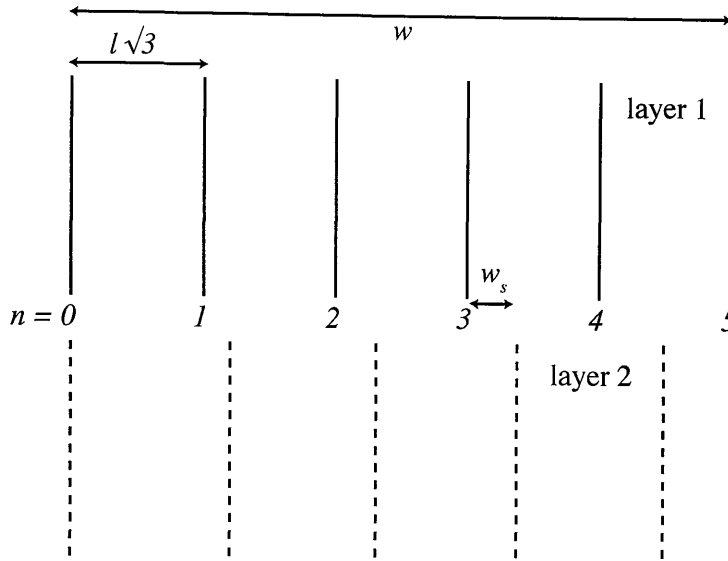


Fig. 4.3: Comb image, representing parallel sides of the lattice hexagons as parallel lines. When overlapped and seen from a distance, they produce a periodic Moiré pattern.

the distance between two dark regions, length a'), we make a few statements, referencing Fig. 4.3. At the left of the image, the lines start superimposed. This is a light region. Over the width of the image, layer two lines gradually span out until after distance w they form in the middle of the layer one lines. This is the centre of a dark region, where the centre of layer one's lines is at a distance $\sqrt{3}l/2$ (i.e., half way). If we count the lines, we see that the n^{th} line in layer one forms at a distance $n\sqrt{3}l$ from the left of the image, where $n \in \mathbb{Z}$. The n^{th} line on layer two is formed at a distance $n\sqrt{3}l(1 \pm \delta)$. The lines in layer two are thus shifted by $w_s = n\sqrt{3}l - (n\sqrt{3}l \pm \sqrt{3}\delta l) = \pm n\sqrt{3}\delta l$.

As stated previously, the dark region is found when lines from layer two form in the middle of lines from layer one, which in this formalism is when the shift w_s is equal to the middle of layer one's lines,

$$n\sqrt{3}\delta l = \frac{\sqrt{3}l}{2} \Rightarrow n = \frac{1}{2\delta}, \quad (4.1)$$

(dropping the “ \pm ”, not allowing negative n). The total distance from the left of the image (the middle of a light patch) to the centre of a dark patch is

$$w = \sqrt{3}ln = \frac{\sqrt{3}l}{2\delta}, \quad (4.2)$$

and hence the distance from one light patch to another or one dark region to another is twice this distance:

$$a' = 2w = \frac{\sqrt{3}l}{\delta}. \quad (4.3)$$

This is the distance between the centres of any two adjacent supercells.

Counting Hexagons in Supercells

It is easy to determine the number of hexagons from layer one along a length a' . Each small hexagon has a length (between two parallel lines) $a = \sqrt{3}l$. Hence, the number of hexagons from layer one seen along length a' in the Moiré pattern is

$$\frac{a'}{a} = \frac{1}{\delta}. \quad (4.4)$$

The number of hexagons from layer one in each supercell can be found by dividing the area of the supercell hexagon by the area of a hexagon from layer one. The area of a hexagon is given by

$$A = \frac{3}{2}\sqrt{3}l^2. \quad (4.5)$$

The length of a side of a supercell hexagon is $l' = a'/\sqrt{3} = l/\delta$, hence the number of hexagons from layer one seen in a supercell is

$$\frac{\frac{3}{2}\sqrt{3}\frac{l^2}{\delta^2}}{\frac{3}{2}\sqrt{3}l^2} = \frac{l^2}{\delta^2 l^2} = \frac{1}{\delta^2}. \quad (4.6)$$

We notice from Eqns. 4.4 and 4.6 that these quantities are dependent on δ alone.

4.1.2 Fourier Analysis Method for Rotated Layers

To describe rotated layers, we again imagine our hexagonal lattice as a set of parallel lines arranged as a grid. A popular way to analyse this situation is to transform the real image into a frequency spectrum via a Fourier transform. The assumption made here is that $\delta \ll 1$. Given that δ is in the range $[0, 0.05]$, the condition is satisfied. We map out the general method required to analyse Moiré patterns in this way, using notation as in Amidror [101, 102]. The only assumption made about the images is that they are periodic and symmetric, and exist in a 2D real space (x, y) . Each image is represented by a reflectance function r , which gives a value in the range $[0, 1]$: 0 for darkness, 1 for perfect reflectance. Thus, superposition is multiplicative: a black image on a white (transparent) image will still produce black. Hence,

$$r(x, y) = r_1(x, y)r_2(x, y) \cdots r_m(x, y) = \prod_{i=1}^m r_i(x, y). \quad (4.7)$$

Fourier transforming $r_i(x, y)$ produces $R_i(u, v)$, which is shown as an impulse in the frequency plane (u, v) . The convolution theorem shows that

$$R(u, v) = R_1(u, v) * R_2(u, v) * \cdots * R_m(u, v). \quad (4.8)$$

Each impulse has an index, together with its geometric location on the (u, v) plane, and an amplitude. In Fig. 4.4 \mathbf{f} is a frequency vector, pointing from the origin to the impulse location. θ is perpendicular to the gratings in the real image, as shown in Fig. 4.4's inset.

Another assumption made in this method is that the images we consider are symmetric: for every \mathbf{f} , there is a corresponding $-\mathbf{f}$. Each grid is represented by the frequency vector \mathbf{f} , such that multiple images superimposed can now be represented by multiple frequency vectors,

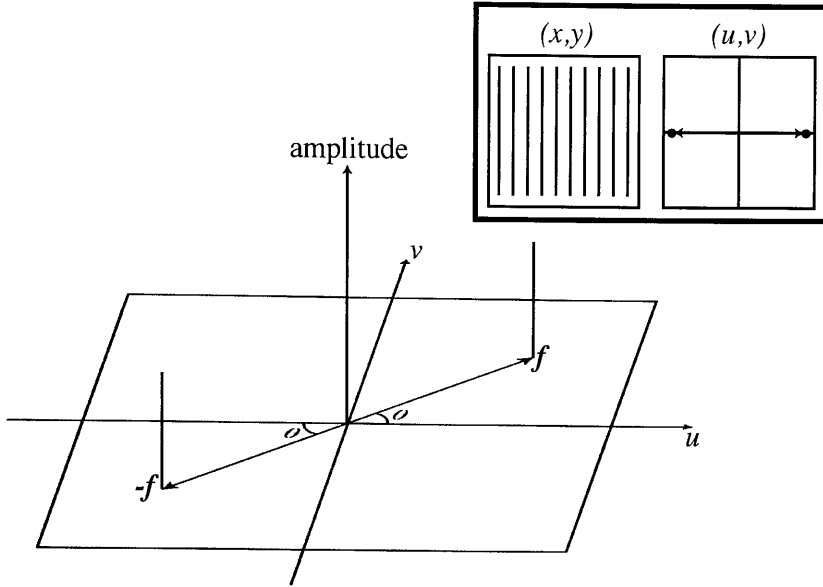


Fig. 4.4: (u, v) frequency plane showing two impulses at \mathbf{f} and $-\mathbf{f}$. Inset shows that frequency vector \mathbf{f} is perpendicular to the gratings.

$$\mathbf{f} = \sum_{i=1}^m \mathbf{f}_i, \quad (4.9)$$

where each \mathbf{f}_i has associated coordinates (f_i, θ_i) . Hence the sum vector \mathbf{f} is given by

$$\begin{aligned} |\mathbf{f}| &= f = \sqrt{u^2 + v^2}, \\ T &= \frac{1}{f}, \\ \theta &= \arctan \frac{v}{u}, \end{aligned} \quad (4.10)$$

where f is the length of the frequency vector, T is its period, and θ is the angle it makes with the positive side of the u axis in frequency space. In Cartesian coordinates,

$$\begin{aligned} u &= f_1 \cos \theta_1 + \cdots + f_m \cos \theta_m, \\ v &= f_1 \sin \theta_1 + \cdots + f_m \sin \theta_m. \end{aligned} \quad (4.11)$$

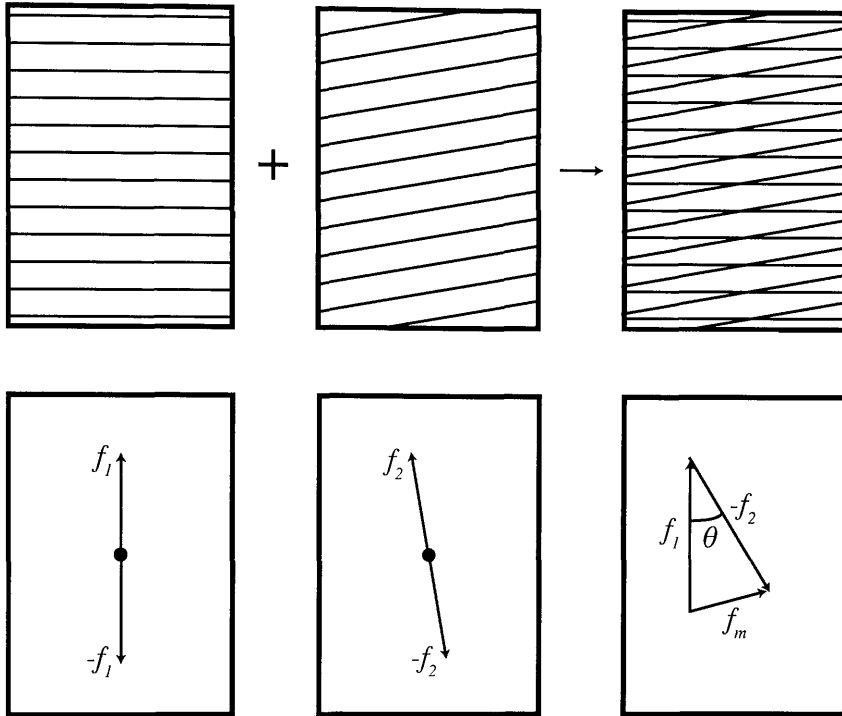


Fig. 4.5: The top row shows real images of parallel grids, superimposed in the third image to show the formation of Moiré patterns. The bottom row shows the corresponding frequency vectors for each pattern and the superimposed image, including the effective Moiré frequency vector f_m .

Many Moiré patterns are possible, but not all are resolvable; for this to be possible they have to be in the visible circle region. For example, for our grid example the Moiré pattern observed is formed due to $f_m = f_1 - f_2$, with an associated period $T_m = 1/f_m$ (see Fig. 4.5).

Looking at Fig. 4.5, and not assuming that f_1 and f_2 are of equal length, we deduce from the law of cosines that

$$f_m = \sqrt{f_1^2 + f_2^2 - 2f_1f_2 \cos \theta}. \quad (4.12)$$

Given that $f_1 = 1/T_1$ and $f_2 = 1/T_2$, we find that

$$\begin{aligned}
T_m &= \frac{1}{\sqrt{f_1^2 + f_2^2 - 2f_1f_2 \cos \theta}} \\
&= \frac{1}{\sqrt{\frac{1}{\frac{1}{T_1^2} + \frac{1}{T_2^2} - \frac{2 \cos \theta}{T_1 T_2}}}} \\
&= \frac{1}{\sqrt{\frac{T_2^2}{T_1^2 T_2^2} + \frac{T_1^2}{T_1^2 T_2^2} - \frac{2T_1 T_2 \cos \theta}{T_1^2 T_2^2}}} \\
&= \frac{T_1 T_2}{\sqrt{T_1^2 + T_2^2 - 2T_1 T_2 \cos \theta}}. \tag{4.13}
\end{aligned}$$

It is now easy to apply this to the case we are interested in: hexagonal lattices. Modelling the hexagons as a series of parallel lines as stated previously, we define those composed from layer one to be separated by a distance $a_1 = \sqrt{3}l$. Lines from layer two are separated by a distance $a_2 = \sqrt{3}l(1 - \delta)$. To map to the Amidror notation in [101, 102], it is noted that $a_1 \equiv T_1$ and $a_2 \equiv T_2$.

Since we can now follow the same derivation as the general method, we can take Eqn. 4.13 and substitute our values for T_1 and T_2 . Letting $a = \sqrt{3}l$, and again defining the distance from one Γ' point to another in the superlattice as a' , we see that

$$a' = \frac{a^2(\delta - 1)}{\sqrt{a^2(2 + (\delta - 2)\delta + 2(\delta - 1) \cos \theta)}}. \tag{4.14}$$

If the angle between our two grid patterns, θ , is now set to zero, we see that

$$a' = \frac{a(1 - \delta)}{\delta}, \tag{4.15}$$

in contrast to Eqn. 4.3. However, it is easily seen that these solutions converge as $\delta \rightarrow 0$, so provided we stay in the regime of $\delta \ll 1$ as assumed at the start of this Section, this is correct.

One can also make a corresponding simplification to Eqn. 4.14, when $a_1 \equiv a_2$ (i.e., when $\delta = 0$). We find that

$$a' = \frac{a}{\sqrt{2 - 2 \cos \theta}}, \tag{4.16}$$

which, after using the trigonometric identity $\cos(2A) = 1 - 2\sin^2 A$, simplifies to

$$a' = \frac{a}{2|\sin \frac{\theta}{2}|}. \quad (4.17)$$

It is also possible to calculate the angle at which the superlattice is formed. The effective Moiré frequency vector \mathbf{f}_m makes an angle $\phi' = \arctan(v/u)$ with the horizontal positive axis in the frequency plane. If layer one is rotated by angle θ_1 from the horizontal axis and layer two is rotated by θ_2 from layer two (and thus $\theta_1 + \theta_2$ from the horizontal axis, the vector subtraction shows that

$$\mathbf{f}_m = \mathbf{f}_1 - \mathbf{f}_2 = (f_1 \cos \theta_1 - f_2 \cos(\theta_1 + \theta_2))\hat{\mathbf{u}} + (f_1 \sin \theta_1 - f_2 \sin(\theta_1 + \theta_2))\hat{\mathbf{v}}. \quad (4.18)$$

Hence,

$$\phi' = \arctan \left(\frac{f_1 \sin \theta_1 - f_2 \sin(\theta_1 + \theta_2)}{f_1 \cos \theta_1 - f_2 \cos(\theta_1 + \theta_2)} \right). \quad (4.19)$$

For the case we are interested in, where layer one has no rotation and we are only concerned with the relative rotation between layers, θ_2 , we set $\theta_1 = 0$ and see that

$$\phi' = \arctan \left(\frac{T_1 \sin \theta_2}{T_1 \cos \theta_2 - T_2} \right), \quad (4.20)$$

which simplifies to

$$\phi' = \cot^{-1}((\delta - 1 + \cos \theta_2) \csc \theta_2). \quad (4.21)$$

This is useful when making comparisons to STM images, later in the Chapter.

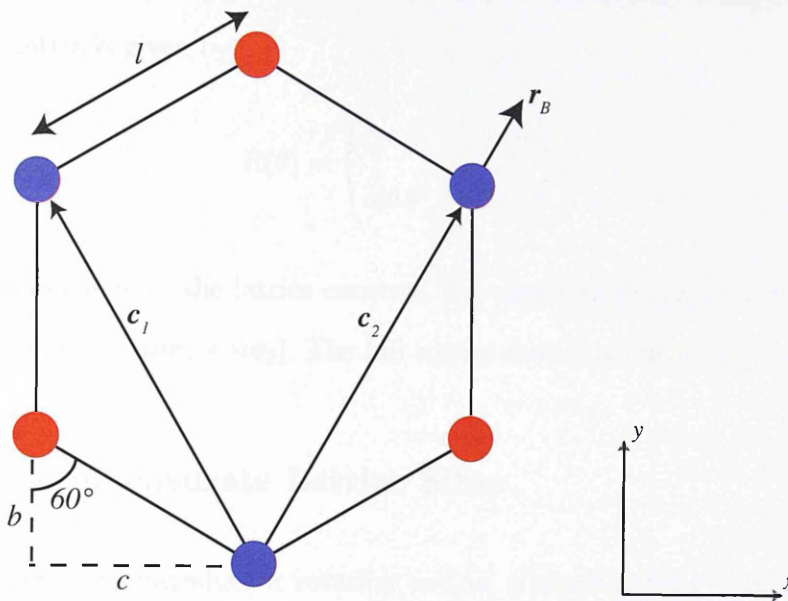


Fig. 4.6: Lattice geometry showing c_i and r_B vectors used in the calculation of commensurate sites.

4.2 Modelling Moiré Images

In this Section we construct a computer model to layer hexagonal lattice sheets. We define the bottom left of any image as the origin. The lattice vectors used to specify the locations of lattice sites are \mathbf{a}_i defined in Fig. 4.2, such that any site (on one sublattice) is connected via the vector $\mathbf{R}_A = a(m\mathbf{e}_1 + n\mathbf{e}_2)$, where a is the lattice constant and \mathbf{e}_i are unit vectors following the direction of \mathbf{a}_i , and $\{m, n\} \in \mathbb{Z}$. Bonds between sites must be rendered in a separate way: one complete hexagon (comprising of six lattice sites) is generated and then iterated with an offset each time. The Cartesian coordinates specifying six points in real space for the bonds are

$$\begin{aligned} \text{bonds}(x, y) = & (x, y), (x + c, y + b), (x + c, y + l + b), \\ & (x, y + d), (x - c, y + l + b), (x - c, y + b), \end{aligned} \quad (4.22)$$

where b , c , d , and l are also specified in Fig. 4.2. The model then simply iterates this several times, to produce the complete hexagonal lattice. Rotation is introduced

by including the rotation matrix such that $\mathbf{R}_A = R(\theta)a(m\mathbf{e}_1 + n\mathbf{e}_2)$, where the rotation matrix is given by

$$R(\theta) = \begin{pmatrix} \cos \theta & -\sin \theta \\ \sin \theta & \cos \theta \end{pmatrix}, \quad (4.23)$$

and a small change in the lattice constant δ is also introduced such that finally, $\mathbf{R}_A = R(\theta)a(1 + \delta)(m\mathbf{e}_1 + n\mathbf{e}_2)$. The full source code is given in Appendix B.

4.2.1 Commensurate Lattice Sites

It is of interest to introduce a rotation and/or a small difference in the lattice constants between layers, and then see which sites are nearly commensurate with those in other layers (up to a threshold given as a parameter). To explain the algorithm we use the example of hexagonal boron nitride (hBN) as layer one and graphene as layer two. For each lattice site in the hBN layer, we solve two equations (for the two sublattices in the graphene layer):

$$\text{point} + (0, l) = R(\theta)(\alpha_A\mathbf{c}_1 + \beta_A\mathbf{c}_2), \quad (4.24)$$

$$\text{point} = R(\theta)(\alpha_B\mathbf{c}_1 + \beta_B\mathbf{c}_2), \quad (4.25)$$

for α_i and β_i , where $\alpha_i, \beta_i \in \mathbb{R}$, and $i \in \{A, B\}$. “point” is the coordinate of a site in the hBN layer, which is already known. \mathbf{c}_i are lattice vectors in the graphene layer, and are defined as $\mathbf{c}_1 = (-c, l + b)$, $\mathbf{c}_2 = (c, l + b)$, shown in Fig. 4.6. Eqn. 4.24 differs from Eqn. 4.25 by adding a shift to jump to the other sublattice. Eqns. 4.24 and 4.25 are solved separately for α_i and β_i (depending on which sublattice may be commensurate, A or B), and then the vectors \mathbf{r}_A and \mathbf{r}_B are calculated as

$$\mathbf{r}_A = [\alpha_A - \text{round}(\alpha_A)] R(\theta)\mathbf{c}_1 + [\beta_A - \text{round}(\beta_A)] R(\theta)\mathbf{c}_2, \quad (4.26)$$

and the equivalent for \mathbf{r}_B . The function $\text{round}(x)$ simply rounds a real number to the nearest integer. We then test whether $|\mathbf{r}_A| = \sqrt{\mathbf{r}_A \cdot \mathbf{r}_A} < t$ (and the same for

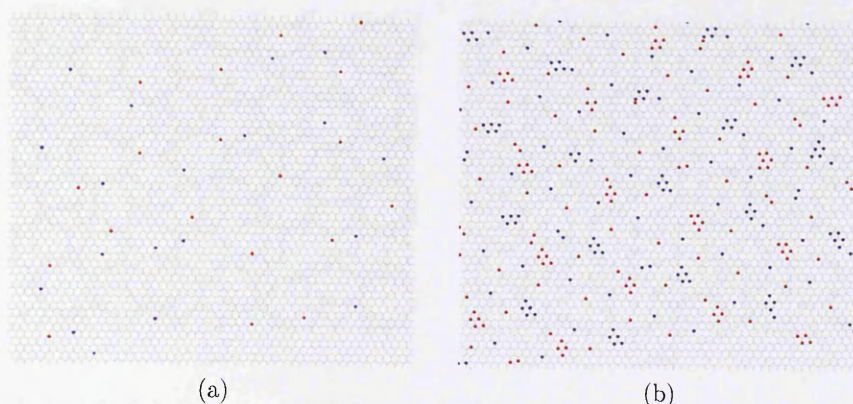


Fig. 4.7: (a) Atomic model of a 12 nm^2 graphene layer with hBN below, rotated at an angle of 10° . Only graphene sites that are almost directly above boron or nitrogen sites are shown, coloured red (blue) for graphene sublattice A (B). (b) Atomic model of a 12 nm^2 monolayer graphene layer below two layers of hBN, the first rotated by 5° relative to graphene, the second by 10° . Only those sites in the hBN layer that are nearly commensurate with sites from sublattice A (B) in the graphene layer are rendered, coloured red (blue).

\mathbf{r}_B), where t is a threshold. If either is true, the lattice site in the hBN layer is within the proximity of a site in the graphene layer, so it is rendered. A threshold of $t = l/6$ is chosen to allow for sites to be drawn that are within the radius of a lattice site in the graphene layer (assuming the site is to have a diameter of about $l/3$ when rendered). Figs. 4.7(a) and 4.7(b) demonstrate this. Fig. 4.7(a) shows commensurate sites when a layer of hBN is placed below monolayer graphene at an angle of 10° , while Fig. 4.7(b) shows monolayer graphene below two layers of rotated hBN.

Angles of Commensurability

Commensurate formations can also be found for certain angles of rotation (with the same lattice spacing), for example in Fig. 4.8(a), which shows two layers of graphene with a relative rotation of 32.2° (clockwise). Fig. 4.8(b) is analogous to Cisternas et al. [106, Fig. 1]. The model consists of a three layer unit supercell; the two lower layers present the usual AB stacking sequence of the bulk hexagonal graphite crystal. The top layer presents a clockwise rotation angle of 21.8° .

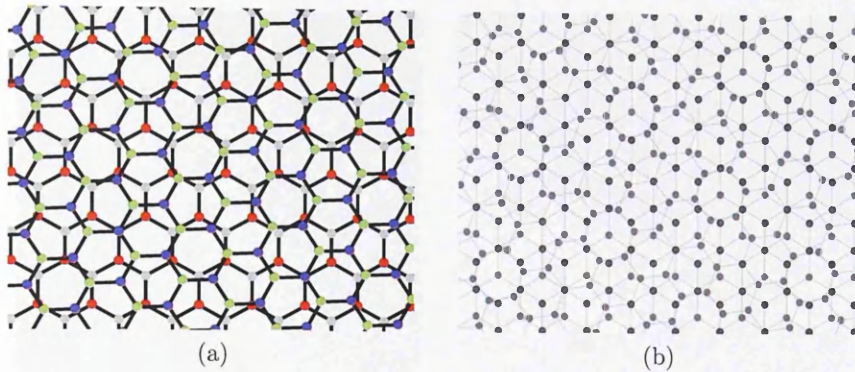


Fig. 4.8: (a) Commensurability angle formed by turbostratic graphene with a relative angle of -32.2° . (b) Three layer unit supercell; the two lower layers present the usual AB stacking sequence of the bulk hexagonal graphite crystal. The top layer presents a clockwise rotation angle of 21.8° . (b) is analogous to Cisternas et al. [106, Fig. 1].

4.3 A Systematic Study and Comparison of Moiré Model Images to Experimental Images

We can now compare images produced by the model to those produced in STM experiments. Moiré images have been found when imaging a few graphitic layers, as well as when graphene is layered on top of hexagonal boron nitride (hBN). The latter is of interest since (when grown on SiO_2 for example) impurities reduce the mobility of carriers in graphene [107]. Thus it is desirable to use a different substrate material; one such contender is hBN since it has a large band gap (5.97 eV [108]) and is flat. Both graphene and hBN have hexagonal lattice structures, though at $a \approx 2.50\text{\AA}$, hBN's lattice constant is slightly longer than graphene's [109, 110] (see Fig. 4.2). Thus, if hBN is used as a substrate for few-layer graphene, one may expect to see Moiré patterns. The same can be said for incommensurate few layers of graphene, for example with a relative rotation (turbostratic graphene).

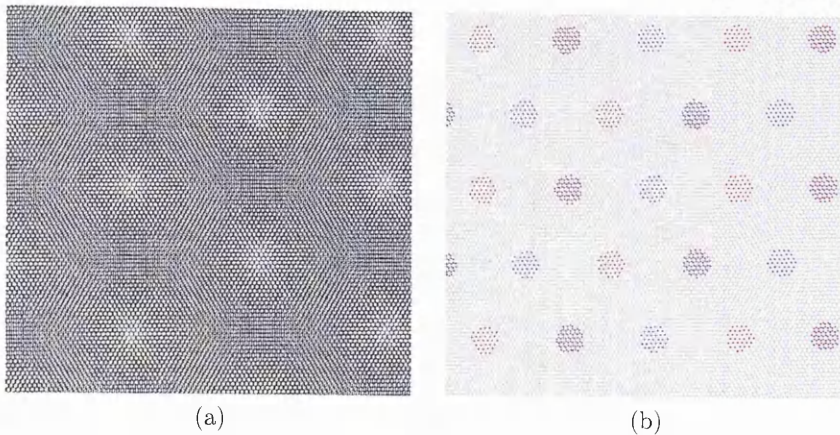


Fig. 4.9: (a) Moiré image formed by two layers of graphene with a relative angle of 1.8° . An effective area of 22.5 nm^2 is shown. (b) The same image showing commensurate sites causing a periodic modulation of the density of states.

4.3.1 Scanning Tunneling Microscope Images of Graphitic Layers

Kuwabara et al. [92] reported on Moiré patterns seen in STM images of graphite with a superlattice period of approximately 7.7 \AA . Using Eqn. 4.17, we concur that the image seen can be explained due to two rotated layers of graphene (i.e., monolayer graphene rotated on a graphite crystal) with an angle of 1.8° (given graphite's lattice constant of 2.46 \AA). The superlattice's orientation is thus (from Eqn. 4.21) rotated by an angle of 89.1° . The computer model is used to accurately reproduce the experimental STM image seen, while also showing commensurate lattice sites (see Figs. 4.9). These sites will affect conductivity and density of states more than other sites, explaining the periodic perturbation in the surface density of states. (Scanning Tunnelling Microscopy will pick up these fluctuations since the tunnelling current is directly proportional to the surface density of states [111].)

Cee et al. [112] found Moiré patterns due to a single graphitic layer on top of a Bernal-stacked bilayer. The model accurately reproduces the simulated STM image (Fig. 4.10(a)). The top monolayer is rotated by 5° ; commensurate sites are shown in Fig. 4.10(b).

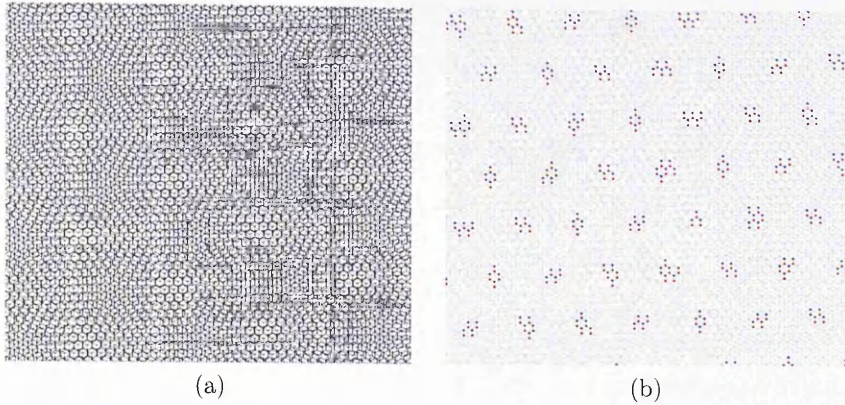


Fig. 4.10: (a) Moiré image formed by two Bernal-stacked layers of graphene with a rotated monolayer on top (with a relative angle of 1.8°). (b) The same image showing nearly commensurate sites causing a periodic modulation of the density of states. Sites in the Bernal-stacked layers that are nearly commensurate with sites in the A (B) sublattice of the rotated layer are coloured red (blue).

Finally, Xhie et al. [113] observed superlattices on four samples of graphite: a monolayer of graphene rotated by an angle relative to the graphite crystal below. The angles ranged from $\theta = 2.1\text{--}8.3^\circ$. A Moiré image analogous to [113, Fig. 5(a)] is shown, together with the commensurate sites, in Figs. 4.11.

4.3.2 Monolayer and Bilayer Graphene on hBN

Given hBN's slightly larger lattice constant compared to graphite's, a few-layer stack of hBN and graphene would present a Moiré pattern even with no rotation. This has been seen in STM images by Decker et al. [114], compared in Figs. 4.12 (with a relative angle of 4°). Xue et al. [115] have also studied Moiré patterns produced by graphene on hBN; a comparison is shown in Figs. 4.13. The hBN layer is rotated relative to the graphene layer by 10.9° . The model predicts the same pattern found in the experiments.

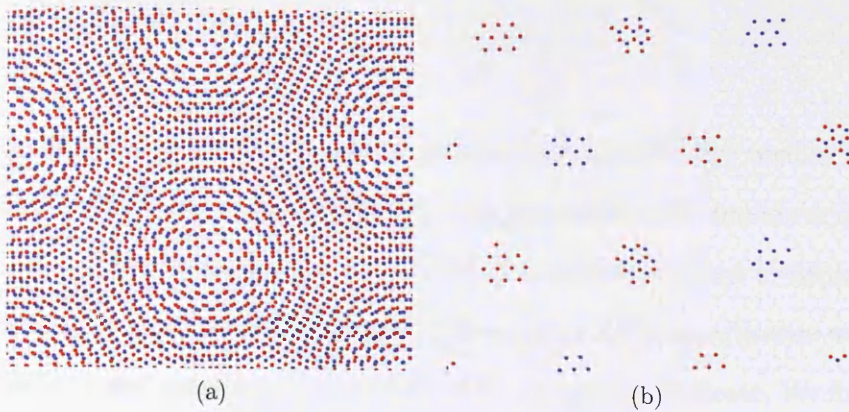


Fig. 4.11: (a) Moiré image produced by overlapping two graphitic monolayers with a relative rotation of 3.5° . Lattice sites from sublattice A (B) are coloured red (blue) (for both layers). (b) The same layer configuration as in (a) but only showing the lattice of the non-rotated layer (no sites); only nearly-commensurate sites are rendered. Sites in the rotated layer that are nearly commensurate with those from sublattice A (B) in the other layer are coloured red (blue).

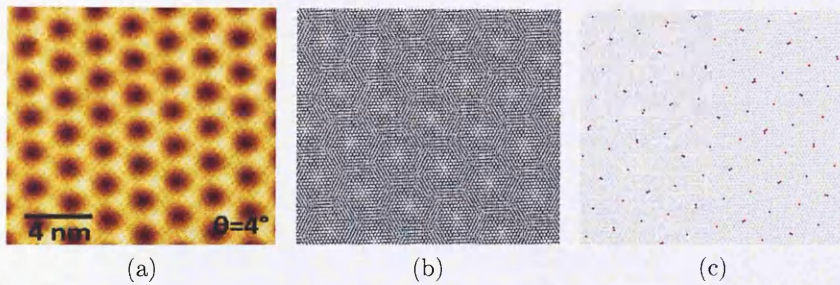


Fig. 4.12: (a) 20 nm^2 STM image of graphene-hBN surface topology with a relative angle of 4° , adapted from Decker et al. [114, Fig. 2(c)]. (b) Atomic model image using equivalent parameters for surface area and relative rotation. (c) Atomic model image showing nearly-commensurate sites. Lattice sites in the hBN layer that are almost commensurate with graphene sublattice A (B) sites are coloured red (blue).

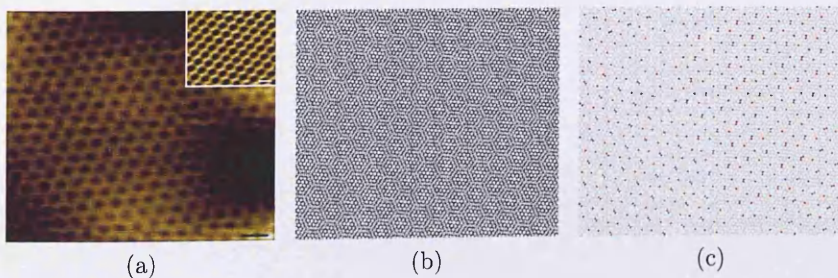


Fig. 4.13: Graphene monolayer above hBN with a relative angle of -10.9° . (a) 16 nm^2 STM image of graphene-hBN surface topology, adapted from Xue et al. [115, Fig. 2(c)]. (b) Atomic model image using equivalent parameters for surface area and relative rotation. (c) Atomic model image showing nearly-commensurate sites. Lattice sites in the hBN layer that are almost commensurate with graphene sublattice A (B) sites are coloured red (blue).

4.4 Conclusion

We have characterised geometric Moiré patterns formed when two regular patterns overlap, induced by either a small difference in their lattice parameters or their angle of rotation. We developed and implemented a computer model to demonstrate this effect and compared model images to those from STM experiments with few-layer graphene and graphene on a hexagonal boron nitride substrate. We find that, empirically, the model characterises the Moiré patterns seen in these experiments well. Additionally, the model also shows patterns of commensurate lattice sites.

Chapter 5

Summary and Conclusions

In this Thesis we have characterised electronic and transport properties of few-layer graphene systems. In Chapter 1 we introduced graphene and described the tight binding model that is frequently used in its analysis. We derived Hamiltonians near the \mathbf{K} points for monolayer and bilayer graphene, and reviewed important phenomena that account for the results seen in later Chapters.

In Chapter 2 we extended the earlier derived low energy effective Hamiltonian for bilayer graphene to incorporate a spatially dependent electrostatic potential consistently. Our calculations show that the angle-dependent transmission through an n-p junction is $T(\theta) \cong \sin^2(2\theta) - (2u/3\gamma_1) \sin(4\theta) \sin(\theta)$. A spatially dependent electrostatic potential affects the angle where perfect transmission is seen, slightly increasing it. In addition, the conductance is slightly reduced to $G \cong 2.10 e^2 w k_F / \pi \hbar$, whereas the Fano factor is slightly increased to $F \cong 0.241$ (both for $u = 40$ meV). Even though our calculations show that the transmission, conductance and Fano factor are changed when these spatially dependent terms in the effective Hamiltonian are kept, we conclude that the approximate low energy Hamiltonian derived in McCann and Fal'ko [7] is very good in this regime. Additionally, a low energy effective Hamiltonian with a spatially dependent asymmetry in the on-site energy between layers is derived. One possible direction of further research is to use this

Hamiltonian to extend the analysis of pseudospintronics in bilayer graphene (first carried out by San-Jose et al. [116]). The calculation of pseudospin for a low energy bilayer graphene system (Section 1.4.1) shows that it has a phase twice that of momentum, $\langle \boldsymbol{\sigma} \rangle = \cos 2\phi \mathbf{i} + \sin 2\phi \mathbf{j}$. If we introduce an asymmetry in the on-site energies between the two layers to give sites in layer one (two) an on-site energy of $\Delta/2$ ($-\Delta/2$), the pseudospin is found to be $\langle \boldsymbol{\sigma} \rangle_{\pm} = \pm \sqrt{1 - \zeta^2} (\cos 2\phi \mathbf{i} + \sin 2\phi \mathbf{j}) + \zeta \mathbf{k}$. ($\langle \boldsymbol{\sigma} \rangle_+$ ($\langle \boldsymbol{\sigma} \rangle_-$) denotes pseudospin in the conduction (valence) band, and $\zeta = \Delta/2\epsilon$.) This is of interest due to the out of plane component. At $\epsilon = \pm\Delta/2$ (the minima and maxima of the low energy bands in the energy spectrum with an induced gap), the in-plane pseudospin components vanish: we are left with the out of plane component only. However, given that the corrections in the derived low energy effective Hamiltonian are small, any corrections to the pseudospin are also expected to be small. (These equations are derived more thoroughly in Appendix C.)

In Chapter 3 we introduced transfer matrices by calculating the transmission of ballistic carriers through n-p-n junctions in monolayer and bilayer graphene. We then extended this analysis by introducing the modulation of a periodic potential profile, which introduces extra Dirac points in the energy dispersion. Classical catastrophe theory was then employed to describe caustics and cusps in a system with a periodic potential profile, for cusps forming at regular interfaces. The periodicity of the formation of cusps was matched with the periodicity of the superlattice, where we determined that the energy at which these cusps form is independent of the number of periods of the superlattice traversed. We mapped this energy to the energy spectrum found when analysing monolayer graphene with a periodic potential profile, and found that they do not correspond to features in the electronic dispersion of the system in the general case (the exception being for $\alpha = 1/2$ where the n and p regions are of equal width). This suggests that the main features seen in the system are due to interference at smaller length scales than catastrophe theory operates. (Being a classical theory, it is valid at length scales greater than the wavelength of carriers in the system.) As further study,

we could minimise λ by taking the limit $\epsilon \rightarrow \infty$, which Eqn. 3.43 suggests means taking the limit $u \rightarrow \infty$. At these energies it may be possible to resolve features attributable to such a classical theory. Furthermore, there may be subtle features in the energy spectrum at the energies that cusps form that this analysis has not shown; it may warrant further investigation to attempt to resolve these.

In Chapter 4 we created a model to characterise the angles and commensurability of a few layers of hexagonal lattice materials, seen in STM images in experiments. The model allows for different lattice constants and rotations for each layer, as well as selectively showing lattice sites that are nearly commensurate with sites in other layers. This model was then used to find the angle of rotation of layers in various STM images from experiments involving multiple graphitic layers, turbostratic graphene, and graphene on hexagonal boron nitride.

In conclusion, we have shown that few-layer graphene is a very interesting material which shows enormous promise for innovative applications. Further research can also be conducted to analyse the effects of rotation and lattice incommensurability on the electronic properties of graphene few-layer systems, extending the work in Chapter 4.

Appendix A

Source Code for Drawing Energy Surfaces Due to a Periodic Modulation of Potential

In this Appendix we give the complete source code used in Chapter 3; longer lines are split with backslashes.

Monolayer Graphene

The energy surfaces for work in Section 3.2 were plotted using the following Mathematica code. First the central equation can be derived from transfer matrix formalism:

```
kx[\[Epsilon]_,u_,ky_,\[Alpha]_] := Sqrt[-ky^2 +(u \[Alpha]
+ \[Epsilon])^2];
kxp[\[Epsilon]_,u_,ky_,\[Alpha]_] := -Sqrt[-ky^2 +(u (1-\[Alpha]
- \[Epsilon])^2);
a12[\[Epsilon]_,u_,ky_,\[Alpha]_] := 1/(\[Epsilon]+u \[Alpha])
(-kx[\[Epsilon],u,ky,\[Alpha]] -I ky);
a22[\[Epsilon]_,u_,ky_,\[Alpha]_] := 1/(\[Epsilon]+u \[Alpha])
(kx[\[Epsilon],u,ky,\[Alpha]] -I ky);
```

```

b12[\[Epsilon]_,u_,ky_,\[Alpha]_] := 1/(\[Epsilon]-u (1-\[Alpha]))
(-kxp[\[Epsilon],u,ky,\[Alpha]] -I ky);

b22[\[Epsilon]_,u_,ky_,\[Alpha]_] := 1/(\[Epsilon]-u (1-\[Alpha]))
(kxp[\[Epsilon],u,ky,\[Alpha]] -I ky);

mA[\[Epsilon]_,u_,ky_,\[Alpha]_] :=
{{1,1},{a12[\[Epsilon],u,ky,\[Alpha]],a22[\[Epsilon],u,ky,\[Alpha]]}};

mB[\[Epsilon]_,u_,ky_,\[Alpha]_] :=
{{1,1},{b12[\[Epsilon],u,ky,\[Alpha]],b22[\[Epsilon],u,ky,\[Alpha]]}};

mC[\[Epsilon]_,u_,ky_,\[Alpha]_] := {Exp[I
kxp[\[Epsilon],u,ky,\[Alpha]] \[Alpha]],0},{0,Exp[-I
kxp[\[Epsilon],u,ky,\[Alpha]] \[Alpha]]};

mD[\[Epsilon]_,u_,ky_,\[Alpha]_] := {Exp[I
kx[\[Epsilon],u,ky,\[Alpha]] (1-\[Alpha])],0},{0,Exp[-I
kx[\[Epsilon],u,ky,\[Alpha]] (1-\[Alpha])]};

mT1[\[Epsilon]_,u_,ky_,\[Alpha]_]
:=Inverse[mA[\[Epsilon],u,ky,\[Alpha]]]
. mB[\[Epsilon],u,ky,\[Alpha]];

mT2[\[Epsilon]_,u_,ky_,\[Alpha]_]
:=Inverse[mB[\[Epsilon],u,ky,\[Alpha]]]
. mA[\[Epsilon],u,ky,\[Alpha]];

mT[\[Epsilon]_,u_,ky_,\[Alpha]_] := mD[\[Epsilon],u,ky,\[Alpha]]
. mT1[\[Epsilon],u,ky,\[Alpha]] . mC[\[Epsilon],u,ky,\[Alpha]]
. mT2[\[Epsilon],u,ky,\[Alpha]];

ans[\[Epsilon]_,u_,ky_,\[Phi]_,\[Alpha]_] :=
Det[mT[\[Epsilon],u,ky,\[Alpha]] - IdentityMatrix[2]
Exp[I \[Phi]]];

```

ans can be simplified as

```

sans[\[Epsilon]_,u_,ky_,\[Phi]_,\[Alpha]_] := Cos[\[Phi]] -
Cos[\[Alpha] kxp[\[Epsilon],u,ky,\[Alpha]]] Cos[(\[Alpha]-1)
kx[\[Epsilon],u,ky,\[Alpha]]] + ((ky^2 - (u
(\[Alpha]-1)+\[Epsilon])
(u \[Alpha]+\[Epsilon]))/(kx[\[Epsilon],u,ky,\[Alpha]]
kxp[\[Epsilon],u,ky,\[Alpha]])) Sin[(\[Alpha]-1)
kx[\[Epsilon],u,ky,\[Alpha]]] Sin[\[Alpha]
kxp[\[Epsilon],u,ky,\[Alpha]]];

```

In order to produce a surface plot, showing k_y vs ϕ for some range of energy ϵ , we devise an algorithm where by we first find an approximate root of `sans`,

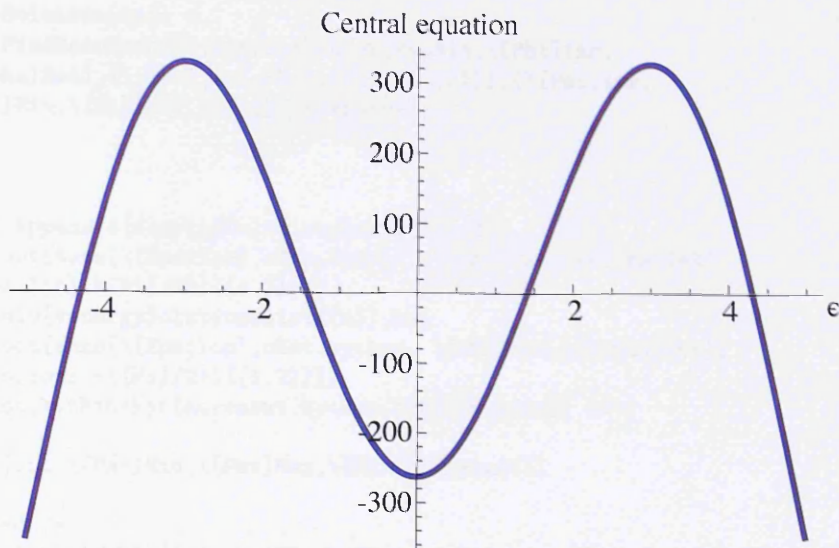


Fig. A.1: Central equation sans plotted with values $u = 10\pi$, $k_y = 16$, $\phi = 1$, and $\alpha = 1/2$ to determine the first root, approximately $\epsilon = \pi/2$.

given values for its parameters. We can then use the `FindRoot` function (Newton-Raphson iteration) to find the next root, and iterate this process for each different root as we subtly change the values of k_y and ϕ .

To find the first root, we look at the graph:

```
Plot[sans[\[Epsilon],10 \[Pi],16,1,0.5],{\[Epsilon],-5,5},PlotRange->All]
```

The roots of both the conduction and valence bands are approximately at $\epsilon = \pi/2$.

We use the following code to find all the subsequent roots, and arrange them to form a 3D surface plot:

```
uSet=10 \[Pi];
\[Alpha]Set=0.5;

kytMin=-16;
kytMax=16;
kytIncrement=1/10;

\[Phi]Min=-1;
\[Phi]Max=1;
\[Phi]Increment=1/10;

cenergySolutionsList =
Table[{FindRoot[sans[\[Epsilon],uSet,kytMin,\[Phi]inc,\[Alpha]Set],
  {\[Epsilon],\[Pi]/2}][[1,2]],{\[Phi]inc,
  \[Phi]Min,\[Phi]Max,\[Phi]Increment}};
```

```

venergySolutionsList =
Table[{FindRoot[sans[\[Epsilon],uSet,kytMin,\[Phi]inc,
\[Alpha]Set],{\[Epsilon],-\[Pi]/2}][[1,2]]},{\[Phi]inc,
\[Phi]Min,\[Phi]Max,\[Phi]Increment}];

n=1;

Do[Do[{ AppendTo[cenergySolutionsList[[n]],Re[
FindRoot[sans[\[Epsilon],uSet,kytinc, \[Phi]inc,\[Alpha]Set],
{\[Epsilon],\[Pi]/2}][[1,2]]}],
AppendTo[venergySolutionsList[[n]],Re[
FindRoot[sans[\[Epsilon],uSet,kytinc, \[Phi]inc,\[Alpha]Set],
{\[Epsilon],-\[Pi]/2}][[1,2]]]
}],{kytinc,kytMin+kytIncrement,kytMax,kytIncrement}] n++;

, {\[Phi]inc,\[Phi]Min,\[Phi]Max,\[Phi]Increment}]

ckytCoords =
Flatten[Table[Table[i,{i,kytMin,kytMax,kytIncrement}],
{Length[cenergySolutionsList]}]];

vkytCoords =
Flatten[Table[Table[i,{i,kytMin,kytMax,kytIncrement}],
{Length[venergySolutionsList]}]];

c\[Phi]Coords =
Flatten[Table[i,{i,\[Phi]Min,\[Phi]Max,\[Phi]Increment},
{Length[cenergySolutionsList][[1]]}]];

v\[Phi]Coords =
Flatten[Table[i,{i,\[Phi]Min,\[Phi]Max,\[Phi]Increment},
{Length[venergySolutionsList][[1]]}]];

ccombinedCoords =
Table[{ckytCoords[[j]],c\[Phi]Coords[[j]],Flatten[
N[cenergySolutionsList][[j]]},{j,1,Length[Flatten[cenergySolutionsList]]}]];

vcombinedCoords =
Table[{vkytCoords[[j]],v\[Phi]Coords[[j]],Flatten[
N[venergySolutionsList][[j]]},{j,1,Length[Flatten[venergySolutionsList]]}]];

ListPlot3D[{vcombinedCoords,ccombinedCoords},AxesLabel->{ky,\[Phi],\[Epsilon]}]

```

Bilayer Graphene

The energy surfaces for work in Section 3.3 were plotted using the following Python code. It uses selected functions from the numpy and scipy libraries, and is compiled to a C program using Cython.

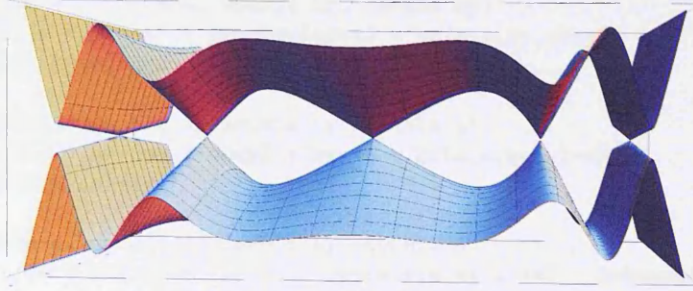


Fig. A.2: Valence and conduction bands of the spectrum of a superlattice with square barriers in monolayer graphene; $u = 10\pi$, $\alpha = 1/2$. Values used to match Barbier et al. [19, Fig. 2].

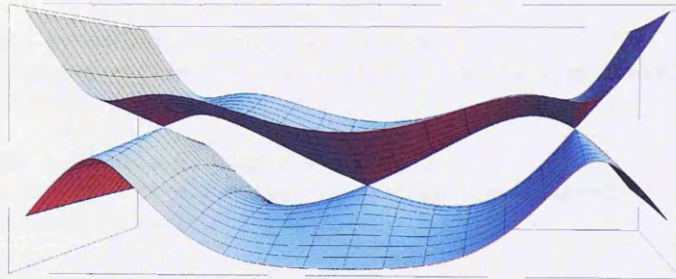


Fig. A.3: Valence and conduction bands of the spectrum of a superlattice with square barriers in monolayer graphene; $u = 6\pi$, $\alpha = 4/10$. Values used to match Barbier et al. [19, Fig. 3].

```

import cmath as c
from numpy import matrix, identity, diag, pi, arange
from scipy.linalg import det, inv
from scipy.optimize import brentq
import time, io
cdef extern from "math.h":
    double pow(double, int)

def utilda(double potential, double period):
    return (potential * pow(10,-3) * 1.6 * pow(10,-19)) / (((1.05 * \
    pow(10,-34))**2) / (2 * 0.035 * 9.11 * pow(10,-31) * (period * \
    pow(10,-9))**2))

def kx(double e, double u, double ky, double a):
    return c.sqrt(-ky**2 + u * a + e)

def kappa(double e, double u, double ky, double a):
    return c.sqrt(ky**2 + u * a + e)

def kxp(double e, double u, double ky, double a):
    return - c.sqrt(-ky**2 + u * (1-a) - e)

def kappap(double e, double u, double ky, double a):
    return - c.sqrt(ky**2 + u * (1-a) - e)

```

```

def a12(double e, double u, double ky, double a):
    return 1/(e + u * a) * complex(ky**2 - kx(e,u,ky,a)**2, \
    - 2*kx(e,u,ky,a)*ky)

def a22(double e, double u, double ky, double a):
    return 1/(e + u * a) * complex(ky**2 - kx(e,u,ky,a)**2, \
    + 2*kx(e,u,ky,a)*ky)

def a32(double e, double u, double ky, double a):
    return 1/(e + u * a) * (ky**2 + kappa(e,u,ky,a)**2 - 2*kappa(e,u,ky,a)*ky)

def a42(double e, double u, double ky, double a):
    return 1/(e + u * a) * (ky**2 + kappa(e,u,ky,a)**2 + 2*kappa(e,u,ky,a)*ky)

def b12(double e, double u, double ky, double a):
    return 1/(e - u * (1-a)) * complex(ky**2 - kxp(e,u,ky,a)**2, - \
    2*kxp(e,u,ky,a)*ky)

def b22(double e, double u, double ky, double a):
    return 1/(e - u * (1-a)) * complex(ky**2 - kxp(e,u,ky,a)**2, + \
    2*kxp(e,u,ky,a)*ky)

def b32(double e, double u, double ky, double a):
    return 1/(e - u * (1-a)) * (ky**2 + kappap(e,u,ky,a)**2 -
    2*kappap(e,u,ky,a)*ky)

def b42(double e, double u, double ky, double a):
    return 1/(e - u * (1-a)) * (ky**2 + kappap(e,u,ky,a)**2 +
    2*kappap(e,u,ky,a)*ky)

def matrixA(double e, double u, double ky, double a):
    return matrix([ \
        [1, 1, 1, 1], \
        [a12(e, u, ky, a), a22(e, u, ky, a), a32(e, u, ky, a), \
        a42(e, u, ky, a)], \
        [complex(0, kx(e, u, ky, a)), \
        - complex(0, kx(e, u, ky, a)), kappa(e, u, ky, a), \
        - kappa(e, u, ky, a)], \
        [complex(0, kx(e, u, ky, a) * a12(e, u, ky, a)), \
        - complex(0, kx(e, u, ky, a) * a22(e, u, ky, a)), \
        kappa(e, u, ky, a) * a32(e, u, ky, a), \
        -kappa(e, u, ky, a) * a42(e, u, ky, a)]]])

def matrixB(double e, double u, double ky, double a):
    return matrix([ \
        [1, 1, 1, 1], \
        [b12(e, u, ky, a), b22(e, u, ky, a), b32(e, u, ky, a), \
        b42(e, u, ky, a)], \
        [complex(0, kxp(e, u, ky, a)), \
        - complex(0, kxp(e, u, ky, a)), kappap(e, u, ky, a), \
        - kappap(e, u, ky, a)], \
        [complex(0, kxp(e, u, ky, a) * b12(e, u, ky, a)), \
        - complex(0, kxp(e, u, ky, a) * b22(e, u, ky, a)), \
        kappap(e, u, ky, a) * b32(e, u, ky, a), \
        -kappap(e, u, ky, a) * b42(e, u, ky, a)]]])

```

```

def matrixC(double e, double u, double ky, double a):
    return diag([c.exp(complex(0, kxp(e, u, ky, a) * a)), \
                 c.exp(- complex(0, kxp(e, u, ky, a) * a)), \
                 c.exp(kappap(e, u, ky, a) * a), \
                 c.exp(- kappap(e, u, ky, a) * a)])

def matrixD(double e, double u, double ky, double a):
    return diag([c.exp(complex(0, kx(e, u, ky, a) * (1-a))), \
                 c.exp(- complex(0, kx(e, u, ky, a) * (1-a))), \
                 c.exp(kappa(e, u, ky, a) * (1-a)), \
                 c.exp(- kappa(e, u, ky, a) * (1-a))])

def matrixT1(double e, double u, double ky, double a):
    try:
        return inv(matrixA(e, u, ky, a) * matrixB(e, u, ky, a))
    except:
        raise ValueError('singular matrix A')

def matrixT2(double e, double u, double ky, double a):
    try:
        return inv(matrixB(e, u, ky, a) * matrixA(e, u, ky, a))
    except:
        raise ValueError('singular matrix B')

def matrixT(double e, double u, double ky, double a):
    return matrixD(e, u, ky, a) * matrixT1(e, u, ky, a) *
           matrixC(e, u, ky, a) * matrixT2(e, u, ky, a)

def ans(double e, double u, double ky, double phi, double a):
    return det(matrixT(e, u, ky, a) - matrix(identity(4) *
        c.exp(complex(0, phi))))).real

def find_root_2D():
    cdef double ky_min = -4
    cdef double ky_max = 4
    cdef double ky_inc = 0.5
    cdef double potential = utilda(100, 20)
    cdef double phi = 0
    cdef double alpha = 0.5
    cdef double energy_min = 0
    cdef double energy_max = 22
    t_1 = time.time()
    output = ""
    for ky in arange(ky_min, ky_max + ky_inc, ky_inc):
        root = brentq(ans, energy_min, energy_max, \
            args=(potential, ky, phi, alpha))
        output += "{" + '{0},{1}'.format(ky, root) + "},"
    print 'time taken: {0:.2f}s'.format(time.time()-t_1)
    #[:-1] removes the last comma that is illegal syntax in Mathematica
    with open('output-2D', 'w') as file:
        file.write("{0} + output[:-1] + "}")

def find_root_3D(double energy_min=0, double energy_max=20, \
    output_file_name='output-3D'):
    cdef double ky_min = -2
    cdef double ky_max = 2
    cdef double ky_inc = 0.1
    cdef double phi_min = -3

```

```

cdef double phi_max = 3
cdef double phi_inc = 0.1
cdef double potential = utilda(100, 20)
cdef double alpha = 0.5
t_1 = time.time()
output = ""
for phi in arange(phi_min, phi_max + phi_inc, phi_inc):
    for ky in arange(ky_min, ky_max + ky_inc, ky_inc):
        root = brentq(ans, energy_min, energy_max,
                    args=(potential, ky, phi, alpha))
        output += "{" + '{0},{1},{2}'.format(ky, phi, root) + "},"
print 'time taken: {0:.2f}s'.format(time.time()-t_1)
#[:-1] removes the last comma that is illegal syntax in Mathematica
with open(output_file_name, 'w') as file:
    file.write("{0} + output[:-1] + "}")

```

Once compiled using Cython to `c_bilayer.so`, the following python code will use it with given parameters to output numerical data in a format acceptable to Mathematica:

```

from c_bilayer import *

try:

    test_alpha = 0.5
    test_potential = utilda(100,20)
    test_ky = 3
    test_phi = 3

    find_root_3D_newton(energy_start = 20,
                       ky_min = -test_ky,
                       ky_max = test_ky,
                       phi_min = -test_phi,
                       phi_max = test_phi,
                       alpha = test_alpha,
                       potential = test_potential,
                       output_file_name = "output-3D-higher")

    find_root_3D_newton(energy_start = 22,
                       ky_min = -test_ky,
                       ky_max = test_ky,
                       phi_min = -test_phi,
                       phi_max = test_phi,
                       alpha = test_alpha,
                       potential = test_potential,
                       output_file_name = "output-3D-higher2")

except:
    raise ValueError("Newton method didn't work")

```

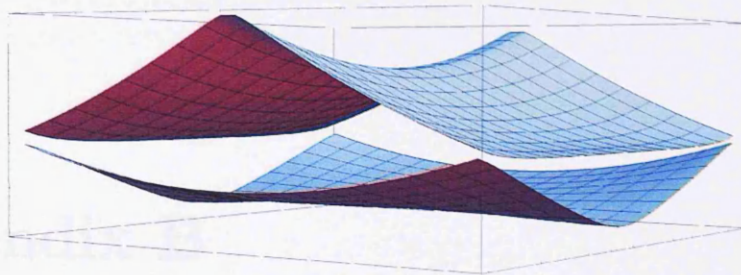


Fig. A.4: The first two conduction bands of the spectrum of a superlattice with square barriers in bilayer graphene; $\bar{u} = 37.02$ (corresponding to 100 meV, $l = 20$ nm), and $\alpha = 1/2$. Values used to match Barbier et al. [20, Fig. 6(1)].

Mathematica then reads the contained data to create plots:

```
PythonOutputFile3Dhigher2 = OpenRead["output-3D-higher2"];
PythonOutput3Dhigher2=Read[PythonOutputFile3Dhigher2];
Close[PythonOutputFile3Dhigher2];
```

```
PythonOutputFile3Dhigher =
OpenRead["output-3D-higher"];
PythonOutput3Dhigher=Read[PythonOutputFile3Dhigher];
Close[PythonOutputFile3Dhigher];
```

```
ListPlot3D[{PythonOutput3Dhigher, PythonOutput3Dhigher2(*,
  PythonOutput3Dlower,PythonOutput3Dlower2*)},
  AxesLabel -> {ky, \[Phi], \[Epsilon]}
```

Appendix B

Source Code for Rendering Moiré Images

The following Mathematica code was used to create the hexagonal lattices when analysing Moiré patterns in Chapter 4. As well as the code, example usage is given.

```
(* Setup lattice *)

a[l_] := 1 Sqrt[3];
b[l_] := 1/2;
c[l_] := 1 Sqrt[3]/2;
d[l_] := 2 l;

bondLinePoints[x_, y_,
  l_] := {{x, y}, {x + c[l], y + b[l]}, {x + c[l], y + 1 + b[l]}, {x,
  y + d[l]}, {x - c[l], y + 1 + b[l]}, {x - c[l], y + b[l]}, {x,
  y}};
sublatticeAPoints[x_, y_,
  l_] := {{x + c[l], y + b[l]}, {x, y + d[l]}, {x - c[l],
  y + b[l]}}; (* {{x+c[l],y+b[l]},{x,y+d[l]},{x-c[l],y+b[l]}} *)

sublatticeBPoints[x_, y_,
  l_] := {{x, y}, {x + c[l], y + 1 + b[l]}, {x - c[l], y + 1 + b[l]}};

(* Not required but useful to check graphs, maybe *)

noOfHexagonsGammaPrimeStretch[\[Delta]_] := 1/\[Delta];
noOfHexagonsSupercellStretch[\[Delta]_] := 1/\[Delta]^2;

ap[a_, \[Delta]_, \[Theta]_] := -((a^2 (-1 + \[Delta]))/Sqrt[
  a^2 (2 + (-2 + \[Delta]) \[Delta] +
  2 (-1 + \[Delta]) Cos[\[Degree] \[Theta]])]);
```

```

\[Phi]p[\[Delta]_, \[Theta]_] :=
  ArcCot[(-1 + \[Delta] +
    Cos[\[Degree] \[Theta]]) Csc[\[Degree] \[Theta]]];

(* Tables of points for lines and atom sites, two each for odd and \
even rows of hexagons *)

collectedbondLinePoints[l_, horizontalHexagons_, verticalHexagons_,
  xOffset_, yOffset_] :=
  Table[bondLinePoints[i a[l] + xOffset, j (d[l] + 1) + yOffset,
    l], {i, 0, horizontalHexagons - 1}, {j, 0,
    verticalHexagons/2 - 1}];
collectedbondLinePoints2[l_, horizontalHexagons_, verticalHexagons_,
  xOffset_, yOffset_] :=
  Table[bondLinePoints[i a[l] + c[l] + xOffset,
    j (d[l] + 1) + b[l] + 1 + yOffset, l], {i, 0,
    horizontalHexagons - 1}, {j, 0, verticalHexagons/2 - 1}];

collectedsublatticeAPoints[l_, horizontalHexagons_, verticalHexagons_,
  xOffset_, yOffset_] :=
  Partition[
    Flatten[Table[
      sublatticeAPoints[i a[l] + xOffset, j (d[l] + 1) + yOffset,
        l], {i, 0, horizontalHexagons - 1}, {j, 0,
        verticalHexagons/2 - 1}]], 2];
collectedsublatticeAPoints2[l_, horizontalHexagons_,
  verticalHexagons_, xOffset_, yOffset_] :=
  Partition[
    Flatten[Table[
      sublatticeAPoints[i a[l] + c[l] + xOffset,
        j (d[l] + 1) + b[l] + 1 + yOffset, l], {i, 0,
        horizontalHexagons - 1}, {j, 0, verticalHexagons/2 - 1}]], 2];

collectedsublatticeBPoints[l_, horizontalHexagons_, verticalHexagons_,
  xOffset_, yOffset_] :=
  Partition[
    Flatten[Table[
      sublatticeBPoints[i a[l] + xOffset, j (d[l] + 1) + yOffset,
        l], {i, 0, horizontalHexagons - 1}, {j, 0,
        verticalHexagons/2 - 1}]], 2];
collectedsublatticeBPoints2[l_, horizontalHexagons_,
  verticalHexagons_, xOffset_, yOffset_] :=
  Partition[
    Flatten[Table[
      sublatticeBPoints[i a[l] + c[l] + xOffset,
        j (d[l] + 1) + b[l] + 1 + yOffset, l], {i, 0,
        horizontalHexagons - 1}, {j, 0, verticalHexagons/2 - 1}]], 2];

(* Join the two sets of points for the lines and atom sites *)

unionBondLinePoints[l_, horizontalHexagons_, verticalHexagons_,
  xOffset_, yOffset_] :=
  Union[collectedbondLinePoints[l, horizontalHexagons,
    verticalHexagons, xOffset, yOffset],
    collectedbondLinePoints2[l, horizontalHexagons, verticalHexagons,
    xOffset, yOffset]]

```

```

unionSublatticeAPoints[l_, \[Theta]_, horizontalHexagons_,
  verticalHexagons_, xOffset_, yOffset_] :=
doRotation[\[Theta], #] & /@
  Union[collectedsublatticeAPoints[l, horizontalHexagons,
    verticalHexagons, xOffset, yOffset],
    collectedsublatticeAPoints2[l, horizontalHexagons,
      verticalHexagons, xOffset, yOffset]];

unionSublatticeBPoints[l_, \[Theta]_, horizontalHexagons_,
  verticalHexagons_, xOffset_, yOffset_] :=
doRotation[\[Theta], #] & /@
  Union[collectedsublatticeBPoints[l, horizontalHexagons,
    verticalHexagons, xOffset, yOffset],
    collectedsublatticeBPoints2[l, horizontalHexagons,
      verticalHexagons, xOffset, yOffset]];

(* Graphics *)

graphBondLines[l_, \[Theta]_, horizontalHexagons_, verticalHexagons_,
  bondColor_, bondStyle_, xOffset_, yOffset_, opacity_] :=
Graphics[
  Rotate[{Opacity[opacity], bondStyle, bondColor,
    Line /@ unionBondLinePoints[l, horizontalHexagons,
      verticalHexagons, xOffset, yOffset]}, \[Theta] \[Degree], {0,
    0}]];

graphSublatticeAPoints[l_, \[Theta]_, horizontalHexagons_,
  verticalHexagons_, atomSize_, sublatticeAColor_, xOffset_,
  yOffset_, onlyPointsOnSites_, threshold_, pointsOnSites1_,
  points\[Theta]_, gColorA_, gColorB_, opacity_] :=
If [onlyPointsOnSites,
  Graphics[{Opacity[opacity], PointSize[atomSize],
    isPointOverSiteQVWithColor[#, threshold, pointsOnSites1,
      points\[Theta], gColorA, gColorB] & /@
      unionSublatticeAPoints[l, \[Theta], horizontalHexagons,
        verticalHexagons, xOffset, yOffset]}],
  Graphics[{Opacity[opacity], PointSize[atomSize],
    unionSublatticeAPointsWithColor[l, \[Theta], horizontalHexagons,
      verticalHexagons, xOffset, yOffset, sublatticeAColor]}]];

graphSublatticeBPoints[l_, \[Theta]_, horizontalHexagons_,
  verticalHexagons_, atomSize_, sublatticeBColor_, xOffset_,
  yOffset_, onlyPointsOnSites_, threshold_, pointsOnSites1_,
  points\[Theta]_, gColorA_, gColorB_, opacity_] :=
If [onlyPointsOnSites,
  Graphics[{Opacity[opacity], PointSize[atomSize],
    isPointOverSiteQVWithColor[#, threshold, pointsOnSites1,
      points\[Theta], gColorA, gColorB] & /@
      unionSublatticeBPoints[l, \[Theta], horizontalHexagons,
        verticalHexagons, xOffset, yOffset]}],
  Graphics[{Opacity[opacity], PointSize[atomSize],
    unionSublatticeBPointsWithColor[l, \[Theta], horizontalHexagons,
      verticalHexagons, xOffset, yOffset, sublatticeBColor]}]];

graphLayer[l_, \[Theta]_, horizontalHexagons_, verticalHexagons_,
  bondColor_, bondStyle_, sublatticeAColor_, sublatticeBColor_,
  atomSize_, xOffset_, yOffset_, onlyPointsOnSites_, threshold_,
  pointsOnSites1_, points\[Theta]_, gColorA_, gColorB_, bondOpacity_,

```

```

    sublatticeAOpacity_, sublatticeBOpacity_] := Show[
graphBondLines[l, \[Theta], horizontalHexagons, verticalHexagons,
bondColor, bondStyle, xOffset, yOffset, bondOpacity],
graphSublatticeAPoints[l, \[Theta], horizontalHexagons,
verticalHexagons, atomSize, sublatticeAColor, xOffset, yOffset,
onlyPointsOnSites, threshold, pointsOnSites1, points\[Theta],
gColorA, gColorB, sublatticeAOpacity],
graphSublatticeBPoints[l, \[Theta], horizontalHexagons,
verticalHexagons, atomSize, sublatticeBColor, xOffset, yOffset,
onlyPointsOnSites, threshold, pointsOnSites1, points\[Theta],
gColorA, gColorB, sublatticeBOpacity]];

(* Test if an atom is near a lattice site *)

isNearlyIntegerQ[x_, threshold_] :=
If[Abs[Round[x] - x] < threshold, True, False];

solveForAlphaBetaSiteA[point_, l_, \[Theta]_] :=
Solve[(point + {0,
1}) == \[Alpha] rotationMatrix\[Theta] . {-c[l],
1 + b[l]} + \[Beta] rotationMatrix\[Theta] . {c[l],
1 + b[l]}, {\[Alpha], \[Beta]}];
solveForAlphaBetaSiteB[point_, l_, \[Theta]_] :=
Solve[point == \[Alpha] rotationMatrix\[Theta] . {-c[l],
1 + b[l]} + \[Beta] rotationMatrix\[Theta] . {c[l],
1 + b[l]}, {\[Alpha], \[Beta]}];

isPointOverSiteQ[point_, threshold_, l_, \[Theta]_] :=
If[
Or[
And[isNearlyIntegerQ[
solveForAlphaBetaSiteA[point, l, \[Theta]][[1, 1, 2]],
threshold],
isNearlyIntegerQ[
solveForAlphaBetaSiteA[point, l, \[Theta]][[1, 2, 2]],
threshold]],
And[isNearlyIntegerQ[
solveForAlphaBetaSiteB[point, l, \[Theta]][[1, 1, 2]],
threshold],
isNearlyIntegerQ[
solveForAlphaBetaSiteB[point, l, \[Theta]][[1, 2, 2]],
threshold]]],
point, {0, 0}];

isPointOverSiteQV[point_, threshold_, l_, \[Theta]_] :=
Block[{
\[Alpha]A = solveForAlphaBetaSiteA[point, l, \[Theta]][[1, 1, 2]],
\[Beta]A =
solveForAlphaBetaSiteA[point, l, \[Theta]][[1, 2, 2]],
rA = ((\[Alpha]A -
Round\[Alpha]A) rotationMatrix\[Theta] . {-c[l],
1 + b[l]} + (\[Beta]A -
Round\[Beta]A) rotationMatrix\[Theta] . {c[l],
1 + b[l]}),
\[Alpha]B = solveForAlphaBetaSiteB[point, l, \[Theta]][[1, 1, 2]],
\[Beta]B =
solveForAlphaBetaSiteB[point, l, \[Theta]][[1, 2, 2]],
rB = ((\[Alpha]B -

```

```

Round[\[Alpha]B]) rotationMatrix[\[Theta]] . {-c[1],
1 + b[1]} + (\[Beta]B -
Round[\[Beta]B]) rotationMatrix[\[Theta]] . {c[1],
1 + b[1]}}),
If[
Or[
isNearlyIntegerQV[Sqrt[rA . rA], threshold],
isNearlyIntegerQV[Sqrt[rB . rB], threshold]], point, {0, 0}];
isNearlyIntegerQV[r_, threshold_] := If[r < threshold, True, False];

(* Rotation *)

rotationMatrix[\[Theta]_] := {{Cos[\[Theta] \[Degree]], -Sin[\[Theta] \
\[Degree]]}, {Sin[\[Theta] \[Degree]], Cos[\[Theta] \[Degree]]}};
doRotation[\[Theta]_, point_] := rotationMatrix[\[Theta]] . point;

(* Color selection (A and B graphene sublattices *)

unionSublatticeAPointsWithColor[l_, \[Theta]_, horizontalHexagons_,
verticalHexagons_, xOffset_, yOffset_, pointColor_] :=
colorEachPoint[#, pointColor] & /@
unionSublatticeAPoints[l, \[Theta], horizontalHexagons,
verticalHexagons, xOffset, yOffset];

unionSublatticeBPointsWithColor[l_, \[Theta]_, horizontalHexagons_,
verticalHexagons_, xOffset_, yOffset_, pointColor_] :=
colorEachPoint[#, pointColor] & /@
unionSublatticeBPoints[l, \[Theta], horizontalHexagons,
verticalHexagons, xOffset, yOffset];

colorEachPoint[point_, color_] :=
Point[{point}, VertexColors -> {color}];

isPointOverSiteQVWithColor[point_, threshold_, l_, \[Theta]_,
gColorA_, gColorB_] :=
Block[{
\[Alpha]A = solveForAlphaBetaSiteA[point, l, \[Theta]][[1, 1, 2]],
\[Beta]A =
solveForAlphaBetaSiteA[point, l, \[Theta]][[1, 2, 2]],
rA = ((\[Alpha]A -
Round[\[Alpha]A]) rotationMatrix[\[Theta]] . {-c[1],
1 + b[1]} + (\[Beta]A -
Round[\[Beta]A]) rotationMatrix[\[Theta]] . {c[1],
1 + b[1]}),
\[Alpha]B = solveForAlphaBetaSiteB[point, l, \[Theta]][[1, 1, 2]],
\[Beta]B =
solveForAlphaBetaSiteB[point, l, \[Theta]][[1, 2, 2]],
rB = ((\[Alpha]B -
Round[\[Alpha]B]) rotationMatrix[\[Theta]] . {-c[1],
1 + b[1]} + (\[Beta]B -
Round[\[Beta]B]) rotationMatrix[\[Theta]] . {c[1],
1 + b[1]}),

```

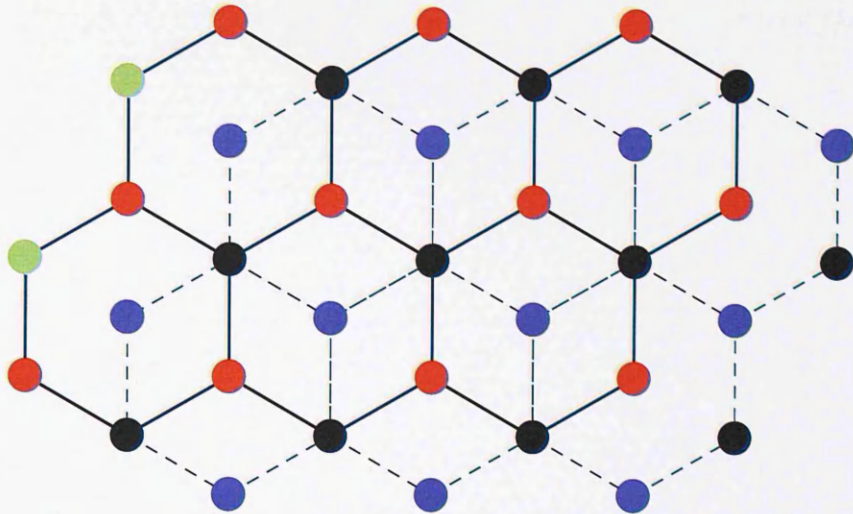


Fig. B.1: Schematic of the bilayer graphene lattice with Bernal stacking. The bonds in the top (bottom) layer are indicated by dashed (solid) lines. Sublattice A (B) sites in the bottom layer are coloured red (green). The top layer sublattice A (B) sites are black (blue).

```
Which[
  isNearlyIntegerQV[Sqrt[rA . rA], threshold],
  colorEachPoint[point, gColorA],
  isNearlyIntegerQV[Sqrt[rB . rB], threshold],
  colorEachPoint[point, gColorB],
  True, colorEachPoint[{0, 0}, Transparent]
];
```

The main function to be called is `graphLayer`, which admits several parameters, detailed in Table B.1.

Example Usage

Bilayer Graphene

A schematic of the bilayer graphene lattice is drawn to correlate with McCann and Fal'ko [7, Fig. 1].

```
Show[
  graphLayer[1, 0, 3, 3, Black, AbsoluteThickness[1], Red, Green, 0.04,
    0, 0, False, 1, 1, 0, Red, Blue, 1, 1, 1],
  graphLayer[1, 0, 3, 3, Black, Dashed, Black, Blue, 0.04,
    a[1]/2, -1/2, False, 1, 1, 0, Red, Blue, 1, 1, 1]]
```

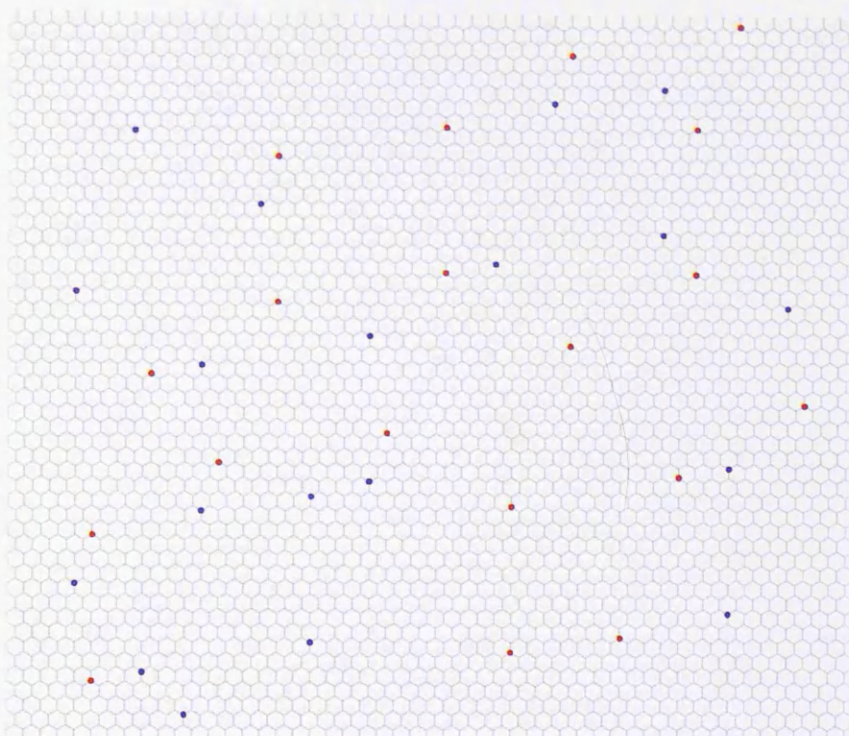


Fig. B.2: Model of a 50x50 graphene layer with hBN below, rotated at an angle of 10° . Only graphene sites that are almost directly above boron or nitrogen sites are shown, coloured red (blue) for graphene sublattice A (B).

Graphene on hBN: Here we model a 50x50 graphene layer with hBN below, rotated at an angle of 10° . Only graphene sites that are almost directly above boron or nitrogen sites are shown, coloured red (blue) for graphene sublattice A (B). See Fig. B.2.

```
Show[graphLayer[1, 0, 50, 50, Black, AbsoluteThickness[1],
  Transparent, Transparent, 0.018, 0, 0, False, 1, 1, 0, Red, Blue,
  0.1, 1, 1],
graphLayer[1.01626, 10, 50, 50, Transparent, AbsoluteThickness[1],
  Transparent, Blue, 0.006, 0, 0, True, 0.06, 1, 0, Red, Blue, 0.1, 1,
  1]]
```

G/hBN/hBN, low-level graphics, only nitrogen sites: Here, to aid with speed of computation we use `graphSublatticeBPoints` directly, drawing a graphene lattice with two layers of boron nitride on top. The first is rotated at an angle of 5° , while the latter is rotated by 10° . Only those graphene sites which are almost directly above a nitrogen atom are shown. (Here, we define the nitrogen sublattice

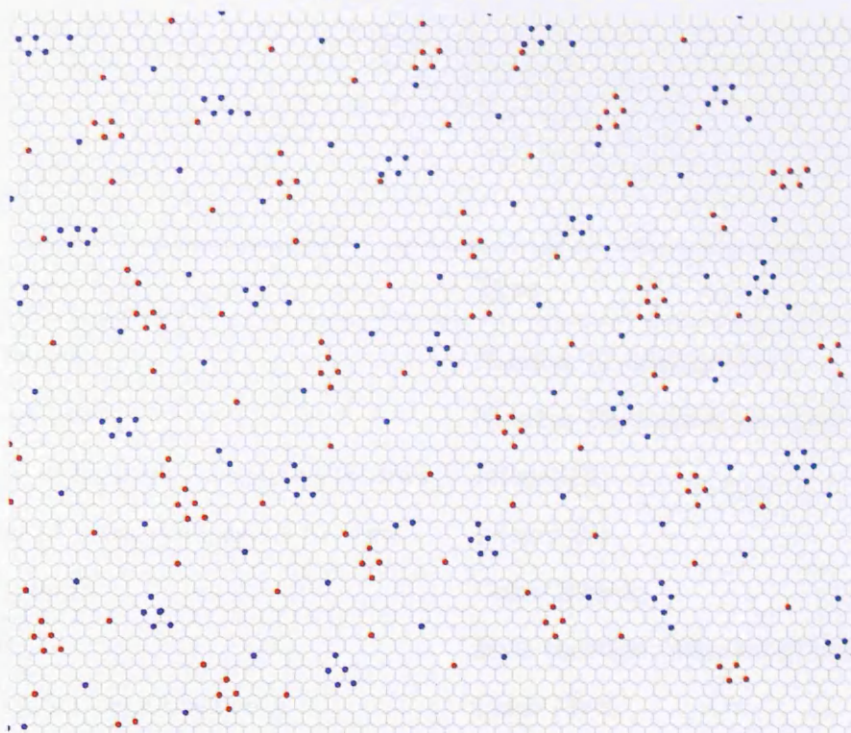


Fig. B.3: Model of monolayer graphene below two layers of hBN, the first rotated by 5° relative to graphene, the second by 10° . Only graphene sites almost directly below a nitrogen site are drawn: sublattice A (B) in red (blue).

to be B.) The graphene bonds have an opacity of 0.1 to highlight the nitrogen atoms. See Fig. B.3.

```
Show[
  graphBondLines[2.46/Sqrt[3], 0, 100, 100, Black,
    AbsoluteThickness[1], 0, 0, 0.1],
  graphSublatticeBPoints[2.50/Sqrt[3], 5, 100, 100, 0.002, Blue, 0, 0,
    True, 2.46/(6 Sqrt[3]), 2.46/Sqrt[3], 0, Red, Blue, 1],
  graphSublatticeBPoints[2.50/Sqrt[3], 10, 100, 100, 0.002, Blue, 0, 0,
    True, 2.46/(6 Sqrt[3]), 2.46/Sqrt[3], 0, Red, Blue, 1]
]
```

Parameter	Type
Bond length	Number (2.46/Sqrt[3])
Angle of layer	Number (0; degrees, no symbol)
Number of horizontal hexagons to draw	Integer (5)
Number of vertical hexagons to draw	Integer (5)
Bond colour	Color (Black)
Bond style	Style function (AbsoluteThickness[1])
Atom colour on sublattice A	Color (Red)
Atom colour on sublattice B	Color (Blue)
Size of atoms	Number (0.04)
Offset of layer in x direction	Number (0)
Offset of layer in y direction	Number (0)
Nearly commensurate atoms only	Boolean (False)
Commensurability threshold	Number (2.46/(6 Sqrt[3]))
Bond length of other layer	Number (2.46/Sqrt[3])
Angle of other layer	Number (0)
Commensurate atom colour sublattice A	Color (Red)
Commensurate atom colour sublattice B	Color (Blue)
Opacity of bonds	Number (1)
Opacity of atoms on sublattice A	Number (1)
Opacity of atoms on sublattice B	Number (1)

Table B.1: Formal parameters (with example values) of `graphLayer`.

Appendix C

Full Derivation of Pseudospin in Bilayer Graphene

The calculation of pseudospin for a low energy bilayer graphene system (Section 1.4.1) shows that it has a phase twice that of momentum:

$$\langle \boldsymbol{\sigma} \rangle = \cos 2\phi \mathbf{i} + \sin 2\phi \mathbf{j}. \quad (\text{C.1})$$

If we introduce an asymmetry in the on-site energies between the two layers, we can write a low energy effective Schrödinger equation as

$$\begin{pmatrix} -\epsilon + \frac{\Delta}{2} & \frac{p^2}{2m} e^{-2i\phi} \\ \frac{p^2}{2m} e^{2i\phi} & -\epsilon - \frac{\Delta}{2} \end{pmatrix} = 0, \quad (\text{C.2})$$

where sites in layer one (two) have an on-site energy of $\Delta/2$ ($-\Delta/2$), thus

$$\epsilon = \pm \frac{1}{2} \sqrt{\frac{p^4}{m^2} + \Delta^2}. \quad (\text{C.3})$$

Eqn. C.2 can be written as a pair of simultaneous equations (where $\Phi = (\Phi_x, \Phi_y)$),

$$\frac{\Delta}{2}\Phi_x + \frac{p^2}{2m}e^{-2i\phi}\Phi_y = \epsilon\Phi_x, \quad (\text{C.4})$$

$$\frac{p^2}{2m}e^{2i\phi}\Phi_x - \frac{\Delta}{2}\Phi_y = \epsilon\Phi_y. \quad (\text{C.5})$$

Substituting $p^2/2m = \pm\sqrt{\epsilon^2 - \Delta^2/4}$ in Eqn. C.5 results in

$$\begin{aligned} \pm\sqrt{\epsilon^2 - \frac{\Delta^2}{4}}e^{i\phi}\Phi_x &= \left(\epsilon + \frac{\Delta}{2}\right)e^{-i\phi}\Phi_y \\ \pm\sqrt{1 - \frac{\Delta^2}{4\epsilon^2}}e^{i\phi}\Phi_x &= \left(1 + \frac{\Delta}{2\epsilon}\right)e^{-i\phi}\Phi_y \\ \pm\sqrt{1 - \zeta^2}e^{i\phi}\Phi_x &= (1 + \zeta)e^{-i\phi}\Phi_y \\ \pm\sqrt{1 - \zeta}e^{i\phi}\Phi_x &= \sqrt{1 + \zeta}e^{-i\phi}\Phi_y, \end{aligned} \quad (\text{C.6})$$

where $\zeta = \Delta/2\epsilon$. Assuming both sides equal unity, we find that

$$\Phi = c \begin{pmatrix} \pm \frac{e^{-i\phi}}{\sqrt{1-\zeta}} \\ \frac{e^{i\phi}}{\sqrt{1+\zeta}} \end{pmatrix}, \quad (\text{C.7})$$

where c is a constant to be determined. By enforcing the normalisation condition $\langle\Phi|\Phi\rangle = 1$, we see that

$$\Phi = \frac{1}{\sqrt{2}} \begin{pmatrix} \pm\sqrt{1+\zeta}e^{-i\phi} \\ \sqrt{1-\zeta}e^{i\phi} \end{pmatrix}. \quad (\text{C.8})$$

The pseudospin is then found to be

$$\langle\sigma\rangle_{\pm} = \pm\sqrt{1 - \zeta^2}(\cos 2\phi\mathbf{i} + \sin 2\phi\mathbf{j}) + \zeta\mathbf{k}, \quad (\text{C.9})$$

where $\langle\sigma\rangle_+$ ($\langle\sigma\rangle_-$) denotes pseudospin in the conduction (valence) band. A change of sign of Δ in Eqn. C.2 implies ζ also changes sign. This result was developed and exploited in San-Jose et al. [116], and is of interest due to the out of plane

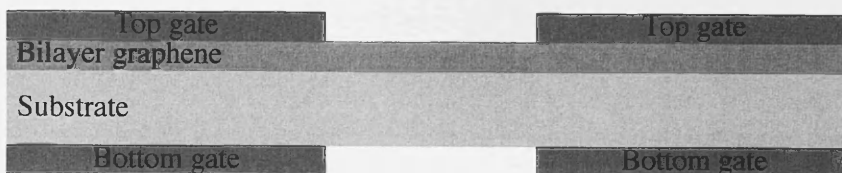


Fig. C.1: Schematics showing graphene bilayer in plane on a substrate (e.g., SiO_2). Top and bottom gates are configured to independently vary the Fermi energy and the size of Δ . The gates can be separated by an in-plane distance of 10–100 nm.

component. At $\epsilon = \pm\Delta/2$ (the minima and maxima of the low energy bands in the energy spectrum with an induced gap) the in-plane pseudospin components vanish: we are left with the out of plane component only. It may be interesting to see what happens as the gap is varied along the length of the substrate of bilayer graphene, using the schematics in Fig. C.1.

With such a device, Δ could be modulated by electrostatic gates to have smoothly varying pseudospin (on the scale of the lattice constant). This structure would increase the resistivity of the system by acting as a spin valve. Such a device would work as pseudospin from one side of the barrier would prefer to tunnel through if the pseudospin on the other side of the barrier was polarized in the same direction. If the directions of pseudospin differ, resistivity would increase. A structure with two or more of these profiles sequentially produced would have an even greater effect on the conductivity of the sample. This is analogous to the giant magneto-resistance (GMR) effect.

Bibliography

- [1] KS Novoselov, AK Geim, SV Morozov, D Jiang, MI Katsnelson, IV Grigorieva, SV Dubonos, and AA Firsov. Two-dimensional gas of massless Dirac fermions in graphene. *Nature*, **438**(7065):197–200, 2005.
- [2] KS Novoselov, AK Geim, SV Morozov, D Jiang, Y Zhang, SV Dubonos, IV Grigorieva, and AA Firsov. Electric field effect in atomically thin carbon films. *Science*, **306**(5696):666–669, 2004.
- [3] AK Geim and KS Novoselov. The rise of graphene. *Nature Materials*, **6**(3):183–191, 2007.
- [4] PR Wallace. The band theory of graphite. *Physical Review*, **71**(9):622–634, 1947.
- [5] DP DiVincenzo and EJ Mele. Self-consistent effective-mass theory for intralayer screening in graphite intercalation compounds. *Physical Review B*, **29**(4):1685–1694, 1984.
- [6] E McCann, DSL Abergel, and VI Fal’ko. Electrons in bilayer graphene. *Solid State Communications*, **143**(1–2):110–115, 2007.
- [7] E McCann and VI Fal’ko. Landau-level degeneracy and quantum Hall effect in a graphite bilayer. *Physical Review Letters*, **96**(8):86805, 2006.
- [8] KS Novoselov, E McCann, SV Morozov, VI Fal’ko, MI Katsnelson, U Zeitler, D Jiang, F Schedin, and AK Geim. Unconventional quantum Hall effect and Berry’s phase of 2π in bilayer graphene. *Nature Physics*, **2**(3):177–180, 2006.

- [9] MI Katsnelson, KS Novoselov, and AK Geim. Chiral tunnelling and the Klein paradox in graphene. *Nature Physics*, **2**(9):620–625, 2006.
- [10] AH Castro Neto, F Guinea, NMR Peres, KS Novoselov, and AK Geim. The electronic properties of graphene. *Reviews of Modern Physics*, **81**(1):109–162, 2009.
- [11] J Nilsson, AH Castro Neto, F Guinea, and NMR Peres. Electronic properties of bilayer and multilayer graphene. *Physical Review B*, **78**(4):045405, 2008.
- [12] MS Dresselhaus and G Dresselhaus. Intercalation compounds of graphite. *Advances in Physics*, **51**(1):1–186, 2002.
- [13] R Saito, G Dresselhaus, and MS Dresselhaus. Physical properties of carbon nanotubes. *Imperial College Press, London*, 1998.
- [14] AK Geim. Graphene: status and prospects. *Science*, **324**:1530–1534, 2009.
- [15] S Das Sarma, S Adam, EH Hwang, and E Rossi. Electronic transport in two-dimensional graphene. *Reviews of Modern Physics*, **83**(2):407, 2011.
- [16] CWJ Beenakker. Andreev reflection and Klein tunneling in graphene. *Reviews of Modern Physics*, **80**(4):1337–1354, 2008.
- [17] LB Drissi, EH Saidi, and M Bousmina. Graphene and cousin systems. *arXiv:1108.1748v1*, 2011.
- [18] M Barbier, P Vasilopoulos, and FM Peeters. Single-layer and bilayer graphene superlattices: collimation, additional Dirac points and Dirac lines. *Philosophical Transactions of the Royal Society A — Mathematical Physical and Engineering Sciences*, **368**(1932):5499–5524, 2010.
- [19] M Barbier, P Vasilopoulos, and FM Peeters. Extra Dirac points in the energy spectrum for superlattices on single-layer graphene. *Physical Review B*, **81**(7):075438, 2010.

- [20] M Barbier, P Vasilopoulos, FM Peeters, and JM Pereira. Bilayer graphene with single and multiple electrostatic barriers: Band structure and transmission. *Physical Review B*, **79**(15):155402, 2009.
- [21] M Barbier, FM Peeters, and P Vasilopoulos. Dirac and Klein-Gordon particles in one-dimensional periodic potentials. *Physical Review B*, **77**(11):115446, 2008.
- [22] JC Slonczewski and PR Weiss. Band structure of graphite. *Physical Review*, **109**(2):272–279, 1958.
- [23] JW McClure. Diamagnetism of graphite. *Physical Review*, **104**(3):666–671, 1956.
- [24] M Inoue. Landau levels and cyclotron resonance in graphite. *Journal of the Physical Society of Japan*, **17**(5):808–819, 1962.
- [25] JC Charlier, JP Michenaud, X Gonze, and JP Vigneron. Tight-binding model for the electronic properties of simple hexagonal graphite. *Physical Review B*, **44**(24):237–249, 1991.
- [26] JC Slater and GF Koster. Simplified LCAO method for the periodic potential problem. *Physical Review*, **94**(6):1498–1524, 1954.
- [27] GS Painter and DE Ellis. Electronic band structure and optical properties of graphite from a variational approach. *Physical Review B*, **1**(12):4747–4752, 1970.
- [28] H Suzuura and T Ando. Crossover from symplectic to orthogonal class in a two-dimensional honeycomb lattice. *Physical Review Letters*, **89**(26):266603, 2002.
- [29] JW McClure. Band structure of graphite and de Haas-van Alphen effect. *Physical Review*, **108**(3):612–618, 1957.

- [30] GL Bir and GE Pikus. Symmetry and strain-induced effects in semiconductors. *John Wiley & Sons*, 1974.
- [31] T Ando. Theory of electronic states and transport in carbon nanotubes. *Journal of the Physical Society of Japan*, **74**(3):777–817, 2005.
- [32] VP Gusynin, SG Sharapov, and JP Carbotte. AC conductivity of graphene: From tight-binding model to 2+1-dimensional quantum electrodynamics. *International Journal of Modern Physics B*, **21**(27):4611–4658, 2007.
- [33] GW Semenoff. Condensed-matter simulation of a three-dimensional anomaly. *Physical Review Letters*, **53**(26):2449–2452, 1984.
- [34] K Riley, M Hobson, and S Bence. Mathematical methods for physics and engineering (second edition). *Cambridge University Press*, 2002.
- [35] M Mucha-Kruczyński, E McCann, and VI Fal’ko. Electron–hole asymmetry and energy gaps in bilayer graphene. *Semiconductor Science and Technology*, **25**:033001, 2010.
- [36] JD Bernal. The structure of graphite. *Proceedings of the Royal Society of London, Series A*, **106**(740):749–773, 1924.
- [37] T Ohta, A Bostwick, T Seyller, K Horn, and E Rotenberg. Controlling the electronic structure of bilayer graphene. *Science*, **313**(5789):951–954, 2006.
- [38] JC Charlier, X Gonze, and JP Michenaud. First-principles study of the electronic properties of graphite. *Physical Review B*, **43**(6):4579–4589, 1991.
- [39] E Mendez, A Misu, and MS Dresselhaus. Magnetoreflexion study of graphite under pressure. *Physical Review B*, **21**(2):827–836, 1980.
- [40] R Tatar and S Rabi. Electronic properties of graphite: A unified theoretical study. *Physical Review B*, **25**(6):4126–4141, 1982.

- [41] OP Gupta and PR Wallace. Effect of trigonal warping on Landau levels of graphite. *Physica Status Solidi B*, **54**(1):53–60, 1972.
- [42] G Dresselhaus. Graphite Landau-levels in the presence of trigonal warping. *Physical Review B*, **10**(8):3602–3609, 1974.
- [43] K Nakao. Landau level structure and magnetic breakthrough in graphite. *Journal of the Physical Society of Japan*, **40**(3):761–768, 1976.
- [44] E McCann. Asymmetry gap in the electronic band structure of bilayer graphene. *Physical Review B*, **74**(16):161403, 2006.
- [45] E McCann, DSL Abergel, and VI Fal’ko. The low energy electronic band structure of bilayer graphene. *European Physical Journal — Special Topics*, **148**(1):91–103, 2007.
- [46] CL Lu, CP Chang, YC Huang, RB Chen, and ML Lin. Influence of an electric field on the optical properties of few-layer graphene with AB stacking. *Physical Review B*, **73**(7):144427, 2006.
- [47] F Guinea, AH Castro Neto, and NMR Peres. Electronic states and Landau levels in graphene stacks. *Physical Review B*, **73**(24):245426, 2006.
- [48] H Min, B Sahu, SK Banerjee, and AH MacDonald. Ab initio theory of gate induced gaps in graphene bilayers. *Physical Review B*, **75**(15):155115, 2007.
- [49] JB Oostinga, HB Heersche, X Liu, AF Morpurgo, and LMK Vandersypen. Gate-induced insulating state in bilayer graphene devices. *Nature Materials*, **7**(2):151–157, 2008.
- [50] EV Castro, KS Novoselov, SV Morozov, NMR Peres, JMB Lopes dos Santos, J Nilsson, F Guinea, AK Geim, and AH Castro Neto. Biased bilayer graphene: semiconductor with a gap tunable by the electric field effect. *Physical Review Letters*, **99**(21):216802, 2007.

- [51] Y Zheng and T Ando. Hall conductivity of a two-dimensional graphite system. *Physical Review B*, **65**(24):245420, 2002.
- [52] T Ando, T Nakanishi, and R Saito. Berry's phase and absence of back scattering in carbon nanotubes. *Journal of the Physical Society of Japan*, **67**(8):2857–2862, 1998.
- [53] T Tudorovskiy, KJA Reijnders, and MI Katsnelson. Chiral tunneling in single and bilayer graphene. *Physica Scripta*, **2012**(T146):014010, 2012.
- [54] MV Berry. Quantal phase factors accompanying adiabatic changes. *Proceedings of the Royal Society of London, Series A*, **392**(1802):45–57, 1984.
- [55] MV Berry. Anticipations of the geometric phase. *Physics Today*, **43**:34–40, 1990.
- [56] Y Zhang, YW Tan, HL Stormer, and P Kim. Experimental observation of quantum Hall effect and Berry's phase in graphene. *Nature*, **438**:201–204, 2005.
- [57] N Stander, B Huard, and D Goldhaber-Gordon. Evidence for Klein tunneling in graphene p-n junctions. *Physical Review Letters*, **102**(2):026807, 2009.
- [58] O Klein. Die reflexion von elektronen an einem potentialsprung nach der relativistischen dynamik von Dirac. *Zeitschrift für Physik*, **53**:157–165, 1929.
- [59] CWJ Beenakker, AR Akhmerov, P Recher, and J Tworzydło. Correspondence between Andreev reflection and Klein tunneling in bipolar graphene. *Physical Review B*, **77**(7):075409, 2008.
- [60] AV Shytov, MS Rudner, and LS Levitov. Klein backscattering and Fabry-Perot interference in graphene heterojunctions. *Physical Review Letters*, **101**(15):156804, 2008.

- [61] T Ando and T Nakanishi. Impurity scattering in carbon nanotubes — absence of back scattering. *Journal of the Physical Society of Japan*, **67**(5): 1704–1713, 1998.
- [62] VV Cheianov and VI Fal’ko. Selective transmission of Dirac electrons and ballistic magnetoresistance of np junctions in graphene. *Physical Review B*, **74**(4):41403, 2006.
- [63] VV Cheianov, VI Fal’ko, and BL Altshuler. The focusing of electron flow and a Veselago lens in graphene pn junctions. *Science*, **315**:1252, 2007.
- [64] I Snyman and CWJ Beenakker. Ballistic transmission through a graphene bilayer. *Physical Review B*, **75**(4):045322, 2007.
- [65] J Cayssol, B Huard, and D Goldhaber-Gordon. Contact resistance and shot noise in graphene transistors. *Physical Review B*, **79**(7):075428, 2009.
- [66] B Huard, JA Sulpizio, N Stander, K Todd, B Yang, and D Goldhaber-Gordon. Transport measurements across a tunable potential barrier in graphene. *Physical Review Letters*, **98**(23):236803, 2007.
- [67] JR Williams, L DiCarlo, and CM Marcus. Quantum Hall effect in a gate-controlled p-n junction of graphene. *Science*, **317**(5838):638–641, 2007.
- [68] RV Gorbachev, AS Mayorov, AK Savchenko, DW Horsell, and F Guinea. Conductance of p-n-p structures with “air-bridge” top gates. *Nano Letters*, **8**(7):1995–1999, 2008.
- [69] J Cserti, A Palyi, and C Peterfalvi. Caustics due to a negative refractive index in circular graphene p-n junctions. *Physical Review Letters*, **99**(24): 246801, 2007.
- [70] C Peterfalvi, A Palyi, and J Cserti. Electron flow in circular n-p junctions of bilayer graphene. *Physical Review B*, **80**(7):075416, 2009.

- [71] MM Fogler, DS Novikov, LI Glazman, and BI Shklovskii. Effect of disorder on a graphene p-n junction. *Physical Review B*, **77**(7):075420, 2008.
- [72] LM Zhang and MM Fogler. Nonlinear screening and ballistic transport in a graphene p-n junction. *Physical Review Letters*, **100**(11):116804, 2008.
- [73] AF Young and P Kim. Quantum interference and Klein tunnelling in graphene heterojunctions. *Nature Physics*, **5**:222–226, 2009.
- [74] JR Schrieffer and PA Wolff. Relation between the Anderson and Kondo hamiltonians. *Physical Review*, **149**(2):491–492, 1966.
- [75] CL Roy. Boundary conditions across a δ -function potential in the one-dimensional Dirac equation. *Physical Review A*, **47**(4):3417–3419, 1993.
- [76] M Büttiker. 4-terminal phase-coherent conductance. *Physical Review Letters*, **57**(14):1761–1764, 1986.
- [77] U Fano. Ionization yield of radiations. II. The fluctuations of the number of ions. *Physical Review*, **72**(1):26–29, 1947.
- [78] YM Blanter and M Büttiker. Shot noise in mesoscopic conductors. *Physics Reports*, **336**(1–2):1–166, 2000.
- [79] J Tworzydło, B Trauzettel, M Titov, A Rycerz, and CWJ Beenakker. Sub-Poissonian shot noise in graphene. *Physical Review Letters*, **96**(24):246802, 2006.
- [80] CWJ Beenakker and C Schonenberger. Quantum shot noise. *Physics Today*, **56**(5):37–42, 2003.
- [81] M Büttiker. Scattering theory of thermal and excess noise in open conductors. *Physical Review Letters*, **65**(23):2901–2904, 1990.
- [82] R de L Kronig and WG Penney. Quantum mechanics of electrons in crystal lattices. *Proceedings of the Royal Society of London, Series A*, **130**:499–513, 1931.

- [83] C Kittel. Introduction to solid state physics (seventh edition). *John Wiley & Sons*, 1996.
- [84] R Thom. Structural stability and morphogenesis. *Westview Press*, 1993.
- [85] MV Berry. Waves and Thom's theorem. *Advances in Physics*, **25**(1):1–26, 1976.
- [86] T Poston and I Stewart. Catastrophe theory and its applications. *Pitman, London*, 1978.
- [87] VG Veselago. Superlens as matching device. *arXiv:cond-mat/0501438v1*, 2005.
- [88] VG Veselago. The electrodynamics of substances with simultaneously negative values of ϵ and μ . *Soviet Physics Uspekhi*, **10**(4):509, 1968.
- [89] MV Berry. Singularities in waves and rays. *Les Houches Lecture Series Session*, 1981.
- [90] VG Veselago. About the wording of Fermat's principle for light propagation in media with negative refraction index. *arXiv:cond-mat/0203451v1*, 2002.
- [91] JB Pendry and DR Smith. Comment on "wave refraction in negative-index media: always positive and very inhomogeneous". *Physical Review Letters*, **90**(2):29703, 2003.
- [92] M Kuwabara, DR Clarke, and DA Smith. Anomalous superperiodicity in scanning tunneling microscope images of graphite. *Applied Physics Letters*, **56**(24):2396–2398, 1990.
- [93] WT Pong and C Durkan. A review and outlook for an anomaly of scanning tunnelling microscopy (STM): superlattices on graphite. *Journal of Physics D: Applied Physics*, **38**:R329–R355, 2005.

- [94] PN First, WA de Heer, T Seyller, C Berger, JA Stroschio, and JS Moon. Epitaxial graphenes on silicon carbide. *MRS Bulletin*, **35**:296–305, 2010.
- [95] ZY Rong and P Kuiper. Electronic effects in scanning tunneling microscopy: Moiré pattern on a graphite surface. *Physical Review B*, **48**(23):427–431, 1993.
- [96] JM Campanera, G Savini, I Suarez-Martinez, and MI Heggie. Density functional calculations on the intricacies of Moiré patterns on graphite. *Physical Review B*, **75**(23):235449, 2007.
- [97] R Bistritzer and AH MacDonald. Moiré bands in twisted double-layer graphene. *Proceedings of the National Academy of Sciences*, **108**(30):12233, 2011.
- [98] M Kindermann and EJ Mele. Landau quantization in twisted bilayer graphene: the Dirac comb. *Physical Review B*, **84**(16):161406, 2011.
- [99] S Shallcross, S Sharma, and OA Pankratov. Quantum interference at the twist boundary in graphene. *Physical Review Letters*, **101**(5):056803, 2008.
- [100] M Kindermann and PN First. Local sublattice-symmetry breaking in rotationally faulted multilayer graphene. *Physical Review B*, **83**(4):045425, 2011.
- [101] I Amidror. The theory of the Moiré phenomenon. *Kluwer Academic Publishers*, 2000.
- [102] I Amidror. Moiré patterns between aperiodic layers: quantitative analysis and synthesis. *Journal of the Optical Society of America A — Optics Image Science and Vision*, **20**(10):1900–1919, 2003.
- [103] GL Rogers. A geometrical approach to Moiré pattern calculations. *Optica Acta*, **24**(1):1–13, 1977.

- [104] JAC Yule. Principles of color reproduction applied to photomechanical reproduction, color photography, and the ink, paper, and other related industries. *Wiley*, 1967.
- [105] Y Nishijima and G Oster. Moiré patterns: their application to refractive index and refractive index gradient measurements. *Journal of the Optical Society of America*, **54**(1):1–5, 1964.
- [106] E Cisternas, M Flores, and P Vargas. Superstructures in arrays of rotated graphene layers: Electronic structure calculations. *Physical Review B*, **78**(12):125406, 2008.
- [107] J Martin, N Akerman, G Ulbricht, T Lohmann, JH Smet, K von Klitzing, and A Yacoby. Observation of electron-hole puddles in graphene using a scanning single-electron transistor. *Nature Physics*, **4**:144–148, 2007.
- [108] K Watanabe, T Taniguchi, and H Kanda. Direct-bandgap properties and evidence for ultraviolet lasing of hexagonal boron nitride single crystal. *Nature Materials*, **3**:404–409, 2004.
- [109] J Robertson. Electronic structure and core exciton of hexagonal boron nitride. *Physical Review B*, **29**(4):2131–2137, 1984.
- [110] G Giovannetti, PA Khomyakov, G Brocks, PJ Kelly, and J van den Brink. Substrate-induced band gap in graphene on hexagonal boron nitride: ab initio density functional calculations. *Physical Review B*, **76**(7):073103, 2007.
- [111] J Tersoff and DR Hamann. Theory of the scanning tunneling microscope. *Physical Review B*, **31**(2):805–813, 1985.
- [112] VJ Cee, DL Patrick, and TP Beebe. Unusual aspects of superperiodic features on highly oriented pyrolytic graphite. *Surface Science*, **329**(1–2):141–148, 1995.

- [113] J Xhie, K Sattler, M Ge, and N Venkateswaran. Giant and supergiant lattices on graphite. *Physical Review B*, **47**(23):835–841, 1993.
- [114] R Decker, Y Wang, VW Brar, W Regan, HZ Tsai, Q Wu, W Gannett, A Zettl, and MF Crommie. Local electronic properties of graphene on a BN substrate via scanning tunneling microscopy. *Nano Letters*, **11**:2291–2295, 2011.
- [115] J Xue, J Sanchez-Yamagishi, D Bulmash, P Jacquod, A Deshpande, K Watanabe, T Taniguchi, P Jarillo-Herrero, and BJ LeRoy. Scanning tunnelling microscopy and spectroscopy of ultra-flat graphene on hexagonal boron nitride. *Nature Materials*, **10**(4):282–285, 2011.
- [116] P San-Jose, E Prada, E McCann, and H Schomerus. Pseudospin valve in bilayer graphene: towards graphene-based pseudospintronics. *Physical Review Letters*, **102**(24):247204, 2009.

Colophon

This thesis was typeset using \LaTeX . Computer Modern was used as the type for all text. GNU Emacs was used to edit the \TeX , together with AU \TeX . Papers.app was used on Mac OS X Snow Leopard to collate articles for use in the bibliography, outputting to Bib \TeX format. This was passed through a script of the author's own design, primarily using sed, to clean it up before being passed to Bib \TeX to generate the bibliography. Ref \TeX was used to easily manage this Bib \TeX file, generating references and citation indexes.

MIT License

All code within this thesis is placed under the MIT License:

Copyright (c) 2012 Chris Poole <chris@chrispoole.com>

Permission is hereby granted, free of charge, to any person obtaining a copy of this software and associated documentation files (the "Software"), to deal in the Software without restriction, including without limitation the rights to use, copy, modify, merge, publish, distribute, sublicense, and/or sell copies of the Software, and to permit persons to whom the Software is furnished to do so, subject to the following conditions:

The above copyright notice and this permission notice shall be included in all copies or substantial portions of the Software.

THE SOFTWARE IS PROVIDED "AS IS", WITHOUT WARRANTY OF ANY KIND, EXPRESS OR IMPLIED, INCLUDING BUT NOT LIMITED TO THE WARRANTIES OF MERCHANTABILITY, FITNESS FOR A PARTICULAR PURPOSE AND NONINFRINGEMENT. IN NO EVENT SHALL THE AUTHORS OR COPYRIGHT HOLDERS BE LIABLE FOR ANY CLAIM, DAMAGES OR OTHER LIABILITY, WHETHER IN AN ACTION OF CONTRACT, TORT OR OTHERWISE, ARISING FROM, OUT OF OR IN CONNECTION WITH THE SOFTWARE OR THE USE OR OTHER DEALINGS IN THE SOFTWARE.